ELECTROCHEMICAL INVESTIGATIONS OF ION TRANSPORT IN UNCONVENTIONAL ENVIRONMENTS

A THESIS SUBMITTED TO
THE GRADUATE SCHOOL OF ENGINEERING AND SCIENCE
OF BILKENT UNIVERSITY
IN PARTIAL FULFILLMENT OF THE REQUIREMENTS FOR
THE DEGREE OF
MASTER OF SCIENCE
IN
CHEMISTRY

By
Can Berk Uzundal
July 2018

ELECTROCHEMICAL INVESTIGATIONS OF ION TRANSPORT IN UNCONVENTIONAL ENVIRONMENTS

By Can Berk Uzundal

July 2018

We certify that we have read this thesis and that in our opinion it is fully adequate, in scope and in quality, as a theiss for the degree of Master of Science.

_____

Burak Ülgüt (Advisor)

_____

Şefik Süzer

_____

Ömer Dağ

_____

Dinçer Gökçen

_____

Ali Çırpan

Approved for the Graduate School of Engineering and Science:

_____

Ezhan Karaşan
Director of the Graduate School of Engineering and Science

ABSTRACT

ELECTROCHEMICAL INVESTIGATIONS OF ION TRANSPORT IN UNCONVENTIONAL ENVIRONMENTS

Can Berk Uzundal

M. Sc. in Chemistry

Advisor: Burak Ülgüt

July 2018

Ion transport is a critical process that occurs routinely in all electrochemical devices. Especially the new generation batteries extensively utilized in portable devices, Li-Ion batteries, operate simply through Li^+ transport. Although, a multitude of similar energy storage and conversion devices are prevalent in both the industry and the electrochemical literature, these devices are not the only technologies that ion transport is critical. Other technologies such as electrochromic devices, organic electronics and next generation display panels also involve electrochemical processes that are inherently dependent on or limited by ion transport. Conventional electrochemical methods enable interrogation of the

various interfaces these devices possess however limited information on the behavior of the concentrated-like media investigated in this thesis compared to the well documented behavior of the dilute media, limits their applicability.

In this thesis we not only offer investigations on possible esoteric materials that have unique ion transport properties that show emergent behavior in the systems they are employed at through fundamental electrochemical studies but also we outline the development of new electroanalytical tools to better interrogate ion transport in variety of electrochemical systems. The attempts at understanding and explaining the ion transport in various media and to leverage its benefits towards better devices is outlined. Electrochemical noise measurements for Li-Ion batteries is shown as a potential tool for ion transport interrogation, while the ion transport behavior of Liquid Crystals and Ionic Liquids are investigated. A new electroanalytical tool to separate counter ion diffusion from electron transfer is also shown. Finally, an electrochemical method to visualize corrosion that utilizes ion transport is outlined in this thesis.

Keywords: Electrochemistry, Electroanalytical tools, Ionic liquids, Liquid Crystals, H_2 permeation, Electrochemical Noise.

ÖZET

GELENEKSEL OLMAYAN ORTAMLARDA ELEKTROKİMYASAL İYON TAŞINMASININ SORGULANMASI

Can Berk Uzundal

Kimya, Yüksek Lisans

Tez Danışmanı: Burak Ülgüt

Temmuz 2018

İyon taşınması bütün elektrokimyasal cihazlarda gerçekleşen kritik bir süreçtir. Özellikle taşınabilir cihazlarda kullanılan yeni nesil piller, Li-Iyon pilleri, Li^+ taşınımı prensibi ile çalışmaktadır. Bir çok benzer enerji depolama ve dönüştürme aygıtı hem literatürde hem de endüstride yaygın olsa da, bu cihazlar iyon taşınımın kritik olduğu tek teknoloji değildir. Elektrokromik cihazlar, organik elektronikler ve görüntü panelleri gibi diğer cihazlar da iyon taşınımını direk olarak kullanan veya iyon taşınımı tarafından limitlenen başka elektrokimyasal süreçler kullanmaktadır. Geleneksel elektrokimyasal methodlar bu cihazların çeşitli arayüzlerinin incelenmesini sağlasa da, bu tezde incelenen yüksek konsantrasyon-

benzeri ortamlarda, iyi incelenmiş seyreltik çözeltiler ile kıyaslandığında, sınırlı miktarda bilgi sağlamaktadır ve bu onların uygulanabilirliğini sınırlamaktadır.

Bu tezde hem iyon taşınımı açısından özgün özelliklere sahip materyallerin elektrokimyasal olarak incelenmesinin yanı sıra iyon taşınımının daha iyi incelenmesini sağlayabilecek elektroanalitik araçların geliştirilmesini de özetliyoruz. Bu tez, elektrokimyasal gürültü ölçümlerini Li-Iyon pilleri için iyon hareketini ölçebilecek potansiyel bir araç olarak gösterirken, sıvı kristaller ve iyonik sıvılarda iyon hareketi incelenmiştir. Aynı zamanda, karşıt iyon difüzyonunu elektron transferinden ayırabilecek yeni bir elektroanalitik yöntem geliştirilmiştir.

Anahtar Sözcükler: Elektrokimya, Elektroanalitik Araçlar, Iyonik Sıvılar, Sıvı Kristaller, H_2 nüfuzu, Elektrokimyasal Gürültü

Acknowledgements

On paper this degree is the result of a two-year study. In reality the process started when I set foot on the campus 6 years ago. As such I have a lot of people to acknowledge for help, support and awesomeness.

I sincerely thank all of my Prof's at the chemistry department, they have been extremely patient with me and shown great interest in not only my development as a scientist but also as a person. I am glad that I had the opportunity to be part of this awesome department.

Unknowingly, the day I met and decided on working with my advisor, Prof. Burak Ülgüt, with extensive guidance from Prof. Ömer Dağ, shaped me in so many ways that I cannot begin to list. I got to learn an awesome field, electrochemistry, from the best. Hocam, not only I learned electrochemistry but also how to be a scientist. I cannot thank you enough. You have given me a solid start for a career. Thank you for your time, thank you for your patience, thank you for your understanding and overall just thank you for everything.

During my time here, I had the chance to pick the brains of almost all of my Profs (aside from my advisor), some more than others. Prof. Şefik Süzer and Prof. Ömer Dağ, you have given me perspectives that I did not even know I could wrap my head around. I truly appreciate your guidance, encouragements and inspirations.

I also need to acknowledge my informal co-advisor Ethem Anber. I have probably spent more time in your office in my first year than in the lab. You have been a

wonderful teacher of all things electronic. Not only that but you have given me someone that I can trust whenever something goes wrong. I truly admire your resolve to learn more and be productive and strive to be more like you every day. Thank you.

As important as my firstly academic acknowledgements, I really have to acknowledge the mixed support from my partner in crime (as cliché as that might be). Her support has been mixed because not only did she provide me with emotional support during the many lows that I've been through but also she has been in the lab with me throughout all of it. I am looking forward to what is next for us. I hope to write an even better acknowledgement for the next thesis that I will be writing. Thank you Gozde Karaoglu, you have been my only hope.

The obligatory acknowledgement to the family goes as the following;

Annemlerim, thank you for your unquestioning support, without you I would have been strayed away from this path long ago. Annem, whenever I may have needed assistance I knew I could count on you. Beste, you have been there for anything I have asked for, you have been extremely understanding with me being busy all the time, Ece, you know I got the smarts from you. Thank you all.

Table of Contents

List of Figures

List of Tables

List of Abbreviations

OFET: Organic Field Effect Transistor

SEI: Solid Electrolyte Interface

LCD: Liquid Crystal Display

SHE: Standard Hydrogen Electrode

EIS: Electrochemical Impedance Spectroscopy

OpAmp: Operational Amplifier

WE, RE, CE: Working Electrode, Reference Electrode, Counter Electrode

UME: UltraMicro Electrode

CV: Cyclic Voltammetry

A/D: Analog to Digital

SECM: Scanning Electron Microscopy

RGB: Red Green Blue

LLC: Lyotropic Liquid Crystal

SA: Sulfuric Acid

$C_{12}E_{10}$: 10-lauryl ether

LAB: Lead Acid Baterry

I/E: Current to Voltage

FTO: Fluorine doped Tin Oxide glass

XPS: X-ray Photoelectron Spectroscopy

Chapter 1

1. Introduction

1.1 General Scope and Overview

Ion transport manifests itself as an essential component of various electrochemical technologies and their problems encountered on a daily basis. State-of-the-art technologies such as Li-ion based batteries, third generation solar cells, capacitive deionization and smart windows involve processes that are directly limited and controlled by ion transport [1]. For performances beyond the current norm in these technologies/to achieve the theoretical limits in the current device architectures and to guide the development of next generation devices, a fundamental grasp at the molecular scale is required [2,3]. In all electrochemically relevant devices, a change in state (either loss of charge stored, a color change or even change in i-V

characteristics for an OFET transistor) is introduced by an applied external bias. Although a fundamental grasp on the electrified interfaces of these devices is in most cases possible and is probed by conventional electrochemical methods as introduced in the Basics of Electrochemistry section of this thesis, certain details of these systems under operation are not predictable with conventional electrochemical methods as will be discussed. For instance, the main charge storage mechanism in rechargeable Li-ion batteries, i.e. Li^+ shuttling through an intercalation material, is well understood and can even be modeled to achieve the expected response for a given material [4]. Yet, since its discovery, significant research efforts are directed towards understanding the so-called Solid-Electrolyte-Interface (SEI) that forms during cycling which significantly influence battery performance[5,6]. Contrary to all the efforts, the transport properties of the SEI, is not well known although probable species involved in the formation of the interface have been outlined[7]. Due to the reactive medium complicating experimental approaches, theoretical approaches attract interest and these methods have been recently reviewed elsewhere[8]. The effects of the SEI on the battery operation is not well understood and can be at times contradictory to the common expectations. In principle, SEI needs to rapidly shuttle Li^+ while not allowing the permeation of the electrolyte thus passivating the otherwise reactive electrodes towards parasitic side reactions [6]. Recently, transport of various other cations aside from Li^+ has been experimentally observed which through disruption of SEI lowers the cycling capabilities of the batteries [9,10]. The unexpected and unaccounted transport of these ions even in the extensively studied Li-Ion systems shows that our

understanding on the ion transport processes is lacking compared to our understanding of the initial electron transfer initiated behavior which is well characterized and captured by the conventional electrochemical systems. A theme in this thesis will be introducing novel electrochemical methods to bridge this gap in understanding as will be discussed Chapter 2 and 5 of this thesis.

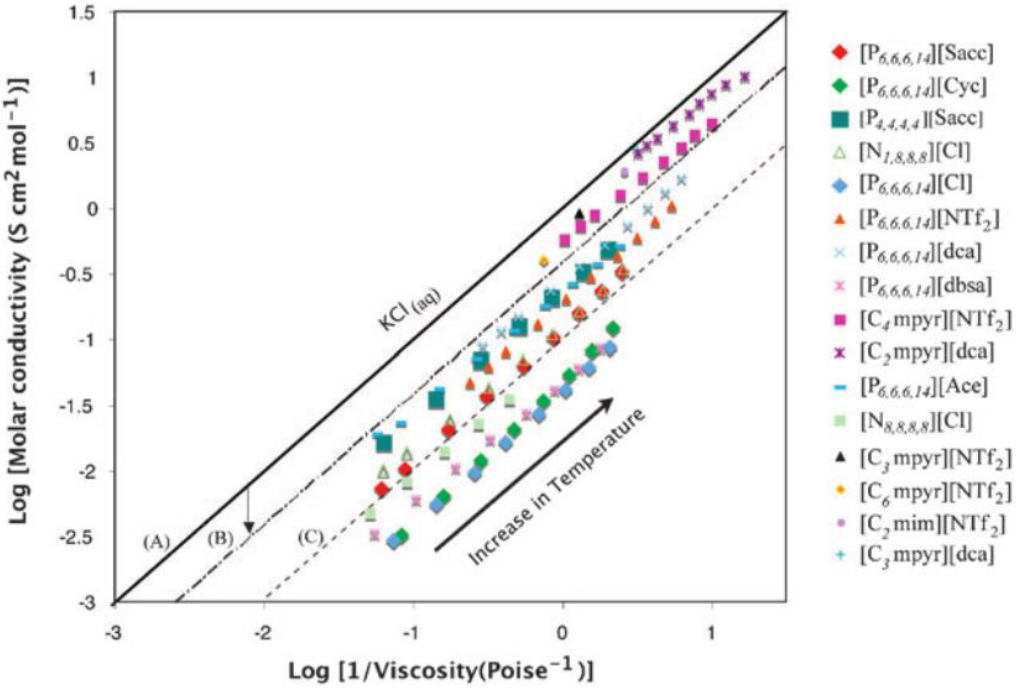

Figure 1. 1 The Walden plot of various ionic liquids at different temperatures. "Reproduced with permission from [11]*."*

Electroneutrality principle states that due to coulombic forces, transport of an ion needs to be accompanied shortly after by the transport of another ion of the opposite charge such that the overall charge in the medium is constant and zero[12] This principle, although holds strongly for well supported media, has been shown to fail at short timescales and at relatively close distances (compared to the Debye time

and length[1] respectively) in weakly supported electrolytes and the relatively simple theory behind accounting for this short scale breakdown has been reviewed elsewhere[12]. A breakdown of electroneutrality, however at much longer length and timescales (compared to the Debye lengths and times relevant to electrolytic solutions) were experimentally observed for the intercalation of ionic liquids into a multi-layered graphene under external bias[13]. These studies in conjunction with other studies that will be introduced in the basics of Electrochemistry section, again demonstrate that the current comprehension on ion transport is lacking or needs overhauls to be able to capture the behavior under applied bias for other materials. Ionic liquids, in particular, seem to generate a lot of interest in the field owing to their low vapor pressure, wide electrochemical window and their high conductivity, yet the rather low number of available charged species[11] allows the investigations of the ion migration effects without the interferences from the ohmic losses that is observed for weakly supported electrolytes. The effect of the lower number of available charged species is clear when compared to an aqueous solution of similar viscosity as shown in Figure 1.1. At the same viscosity the conductivity of the ionic liquid is much smaller, showing that ions do not freely move in the solution but rather participate in a pairing equilibrium [11].As a result, the structure of the electrochemical double layer and its kinetics are still under study and requires multi-dimensional theoretical and experimental investigations to properly address both the microscale ordering[14,15] and the macroscale voltage screening

[1] Debye time is defined as the amount of time an ion can spend without being explicitly paired

effects[16]. A coarse grained electrostatic model to account for this extended voltage screening effect will be introduced in Chapter 6 of this thesis.

Another open question regarding the ions in various media outlined in this thesis is their activity coefficients, where the activity coefficient itself has inherent information regarding the ion transport events happening inside a medium for the particular ion[17]. Even Nernst equation (as mentioned in the following "Basics" section) can at times be shown to be counterintuitive or not applicable in the same way it is used in conventional systems (as will be shown in Chapter 4 of this thesis). An area of research that has been recently revitalized and that suffers from the lack of understanding caused by the failure of the theories applicable to dilute electrolyte solutions is the so-called solvent-in-salt-electrolytes or soggy-sand electrolytes. Their applications in various fields have recently been reviewed elsewhere[18]. The recent surge in interest towards water-in-salt electrolytes for energy storage applications is owing to the ability of these electrolytes to address safety concerns of the conventional Li-Ion batteries stemming from the organic solvents used. Water-in-salt electrolytes compared to their conventional aqueous counterparts have significantly wider electrochemical windows and thus enhanced energy densities[19]. It is believed that the water in these systems form small channels where these channels act as small reaction chambers. The activity of water in these small channels, however, is not well understood and the current studies mostly focus on predicting the channel structure formed at various water loadings[18]. Further studies are needed to fully understand the activity of water in these concentrated solutions where dilute solution theories, as expected fail. Similar

arguments can be extended to Liquid Crystal systems where the water in the system is stuck inside a matrix of surfactant and electroactive species[20] These liquid crystals show excellent conductivities, yet their electrochemical behavior is shown to be completely distinct compared to their aqueous counterparts as will be discussed in Chapter 4.

Although ion transport at various semi-condensed phases described above are not well understood or have aspects that need clarifications both through theory and experimentation, manipulating ion transport for emergent properties have been a common theme in science for well over a decade[21]. Conducting polymers have been extensively utilized in variety of application following their almost metallic conductivities. Especially for light emitting applications and in organic electronics, this class of polymers attract attention. A prime example of leveraging ion transport for emergent behavior is again Li-Ion batteries. Manipulating and achieving control over ion transport can help solve contemporary problems and this is the main theme of this thesis. Utilizing the facile hydrogen transport through a metal, a method that can guide research towards the solution of another contemporary problem, corrosion, will be introduced in Chapter 3 of this thesis.

These examples show that control over ion transport in conjunction with heterogeneous electron transfer can generate emergent behavior in systems under investigation that is not necessarily solely results of either the ion transport or the electron transfer but rather a combination. This thesis outlines attempts at both understanding and controlling ion transport across various media to achieve new behavior in various condensed/semi-condensed phases such as metals, ionic liquids,

liquid crystals and conjugated polymers. These classes of materials have upcoming promising applications in numerous applications including energy storage and conversion. Ionic liquids attract attention as a substitute for the conventional solvent based electrolytes used in many industrial applications ranging from simple material synthesis to battery electrolytes owing to their low vapor pressures and high conductivities. Similarly, aside from applications in LCD displays, liquid crystals attract attention as electrocatalysts and even proposed electrolyte substitutes for various batteries alleviating multitude of problems in battery chemistries they are applied at. Conjugated polymers, aside from their excellent electron conductivities for solution processable materials, have applications as electrochromic materials. The reader is encouraged to peruse the specific chapter of interest for a more detailed introduction to the topics summarized briefly here.

1.2 Basics of Electrochemistry

Electrochemistry can be summarized as the study of materials under various applied electrical potentials and currents [22]. Chemical changes as a result of the passing current, be it under controlled potential or current, provides tools that are not readily available within the toolbox of the rest of chemistry. At the very fundamental, chemical changes can be directly quantified by counting the number of electrons consumed for a given process through Faraday's Law. Although this macroscopic view of counting electrons do give quantitative information regarding electrochemical processes, details of such events are of utmost interest where control over these processes directly control the emergent properties.

In a typical electrochemical setup, a metal electrode (called the working electrode) is at the center of the measurement. The perturbation (either a controlled voltage or current) of choice is referred to the working electrode/electrolyte interface. The potential is controlled with respect to a reference electrode whose electrochemical potential is exactly known, such as a Ag/AgCl reference electrode or a Standard Hydrogen Electrode (SHE). The current that needs to pass through the system for a given perturbation does not flow over the reference electrode since that would cause the potential of the reference to eventually shift and introduce artifacts. Instead another metallic electrode is used as current path such that the counter reaction of the reaction occurring in the working electrode occurs at any given time without interfering with the voltage measurement. This is called the counter electrode. The solution in the electrochemical cell contains the analyte of interest (can practically be anything, salts, biomolecules, organic molecules...) while a solvent containing an ionic salt constitutes the electrolyte. The summarized electrochemical setup consists of three electrodes, the working, reference and counter electrodes, where the electrochemical potential of the system is then defined as the potential difference between the working and reference electrodes while the current flows between the working and the counter electrodes. However, an external reference electrode may not always be available for various reasons. For example, batteries only have two terminals (the positive and the negative terminals). Instead, in these cases, a two electrode setup is utilized where the working electrode is attached to one of the terminals while the counter and the reference electrodes are attached to the other. The drawback of this approach is not being able to absolutely measure

the potential drops across the two electrode/electrolyte interfaces. The potential in the two electrode setup is defined with respect to the reaction happening at the counter electrode where this counter reaction is usually not known. Even when the reaction is known, the exact concentrations of the species involved in the reaction is usually not available or they change during the course of an experiment causing issues with potential determination. Instead, either this reaction is assumed steady and constant and the potentials are reported without further calibration or the potentials are calibrated using an external or internal redox couple of known potential. Usually ferrocene/ferrocenium couple is utilized as an internal redox couple where the half-cell potential of the reaction under standard conditions is well known and the fast kinetics of the redox couple allows easy potential determination across most electrochemical experiments. Another internal reference that is typically used is the Li/Li^+ couple readily available in the electrolyte of a Li-ion battery.

The study of electrochemistry by definition involves elucidating various relationships between the current and the potential of the system under question. Since these two (potential and current) are fundamentally linked (e.g. most simply by Ohm's Law), controlling either causes a restraint on the other. Experiments under potential control are called potentiostatic experiments while experiments under current control are called galvanostatic experiments. Though similar potential and current waveforms are applied (i.e. sine waves, ramps, sweeps...) for both galvanostatic and potentiostatic experiments, vastly unique conclusions can be made using either constraint. The difference in these methods stems from the

fundamental difference between the limits imposed on the system by constraining either the current or the voltage. Considering a limited current experiment, the instrument forces the system to push a set amount of current through the electrolyte no matter the electrochemical reactions taking place to sustain that current through the electrochemical cell. In the extreme case, at high currents, the kinetics of an electrochemical reaction of interest may lag behind and cause another reaction, typically solvent electrolysis, take its place and dominate the voltage responses observed. Therefore, galvanostatic experiments can be thought as controlling the kinetics of the system. Similarly, considering a controlled potential experiment, the instrument holds the potential of the electrode at a certain value which causes only the reactants that are thermodynamically favorable to undergo redox reactions at the relevant kinetics to give a current response. The extent of this driving force can be calculated by comparing the potentials obtained from the Nernst equation (Eq. 1.1) for a given system with the applied potential at the electrode. Therefore, potentiostatic experiments can be thought as controlling the thermodynamics of the system. If given an option between potentiostatic and galvanostatic experiments, usually potentiostatic experiments are chosen since controlling thermodynamics is usually much more predictable compared to fine tuning the currents to obtain and probe the kinetics of interest, especially in aqueous electrolytes. For the purposes of this thesis, mostly potentiostatic methods will be summarized, however, extensions to galvanostatic systems are similar and can be found elsewhere [22].

$$E = E^0 + \frac{RT}{nF} ln \frac{a_{ox}}{a_{red}} \quad (1.1)$$

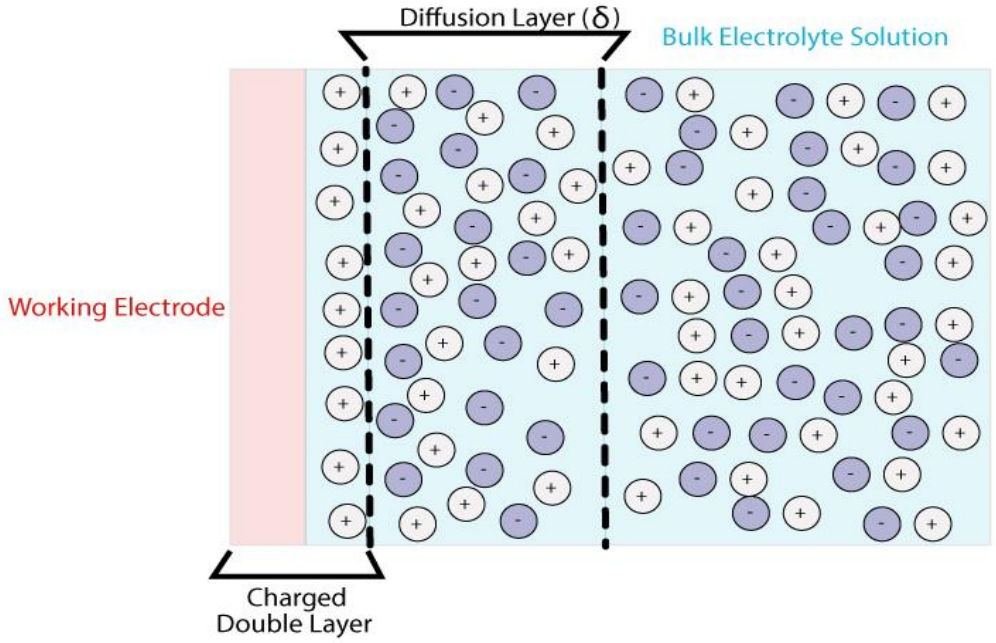

Figure 1. 2 Schematic representation of the charge rearrangements in the electrolyte solution

Consider an electrode with an applied positive bias, to screen the applied bias ions in the electrolyte solution needs to rearrange. For applied bias that is positive of the potential of zero charge, negative ions from the bulk solution needs to come in close to the surface of the electrode, this ion rearrangement is called the compact electrochemical double layer and is usually confined near the electrode surface (~ nm) for typical electrolyte concentrations. The cascading ion rearrangements to properly screen the surface charge of the electrode, however, extends much further than the compact layer and is called the diffuse double layer. These ion rearrangements of the electrolyte (that result in transient currents) are not considered in the Faraday's law since they do not directly involve a redox reaction/chemical change and they are called non-faradaic events. The magnitude

of the non-faradaic current and the energy stored in this mode can range orders of magnitude depending on the surface area of the electrode used and is primarily a result of the charging or discharging of the electrochemical double layer. The electrochemical double layer, as described above, can be visualized, in terms of classical electrical circuit components as a double layer capacitor with a certain capacitance. The capacitance and thus the energy stored in the double layer/in non-faradaic fashion depends primarily on the microscopic surface area of the electrode used as predicted by the simple parallel plate capacitor relations. Supercapacitors utilize this charge stored in the double layer and can achieve extremely high capacitances at limited package sizes owing to the extremely small distances at which the charges are stored. In terms of the electroactive material in the solution, the analyte, the applied potential causes the electroactive material in the vicinity of the electrode to pick up or lose electrons at the electrode. For this heterogeneous electron transfer reaction to occur, the electroactive species need to diffuse to the electrode surface in the timescale of the experiment. The timescale of the experiment can be controlled by the applied perturbation, where if a constant potential (as in choronoamperometry) is applied for long periods of time, then an extended region of analyte have the time to diffuse to the electrode and participate in redox reactions, while if the perturbation constantly changes in amplitude and polarity (as in usual cyclic voltammetry) with time, then only a small region near the vicinity of the electrode (~μm in conventional cyclic voltammetry) can participate in redox reactions. This region of the solution where concentrations of the various electroactive species are different than the bulk concentrations as a

result of the redox reactions taking place at the electrode is called the diffusion layer. The diffusion layer is a construct that enables the visualization of the processes occurring at the electrode-electrolyte interface where in an electrochemical measurement, faradaic current response is only observed for the species that can travel the length of the diffusion layer in the timescale of the experiment.

Similar to the electrochemical double layer, it is possible to depict the major phenomena occurring in the electrochemical cell as circuit elements. This approach of equivalent circuit analysis is usually employed to extract relevant parameters (resistances, capacitances, number of interfaces...) out of Electrochemical Impedance Spectra (EIS). EIS can get incredibly involved in terms of analysis especially when porous materials such as battery electrodes are investigated. For the simple electrochemical cell, however, a relatively simple equivalent circuit can be constructed which aids in understanding processes occurring near the electrode. As explained above, the electrochemical double layer can be modeled as a capacitor. The capacitance of this capacitor depends on the dielectric constant of the electrolyte and the surface area of the electrode in question. While the ions of the supporting electrolyte move in the solution to form the double layer and use some of the current response, redox reactions at the surface of the electrode compete for the same current, therefore the formation of the electrochemical double layer and the redox reactions should be depicted by circuit elements that are in parallel to each other. The redox reactions can be modeled by a resistance associated with the charge transfer as can be derived by the low over-potential limit of the Butler-

Volmer kinetics [22]. The resistance introduced to the electrochemical cell due to the rest of the electrolyte solution/the bulk of the solution, is then modeled as a series resistance. This parasitic resistance causes small ohmic losses in the electrochemical setup which is usually ignored for conventional experiments due to the relatively low value of the resistance (~Ω) and the relatively low currents involved (~μA). The summarized equivalent circuit is called a simplified Randles' Cell. For a more complete picture for processes under mass transport limits a theoretical circuit component (called a Warburg) can be attached in series to the charge transfer resistance.

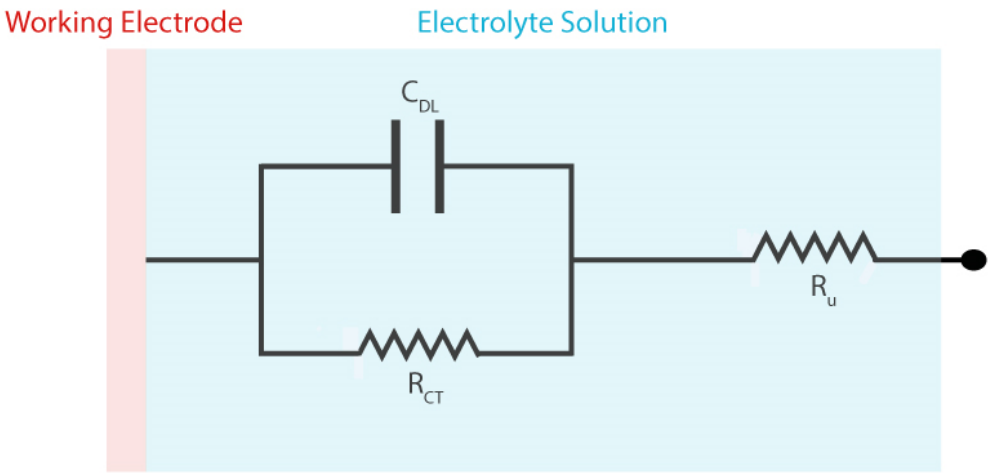

Figure 1. 3 Simplified Randles' equivalent circuit of a common electrochemical cell

The above summarized picture, then, involves multiple physical phenomena occurring simultaneously to yield the currents we investigate in potentiostatic experiments. The flux of redox-active species to the working electrode can be calculated and can be used to predict the current responses to various voltage waveforms. This flux has contributions from diffusion, migration and convection

as explained by the Nernst-Planck equation (Eq. 1.2). In most electrochemical systems the contribution to the flux from migration and convection (second and third terms of Eq. 1.2. respectively) are ignored. The migration of electroactive species is ignored since usually a supporting electrolyte is used to carry the bulk of the current flowing through the electrochemical cell while convection is ignored since no intentional flow is introduced into the system. Electrochemical methods under purposefully introduced convective flows is called hydrodynamic techniques and allows the study of electrochemical reactions without mass transport limits. For the purposes of this thesis, these methods are not directly relevant, a detailed discussion can be found elsewhere[22].

$$J(x) = -D\frac{\partial C}{\partial x} - \frac{zF}{RT}DC\frac{\partial \gamma}{\partial x} + Cv(x) \qquad (1.2)$$

On the following sections, for the most prevalent voltage perturbations, the solution of the appropriate ion flux equations will be discussed, however, instrumentation that can apply these voltage perturbations deserve a mention as well.

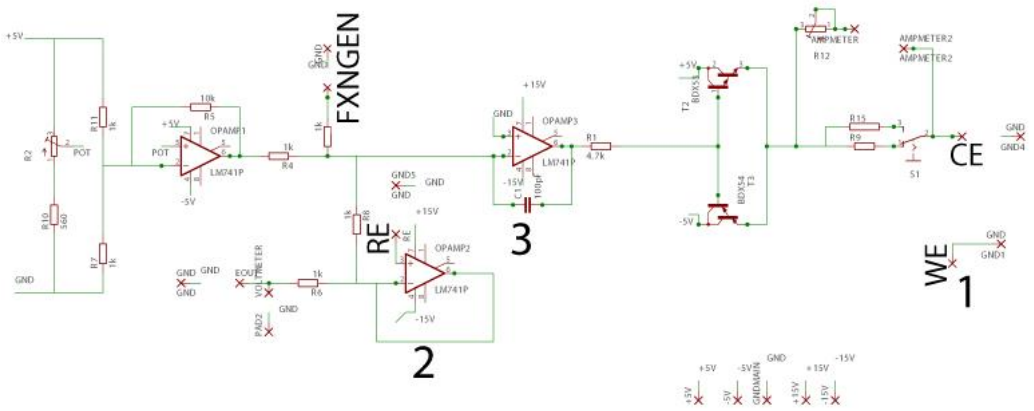

Figure 1. 4 Circuit schematic of a potentiostat.

Commercialization of Operational Amplifiers, OpAmps, in cheap and small packages enabled electrochemistry to evolve from few simple DC experiments at constant currents to the vast field it is today. Especially the high bandwidth, high gain OpAmps that are readily available from multiple manufacturers allows custom instruments to be built for tailored applications. The instrument that controls the potential applied to the electrochemical cell is called a potentiostat. Although the specific potentiostat circuitry relevant in this thesis will be discussed in the Ultrafast Spectroelectrochemistry Chapter, the basic principles are as follows. A signal waveform is generated either using a digital or analog signal generator as denoted by FXNGEN in the schematic. The above schematic uses a grounded working electrode (as denoted by 1 in the Figure) for reasons that will be discussed in the Ultrafast Spectroelectrochemistry Chapter. A feedback loop (denoted as 2) that compares the voltage of the reference electrode (denoted as RE) to the voltages of the working electrode (denoted as 3, keep in mind that the working electrode is grounded) and the function generator input is employed such that the potential measured over the working and the reference leads of the instrument is held at the same potential imposed by the signal generator. This outlined circuit can be expanded to include a signal amplification, current to voltage conversion chain and a solution resistance compensation as will be shown in the Ultrafast Spectroelectrochemistry Chapter.

1.2.1 Chronoamperometry

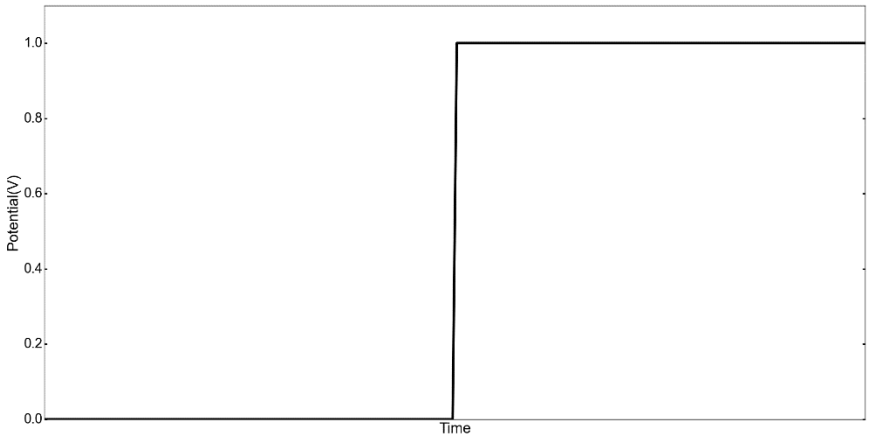

Figure 1. 5 The voltage profile applied in a standard chronoamperometry experiment.

In chronoamperometry, a simple abrupt change in potential is applied to the electrode and the current as a result of the applied voltage step is monitored. Potential steps and its associated methods present one of the most utilized techniques in electrochemistry. Information regarding the diffusion coefficients of the electroactive species and the electrochemical reversibility of the system can be extracted by relatively simple treatments to the chronoamperometry data.

As explained in the previous chapter, an electrochemical cell can be explained using equivalent circuit models. This not only helps in understanding the electrode processes and extracting parameters regarding these processes, but also can help predict the behavior of the electrochemical cell to an external perturbation. Considering a simple first order RC circuit, the current response to a step in potential is simply an exponential decay with a certain time constant as shown in Eq. 1.3.

$$i = -\frac{V_o}{R} e^{-\frac{t}{RC}} \tag{1.3}$$

Eq. 1.3. is derived for a pure RC circuit, which is applicable for a Simplified Randles Cell, however, in most electrochemical cells, reactions occur under mass transport limitations and flux equations such as the Nernst Planck equation shown in Eq. 1.2 needs to be solved with the appropriate boundary conditions. The problem, however, is simplified considering that migration and convection is ignored and only the Fick's Law of diffusion needs to be solved for the given geometry. Still the simple RC analysis guides our expectations from an analytical solution and presents a lower limit on the observed currents. Usually, in electrochemical cells, a small electrode is used such that the applied potential does not change the bulk concentrations of ions appreciably and the timescales are such that the bulk concentration is constant. This simplifies the mathematical treatment substantially. Especially with the utilization of ultramicroelectrodes(UME) (of diameter ~μm), this assumption holds without fail.

Once a step is applied, all of the species in the vicinity of the electrode undergo redox reactions and result in a large current, while at longer times, current slowly decays since more and more electroactive species need to travel longer distances from the electrode to continue the redox reaction at the electrode. Assuming a planar electrode with sufficiently large applied potential to fully oxidize or reduce the species at the electrode surface such that the surface concentration of the electroactive species at the given potential is 0, the diffusion equations can be solved to yield the Cottrell equation as seen in Eq. 1.4.

$$i(t) = \frac{nFAD^{\frac{1}{2}}C}{\pi^{\frac{1}{2}}t^{\frac{1}{2}}} \quad (1.4)$$

As can be seen, Cottrell Equation predicts infinite current once the potential step occurs. In reality this infinite jump is limited by various factors. It is important to understand these limitations which are almost always present in any electrochemical methods/setups. The first limit is imposed by the potentiostat of choice to conduct the experiment where there is an upper limit on the current that can be supplied by the instrument, thus the infinite current predicted can never be supplied by the instrument. Even before a faradaic reaction occurs, non-faradaic effects occur and the double layer charging needs to complete. During the experiment the time constant of the electrochemical cell determined by the double layer capacitance and the uncompensated resistance of the electrolyte presents an upper bound on the smallest time at which a change in potential can be established. Therefore, an infinitely sharp current spike cannot be observed. At the infinite time limit, the inherent vibrations in regular electrochemical cells and the local temperature fluctuations due to the current flow introduces convection to the electrochemical cell which causes deviations from the expected behavior predicted by Cottrell equation.

Considering Eq. 1.4, Cottrell equation predicts a current that decays with a square root dependence which is a signature of a process under diffusion/mass transport limit which presents itself in various other forms throughout most electrochemical processes as will be shown for cyclic voltammetry as well.

Further extensions of the chronoamperometric techniques to yield steady state voltammograms and reversal experiments to probe reversibility of the systems along with other applications can be found elsewhere [22].

1.2.2 Cyclic Voltammetry

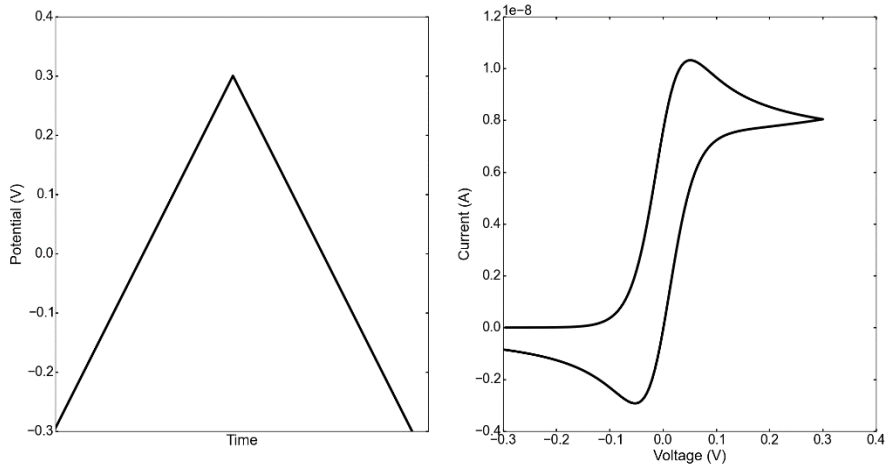

Figure 1. 6 The voltage profile applied in cyclic voltammetry and the resulting cyclic voltammogram.

In cyclic voltammetry, a linear potential that changes at a certain rate (called the sweep rate) is applied to the electrode. The name cyclic comes from the fact that the voltage is swept forwards and backwards between two potential limits at the specified sweep rate. As the potential approaches to values around the half-cell potential of the redox active material, a higher fraction of the electrode collisions result in reactions and current increases as a function of voltage, at some point however, a limit to the increment is achieved due to mass transport limits and the current no longer can increase. A geometrical way of visualizing the peak shape is shown in Figure 1.7. Electrochemical behavior of a system can be fully

characterized by collecting current data at closely separated potential steps as depicted [22]. A linear sweep corresponds to a slice in this surface as depicted[23].

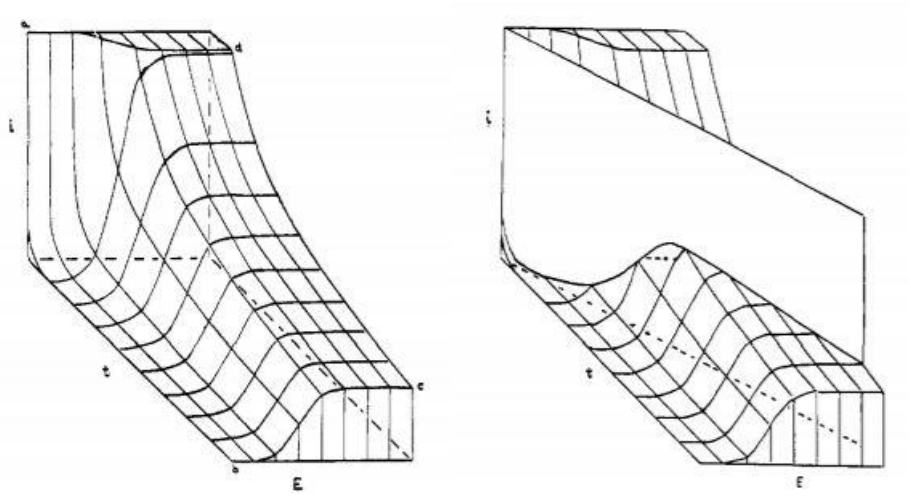

Figure 1. 7 Geometrical representation of a linear sweep in the current-time-potential surface. "Adapted with permission from [23]*. Copyright 1960, American Chemical Society."*

Similar to the Cottrell equation, solutions to the diffusion equations for various electrode geometries are numerically possible. The most prominent voltammetric feature is the peak in current observed in either scan direction and once both scan directions are plotted in the same plot, the so-called "duck" like shape is obtained. The mathematical treatment of the diffusion equations for cyclic voltammetry are more complicated compared to chronoamperometry because of the time varying potential applied. Still, depending on the applied potential and its value compared to the standard half-cell potential of interest, the current function at different times can be calculated numerically. Similarly, at the peak of this i-E curve, the current function can be evaluated as Eq. 1.5 and is called the Randles-Sevcik equation[24].

$$i_{peak} = (2.69\ x\ 10^5)n^{3/2}AD^{1/2}Cv^{1/2} \qquad (1.5)$$

As can be seen, the value of the peak current evolves with the square root of the sweep rate of the applied potential and again information regarding the diffusion coefficients of the system can be obtained through experiments at different sweep-rates. The information regarding diffusion coefficients, however, is not the reason why cyclic voltammetry is among the first techniques used in elucidating electrochemical behavior of novel systems, rather the information regarding the number of electrons involved in the redox reaction, the reversibility of the system, or whether a coupled chemical reaction occurs to the redox reaction taking place at the electrode makes cyclic voltammetry the technique of choice for almost all electrochemists. The details on how to extract this information can be found elsewhere [24].

The timescale of a cyclic voltammetry experiment is determined by the sweep rate of the applied potential. For instance, as an oxidizing potential is swept only the current response from the oxidizable species in the electrolyte solution that can diffuse from the solution to the electrode surface before the polarity/scan direction of the applied potential is reversed can be seen. The length from the electrode at which these species reside is called the diffusion layer as explained previously. By definition this length depends on the sweep rate. At high sweep rates the length of the diffusion layer is small while at low sweep rates the length of the diffusion layer is large. The ability to probe different timescales with a single experiment is among the reasons why cyclic voltammetry is such a versatile tool in investigating not only ion transport but also other novel systems[24].

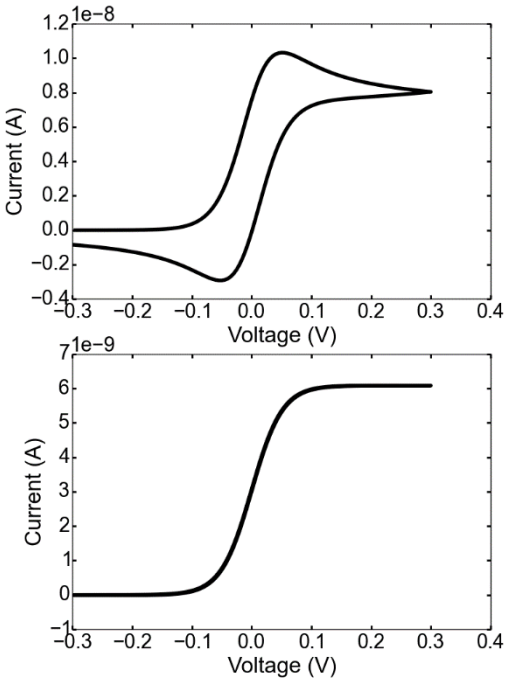

Figure 1. 8 Transient(top) and steady state voltammograms(bottom) of a fast redox couple simulated assuming equal diffusion coefficients of the oxidized and the reduced species (1e-5) at a hemispherical UME of radius 10 μm at 1 V/s and 0.001 V/s sweep rates.

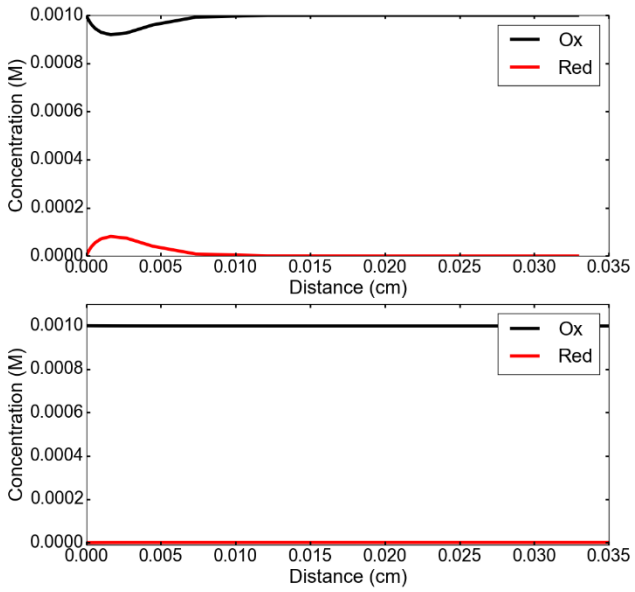

Figure 1. 9 The surface concentrations of the electroactive species under transient conditions (top) and under steady state conditions (bottom) at the peak potential.

Depending on the timescale of the experiment and the electrodes in question, the results of a given cyclic voltammetric experiment can vary greatly as shown in Figure 1.8. The cyclic voltammetry response of a hemispherical electrode at different timescales were simulated and a transition between the transient and steady-state voltammograms can be seen. The perfectly overlapping forward and backward sweeps show that the voltammogram is independent of the kinetics at the electrode for a steady state voltammogram while the peaks observed for the transient voltammogram suggests that the oxidation and the reduction reactions are displaced with respect to each other thus have kinetic contributions. For the simulated hemispherical electrode, two modes of diffusion can be imagined, a linear diffusion and a spherical diffusion. Spherical diffusion is much more effective in mass transport compared to linear diffusion due to edge effects [22]. At long timescales, the contribution from the spherical diffusion to the electrode dominates the response and as such the more effective mass transport results in the constant concentration profile observed in Figure 1.9. At short timescales, linear diffusion becomes more effective and dominates the current response, however, since it is not as effective in mass transport as spherical diffusion, electrode kinetics and various differences in the transport properties of the electroactive species results in the well-known transient cyclic voltammogram as shown in Figure 1.8.

Recently cyclic voltammetry investigations in model compounds (such as quinones) that undergo two consequent electron transfer reactions followed by a chemical reaction between these electroactive species in the following scheme were

conducted in weakly and fully supported electrolytes to elucidate the fine details in the electrochemical reaction mechanism involved.

$$Ox + e^- \rightleftharpoons Ox^-$$

$$Ox^- + e^- \rightleftharpoons Ox^{2-}$$

$$Ox + Ox^{2-} \rightleftharpoons 2Ox^-$$

The chemical reaction in the above mechanism is called a comproportionation reaction where Ox and Ox^{2-} are two reactants that have the same molecular formula, however at different oxidation states. The presence of this comproportionation step in a two electron transfer mechanism cannot be probed by conventional cyclic voltammetry in fully supported electrolyte solutions. As such two reversible redox waves of comparable peak size is seen in the conventional cyclic voltammetry regardless comproportionation occurs or not. In a weakly supported electrolyte, however, the second reduction wave, compared to the first oxidation has a noticeably smaller peak. This can be explained by the fact that the current at the second reduction peak is limited by the diffusion of neutral Ox species to the electrode in the absence of a comproportionation step. The diffused Ox undergoes two consequent and almost immediate oxidation steps to yield the current response. In the presence of a comproportionation step, however, the diffusion limit is imposed by the negatively charged Ox^- species whose transport can be effected by electric fields near the electrodes. In the properly supported medium, the electric field effects are nullified while in weakly supported electrolytes these differences can be measured through voltammetry[25]. This study not only highlights the inability of the conventional voltammetry to distinguish between mechanisms

under different ion transport regimes but also proposes a new tool in the electrochemical toolbox that is cyclic voltammetry in weakly supported electrolytes. Establishing novel methods to probe the effects of ion transport as previously explained is among the chief aims of this thesis.

The rest of this thesis is organized as follows: In Chapter 2 a method of measuring the electrochemical noise of commercial Li-Ion batteries and supercapacitors is outlined where the electrochemical noise should have information regarding ion transport phenomena occurring at the equilibrated state. A new offset reduction method is introduced and employed to accurately measure the electrochemical noise of batteries. Especially for primary batteries, electrochemical noise will be shown as a potential tool to characterize whether a given cell is shorted or not. In Chapter 3, a simple method that utilizes facile hydrogen transport through coated metal samples and pH indicators to reveal coating defects which is detrimental for overall coating integrity especially under corrosive environments will be outlined. Chapter 4 involves electrochemical investigations in an unconventional electrolyte, a Liquid crystal mesophase. The ability of this phase to stabilize thermodynamically unstable species for potential applications in Lead Acid Batteries will be shown, as well as fundamental investigations towards understanding the processes that govern this distinct behavior compared to their dilute solution counterparts will be discussed. In Chapter 5, an ultrafast potentiostat circuit with positive feedback on-line iR compensation will be discussed. Its potential in decoupling consecutive processes across multiple timescales will also be discussed. Moreover, developments towards a new spectroelectrochemical method, Ultrafast

Spectroelectrochemistry with a broadband UV-Vis spectrometer will be shown. Finally, in Chapter 6, a computationally inexpensive, coarse grained electrostatic model to explain the charge screening effects and the double layer formation kinetics at extended distances away from the point of contacts for an ionic liquid under external bias will be outlined. Through comparison between the described model and XPS results, insights towards understanding ion dynamics in this unconventional electrolyte will be discussed.

The unifying theme is developing an understanding of ion transport in an unconventional system (such as ionic liquids or liquid crystals) or attempts at improving on the state-of-the-art to extract further information regarding ion transport and ion transport controlled processes.

Chapter 2

2. A New Method for Voltage Noise Measurement and Its Application to Abused Primary Batteries

(This part is also described in **Can Berk Uzundal**; Burak Ulgut, *"A New Method for Voltage Noise Measurements and Its Application to Abused Primary Batteries", Journal of Electrochemical Society, Under Review.*

"Reproduced with permission from JES Copyright 2018")

2.1 Introduction

Ionic transport governs the operation and performance of a number of electrochemical devices. Information regarding the underlying processes within electrochemical systems can be extracted through processing signals that are either the results of applied external excitations or intrinsically generated.

Electrochemical noise measurements with the appropriate measurement and signal processing routines especially relevant in this regard where the noise measured is a vital indicator of the stochastic processes such as crevice and pitting in corrosion studies. The electrochemical noise literature is rich with both well-defined measurement systems and data analysis methods. Application of these methods to corrosion systems were thoroughly reviewed by Cottis[26]. Further, a guideline to standardize electrochemical noise in studies of corrosion were published by ECG-COMON[27]. If measured properly, even local behavior can be extracted from monitoring voltage or current noise of corroding systems[28–30]. Recently, electrochemical noise measurement of fuel cells and batteries have been attracting interest as a diagnostic tool due to the non-invasive nature of the measurement. Residual water content of the fuel cell, which is known to be detrimental, was shown to correlate with the electrochemical noise of the system[31]. On another example, calendar aging of supercapacitors were followed by careful investigations of their flicker noise [32]. In batteries, early reports of electrochemical noise measurements were conducted using aqueous chemistries as extensions to the corrosion studies. Lead-acid batteries were the focus of these reports where

electrolysis can be followed via noise measurements[33]. Similar measurements were further extended to Ni based aqueous systems as well[34,35]. Yet, noise measurements involving new generation batteries, especially Li-Ion batteries are sparse in the literature. Only recently, articles measuring voltage noise of commercially available Li-Ion batteries with very low backgrounds was published [36]. The conclusions drawn from this low background electrochemical noise data, however, is highly suspect since the published analysis suffers from lack of appropriate de-trending. The need for well-defined analysis methods and measurement techniques is clear. The apparent noise should be, unequivocally, from the battery while the numerical handling of the stochastic data should not introduce artifacts.

These techniques elucidate the underlying processes to both diagnose the state of the systems and also gain insights to increase next generation performances[37,38]. Especially for primary chemistries that are inherently not rechargeable, nondestructive/equilibrium techniques such as electrochemical noise is attractive where conventional techniques deplete the battery in question during the quality control process. For various other attempts at non-destructive battery quality control methods see the following references[39,40].

Though underappreciated in academic circles, the market share of the primary batteries are still expected to continuously grow in the near future and thus primary battery diagnosis is still an open question[41]. Primary chemistries are prevalently used in household items and medical tools due to their high and steady energy outputs in addition to their military uses.

Though both voltage and current noise are routinely measured in corrosion studies, due to the much lower noise levels, current noise measurements of batteries are dominated by the noise introduced to the system due to the noise in the applied potential. Therefore, noise studies on batteries are focused on voltage noise only [32–34,36] since the noise measurements can be performed without any applied signal under open circuit. For simplicity, throughout the rest of this manuscript, noise always refers to voltage noise.

In the literature, to draw both quantitative and qualitative conclusions from noise data, usually a background measurement is employed that involves a shorted lead measurement and resistors of relevant resistance levels[26]. Although resistor experiments can guide the initial inquiry, voltage noise of batteries are affected by issues that are not reflected in resistor measurements.

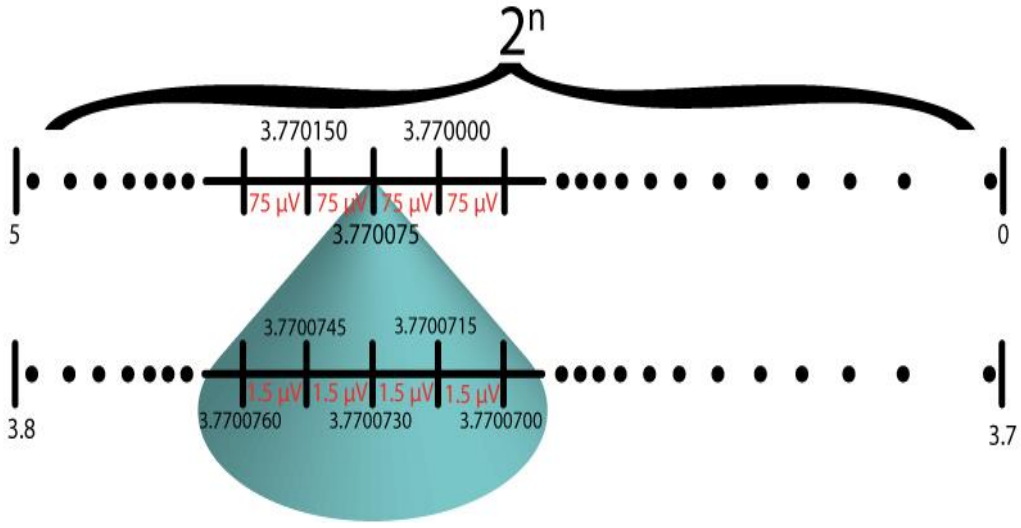

Figure 2. 1 Illustration of the increased resolution by offset reduction

An analog process that ends up introducing artifacts to the measured signal at amplitudes relevant to noise measurements (~µV) in batteries is offset subtraction.

Most instruments achieve high resolution even at high voltage amplitudes by offset subtraction and gaining the low residual as illustrated in Figure 2.1. The smallest voltage that can be measured above the quantization error is determined both by the amplitude of the voltage signal to be converted and the resolution of the A/D converter (given by the number of bits available). Roughly, offset correction subtracts the static part of the voltage from the whole thus reducing the voltage amplitude and increasing the resolution on the analog-to-digital converter. Our experiments show that this offset correction may significantly contribute to the apparent noise and can be circumvented by using another battery of the same voltage in an anti-serial connection (i.e. connected in series with same sign poles connected to each other) as shown in Figure 2.3. When two batteries are attached in parallel, they are at a high voltage amplitude (4.1V) which requires offset correction to achieve high resolution. During this offset correction, noise that stems from the instrument is introduced to the measurement. In the anti-serial connection, the voltage that needs to be measured by the instrument is effectively already offset corrected (it is at 0V) which enables the high resolution required for noise measurements. Offset correction by anti-serial connection achieves the high resolution required for battery noise measurements while mitigating the noise introduced by the electronic offset reduction.

2.2 Materials and Methods

SANYO 18650 Li-Ion batteries of 3400mAh capacity, MAXELL CR2032 (batch 63) coin-cells and 5F Nesscap Supercapacitors were procured from local suppliers.

Supercapacitors and the 18650 batteries were charged to the desired voltage and left to relax over a day such that voltage equilibration is complete (voltage changes less than 1mV/min) prior to noise measurement.

Impedance of primary batteries were measured galvanostatically with a DC offset of -2μA and AC amplitude of 2μA in the frequency region of 10mHz to 50kHz.

All measurements were done inside an earth grounded Faraday's cage to ensure the quality of the experiment. The energy storage devices were connected to the Gamry Interface 5000 in a two electrode configuration. ESA 410 software which specializes in measurement of electrochemical noise was utilized. Using this software, the potentiostat can be used as a galvanostat with an output frequency of 500 Hz and an output filter of 0.1%. The data was sampled at 500 Hz. Only for primary batteries the output frequency and the sampling rate was lowered guided by our initial experiments on primary batteries where the battery noise was mostly seen in the low frequency region. For these systems, the potentiostat was operated as a galvanostat with an output frequency of 5 Hz, sampled at 5 Hz.

The voltage noise measured has a contribution from the slow self-discharge of the batteries and various instrumental offsets. The analytical form of self-discharge can be extremely complex and may not be known[42] therefore directly removing it from the voltage noise with a non-linear fit is not viable. Instead a piecewise linear de-trend is used in the literature to remove this background[26]. The obtained de-trended voltage can be taken to the frequency domain and analyzed, however the voltage trace is not periodic but rather stochastic, thus limited insight is gained from

the f-domain traces. Electrochemical noise literature is rich with reports that highlight methods that prefer time domain analyses. Wavelet transforms capture finer details by applying non-periodic signals [43,44]. Recurrence Quantification Analysis shows the degree of repetition and correlation in the otherwise stochastic data[30,45] and Stochastic Process Detection (SPD) algorithm developed by Roberge can catalog stochastic events in terms of their shape to quantify trends[46]. For the purposes of this article, a plainer approach was taken and time traces were visualized using histograms.

Noise measured was first linearly de-trended by dividing the whole voltage trace into 1024-point chunks and individually subtracting the best-fit line from each chunk. This piecewise linear de-trended voltage is then either visualized using histograms of 64 bins or taken to the frequency domain using FFT and visualized.

All data visualizations and array operations were done in Python 2.7.10.0 using Matplotlib [47], Numpy [48] and Scipy under a Python(x,y) shell.

2.3 Results and Discussion

Apparent noise is a superposition of the actual noise of the battery and the noise introduced by the measurement instrument. Noise of the battery could be stemming from either faradaic or non-faradaic processes. In contrast to the earlier reports involving the noise of aqueous chemistries, electrolysis (faradaic contribution) is not a significant factor in Li-Ion batteries in the voltage ranges used and therefore the amount of noise is not as large. This puts the level of noise in an order of

magnitude where most of the noise that occur inside the battery should be shunted by the high capacitance of the electrodes[49]. To distinguish between these two distinct noise sources, supercapacitors are a valuable tool, since their charge storage mechanism is purely non-faradaic. If employed at the same voltage and with electrodes of similar capacitance as the electrodes of the battery in question, a supercapacitor is an ideal control sample for battery noise. The background provided by supercapacitor noise not only can distinguish between faradaic and non-faradaic sources of battery noise but also can show whether the apparent noise is an instrumental artifact.

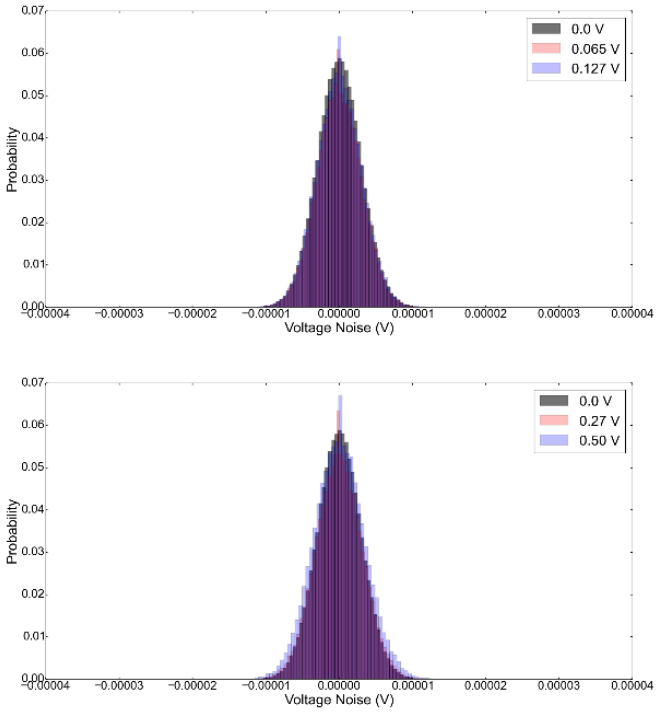

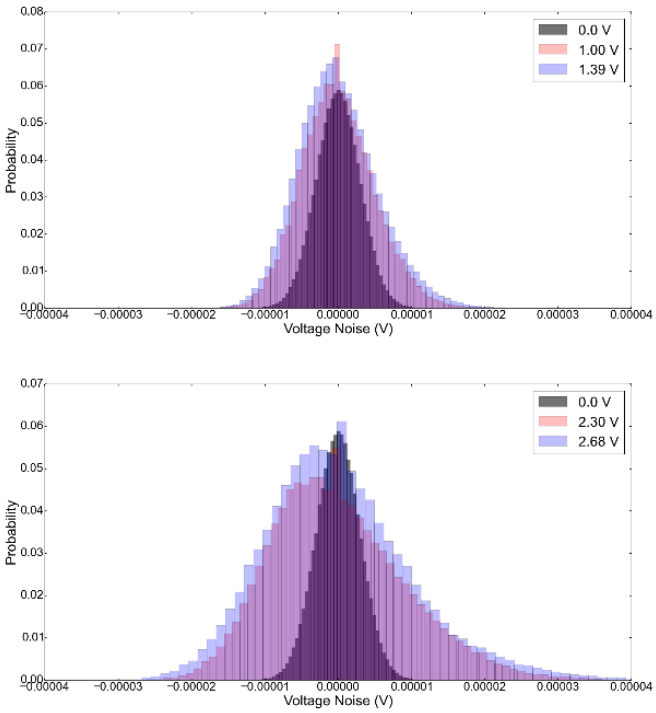

Figure 2. 2 Apparent noise of a 5F Supercapacitor at different states-of-charge.

Further, supercapacitors allow noise measurements at the low voltages that are not available within the operational window of a Li-Ion battery. Figure 2.2 shows the apparent noise of a 5F supercapacitor measured at different states-of-charge. The normalized histograms centered around 0 V widen with the increasing voltage of the supercapacitor, indicating an increase in the apparent noise. Similar experiments with batteries are much less conclusive as the available voltage window is much narrower.

If the observed increase in apparent noise is indeed due to the state of charge and not an instrumental artifact, apparent noise should show a similar behavior regardless of the average voltage measured by the instrument as long as the state of charge of the battery or the supercapacitor is preserved. Therefore, attaching another battery or supercapacitor of the same voltage (i.e. state of charge) in an anti-

serial connection should yield similar apparent noise profiles. However, the apparent noise at these voltages when two supercapacitors are connected in an anti-serial connection yields an apparent noise that is similar to the shorted lead of the instrument. Although this shows that the apparent noise is an instrumental artifact at these voltage amplitudes, the possibility of using supercapacitors as a background measurement for voltage noise and the higher voltage sensitivity achieved by the anti-serial connection needs to be highlighted. In this chapter, we report on the enhanced voltage resolution enabled by the anti-serial connection to measure the noise of Li-Ion batteries.

In order to accurately offset the DC voltage, the two cells to be connected anti-serially have to be at precisely the same potential. Therefore, the best experimental workflow is to keep the cells connected in parallel to force the potentials to be the same, let them equilibrate to the same potential and then switch to the anti-serial connection for the noise measurement without any need for an electronic offset correction. Therefore, a simple switch was designed to alternate between parallel and anti-serial connections as shown in Figure 2.3. This ability to quickly alternate between parallel and anti-serial connections helps with equilibrating the two batteries to the same potential using the parallel connection and quickly switching to the anti-serial position to achieve zero overall potential.

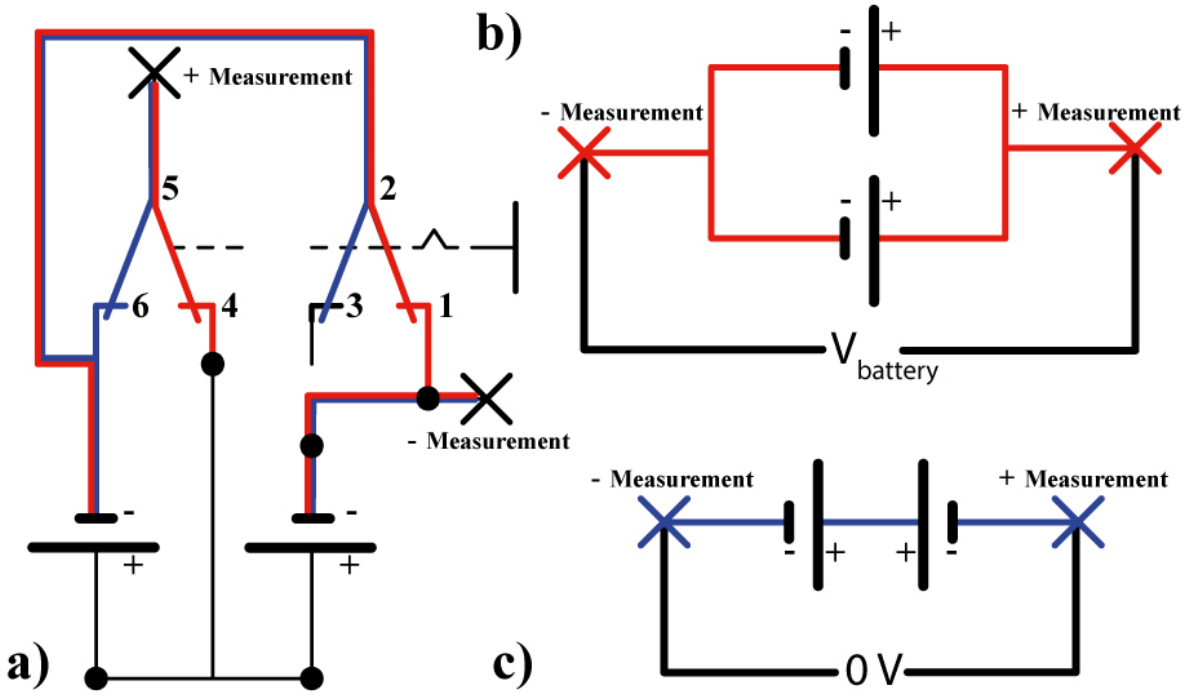

Figure 2. 3 a) Sliding switch that changes connections from parallel (red) to anti-serial (blue). b) When the connections 1-2 and 5-4 are selected, the batteries are in parallel as shown. c) When the connections 3-2 and 6-5 are selected, the batteries are in anti-serial as shown.

2.3.1 Comparing Instruments

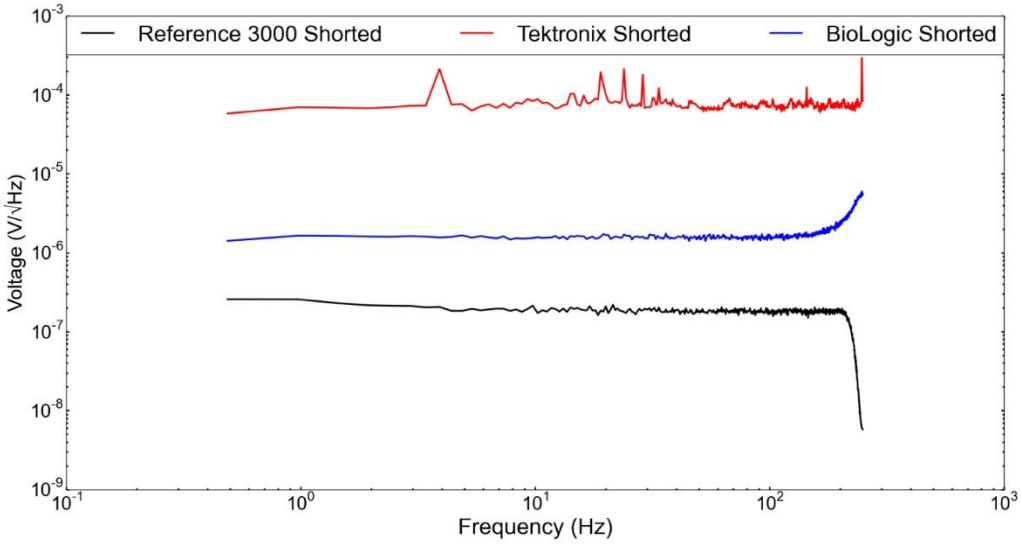

Figure 2. 4 Shorted lead noise of Tektronix DPO 2002B, Bio-Logic SP-150 and Gamry Reference 3000 in the f-domain.

In our studies we used potentiostats from two different manufacturers and an oscilloscope. In Figure 2.4, shorted lead noise of these instruments are shown. The need for specialized instruments for noise measurements is clear where the background noise of various instruments can range almost 3 orders of magnitude. As can be seen from the f-domain traces, the apparent noise is much higher for the Tektronix oscilloscope. This baseline renders the oscilloscope unsuitable for battery noise measurements. The higher apparent noise of Tektronix is partly due to aliasing where the bandwidth (20 MHz) of the instrument far exceeds the frequency regions of interest (250 Hz) and the relatively low input impedance (and high input bias current) of the oscilloscope to achieve this large bandwidth. The effects of aliasing can be seen in the frequency domain as sharp features at much lower frequencies. To remove these aliasing frequencies a low pass filter should be put in

place. The effect of analog filtering on the data is seen on the frequency domain of the shorted lead of the Gamry Reference 3000. Aside from the overall lower noise, caused by a lower input current, we observe two striking changes in the frequency domain. First, the sharp features seen in the Tektronix shorted lead is lost, since they can no longer alias. Second, the high frequency end of the Reference 3000 shows a cut-off. This is a direct result of the hardware filter.

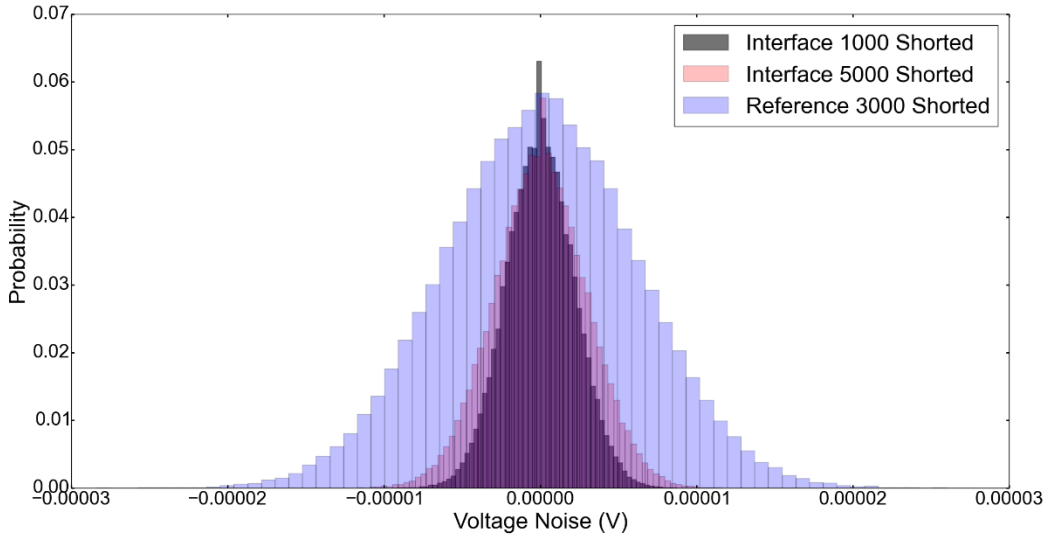

Figure 2. 5 Shorted lead noise of various Gamry instruments potentiostats.

It is clear that the apparent shorted lead noise of instruments from Gamry is much lower which should allow for much cleaner measurements compared to other instruments in this study. Even among the instruments of the same manufacturer there are slight differences in apparent noise such that a clear choice can be made to minimize it as seen in Figure 2.5. Since this difference is much smaller, it is more appropriately shown on a linear scale in a histogram plot, instead of a logarithmic f-domain plot.

2.3.2 Electrometer Stability

A factor that complicates these noise measurements is the fact that electrometers tend to oscillate when large capacitive loads are attached. Though the results shown in Figure 2.2 were without any modifications to the anti-serial/parallel switch, oscillations were commonplace for all the instruments.

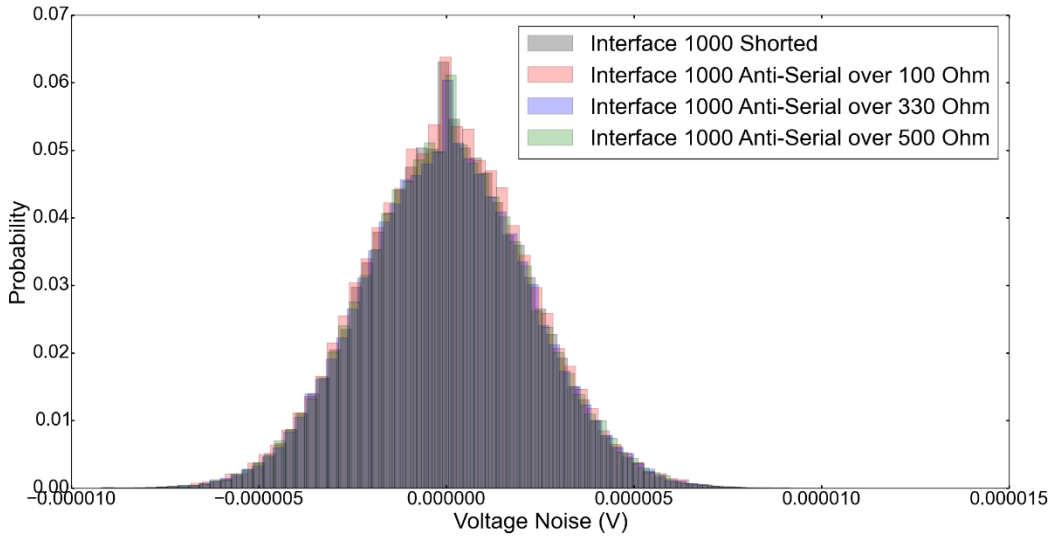

Figure 2. 6 Apparent noise at 4.1V in the anti-serial connection measured over various resistances and compared to the shorted lead of Gamry Interface 1000.

The simplest approach that improves the stability is to ground one of the inputs of the instrument, adding, an albeit small, resistive component to the otherwise capacitive load which removes the oscillations. The quality of the ground connection, however, is crucial, where a clean ground connection may not always be available. Another simple solution is to introduce a parallel resistor to the anti-serial/parallel batteries, over which the voltage noise can be measured. Similar to grounding, the added resistance improves stability substantially. Adding a resistor to the noise measurement setup, brings concerns over the increased noise. The

Johnson noise introduced by a 100 Ω resistance at room temperature with 250 Hz bandwidth is roughly 20 nV, which is negligible given the levels measured and therefore does not contribute to the apparent noise significantly as seen in Figure 2.6.

2.3.3 18650 Li-Ion Battery Noise

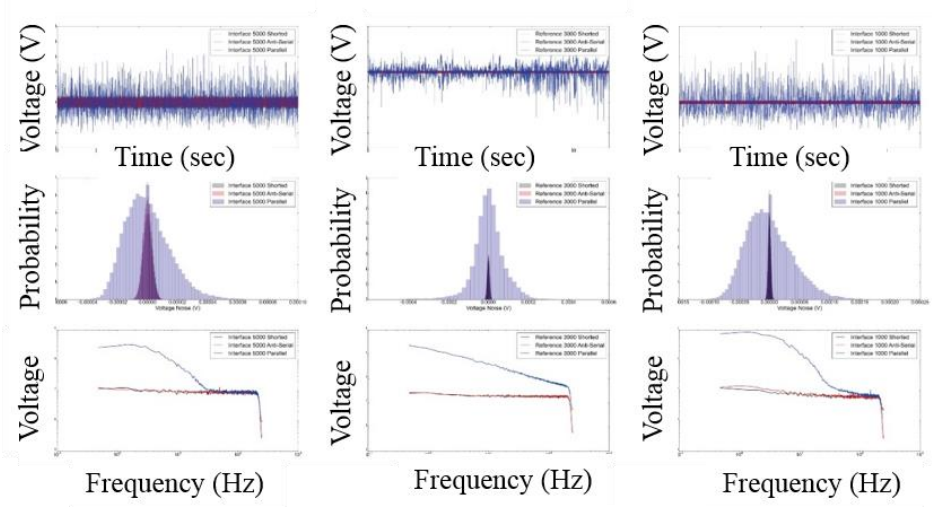

Figure 2. 7 Voltage noise of a Li-Ion battery at 4.1V in parallel and anti-serial configurations compared to the shorted lead measured using Interface 5000, Reference 3000.

In a case where the apparent noise is purely of the battery, the anti-serial connection would show noise levels similar to or exceeding the single battery measurement. This was not seen for the noise of 18650 Li-Ion batteries charged to 4.1V. Apparent noise of two 18650 batteries connected in a parallel connection reduces to the same level as the shorted lead noise of the instrument when attached in an anti-serial connection (Figure 2.7). The apparent noise of the parallel/high amplitude case being significantly higher, while, the apparent noise of the anti-serial connection being the same as the shorted lead, proves that the apparent noise is *dominated by instrumental artifacts at high voltage amplitudes*. Considering that the large

capacitance of the high surface area electrodes damp the effects of events on electrodes[49], instrumental factors that contribute to the apparent noise should be fully accounted for. Among these instrumental factors the input bias and the oscillations of the electrometer in the frequency region of interest should be minimized. For a given instrument changing these factors is, in most cases, not possible.

2.3.4 De-trending

Using the anti-serial offsetting scheme outlined in this article does not fully mitigate the need to de-trend the apparent noise, where small drifts in voltage can still occur. Commercial batteries of the same manufacturer, even from the same batch, have slight differences in terms of their impedance and capacity[50]. This alone can cause a slight drift, which should be de-trended as shown in Figure 2.8. If the measured noise is not de-trended, it is easy to draw ill-guided conclusions guided by the statistics of a should-be stationary system applied to a non-stationary one. Especially noise power analysis and high order statistics are known to be highly susceptible to drift[26].

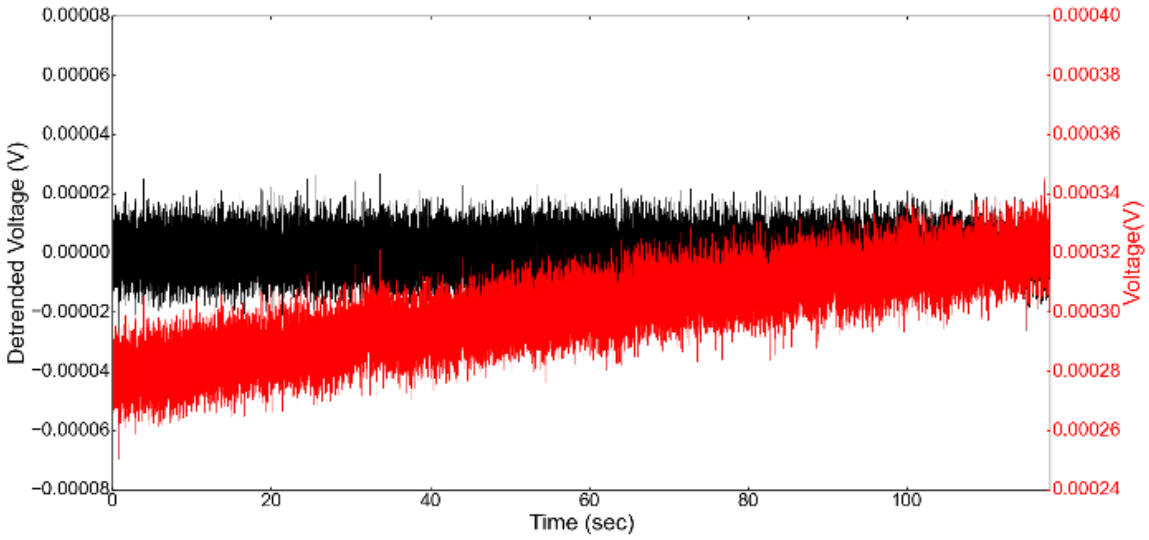

Figure 2. 8. Apparent noise at 4.1V, de-trended time trace shown in black and the pristine trace is shown in red.

2.3.5. Primary Li-Ion Battery Noise

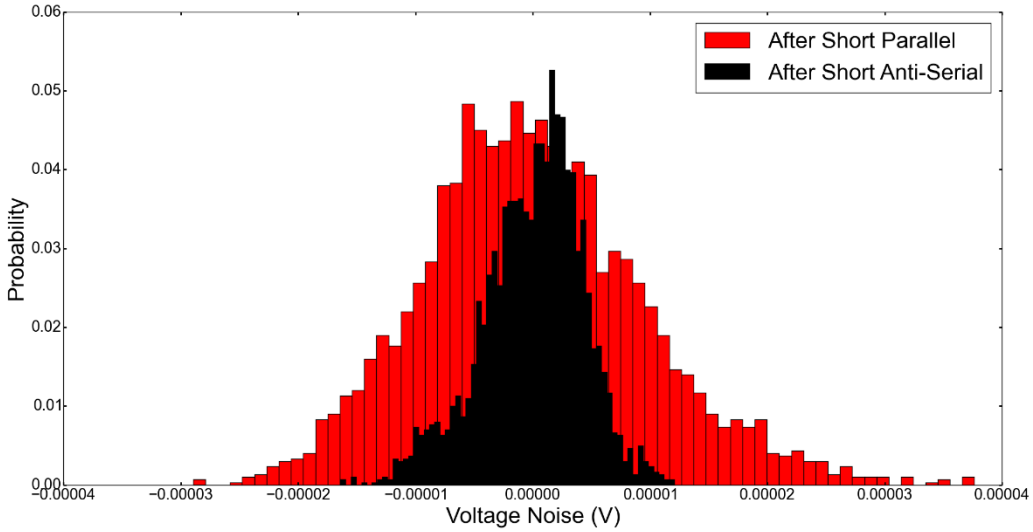

Figure 2. 9 Noise of the same two CR2032 batteries compared in anti-serial and parallel connections after short circuiting the batteries.

Discussions outlined in the above sections form a basis for the proper measurement of battery noise. As discussed, the large capacitance of the 18650 Li-Ion batteries

lowers the noise amplitude and render them practically unmeasurable with our instruments. Thus smaller batteries are expected to be more amenable for noise measurements. As such, we selected CR2032 coin-cells and measured their noise. Another added benefit of this chemistry (primary $LiMnO_2$) in this geometry is the relatively high internal resistance (100Ω) which improves the electrometer stability. Further, in order to mitigate the adverse effects of the high frequency noise components in time domain analyses, a narrower bandwidth of 2.5Hz is chosen in these measurements.

The apparent noise at 3.2V without applying the anti-serial connection outlined in this article shows a noise signal that vanishes when attached in the anti-serial connection. The disappearance of the noise signature to the shorted lead levels in the anti-serial connection again confirms that the noise measured at the high amplitude is an instrumental artifact introduced by the offset correction scheme employed by the instrument. The increased voltage resolution of the anti-serial case is evident when comparing the apparent noise histograms obtained under same conditions for the parallel and anti-serial connections as shown in Figure 2.9. Individually shorting these batteries and measuring the noise once they settle, however, yields a remarkable increase in the measured noise (Figure 2.10-a). An appropriate background for the anti-serial connected batteries is the apparent noise measured over a resistor of comparable resistance. For the batteries after shorting, the internal resistance increases significantly and approaches around 1kΩ. This background is not appropriate for the noise measurements in the parallel connection due to the above discussed offset correction artifacts introduced by the instrument

to the measurement in question. Instead the noise of the pristine battery can be taken as the apparent noise floor. Clearly after short circuiting the batteries, the apparent noise rises above the noise floor for the anti-serial connection while for the parallel connection no such increase can be discerned. The inability of the parallel connection to catch the noise signature of the battery is expected especially when we compare the voltage amplitudes at which the battery noise occurs as shown in Figure 2.9 (around 4 times lower than the smallest voltage measurable in the parallel case). When the external short circuit is lifted, the coin-cell recovers its voltage over time (as confirmed by the impedance and the voltages of the cells). The origins of this noisy recovery is currently under investigation. Clearly the obtained noise profile has information regarding the processes taking place in the battery similar to the corroding systems (Figure 2.11-a), however the stochastic nature of the data, as seen by the frequency domain responses, complicate the quantification (Figure 2.11-b) and consequently identification of these processes. The need for reliable time domain analysis methods is again stressed for proper quantification of these stochastic processes.

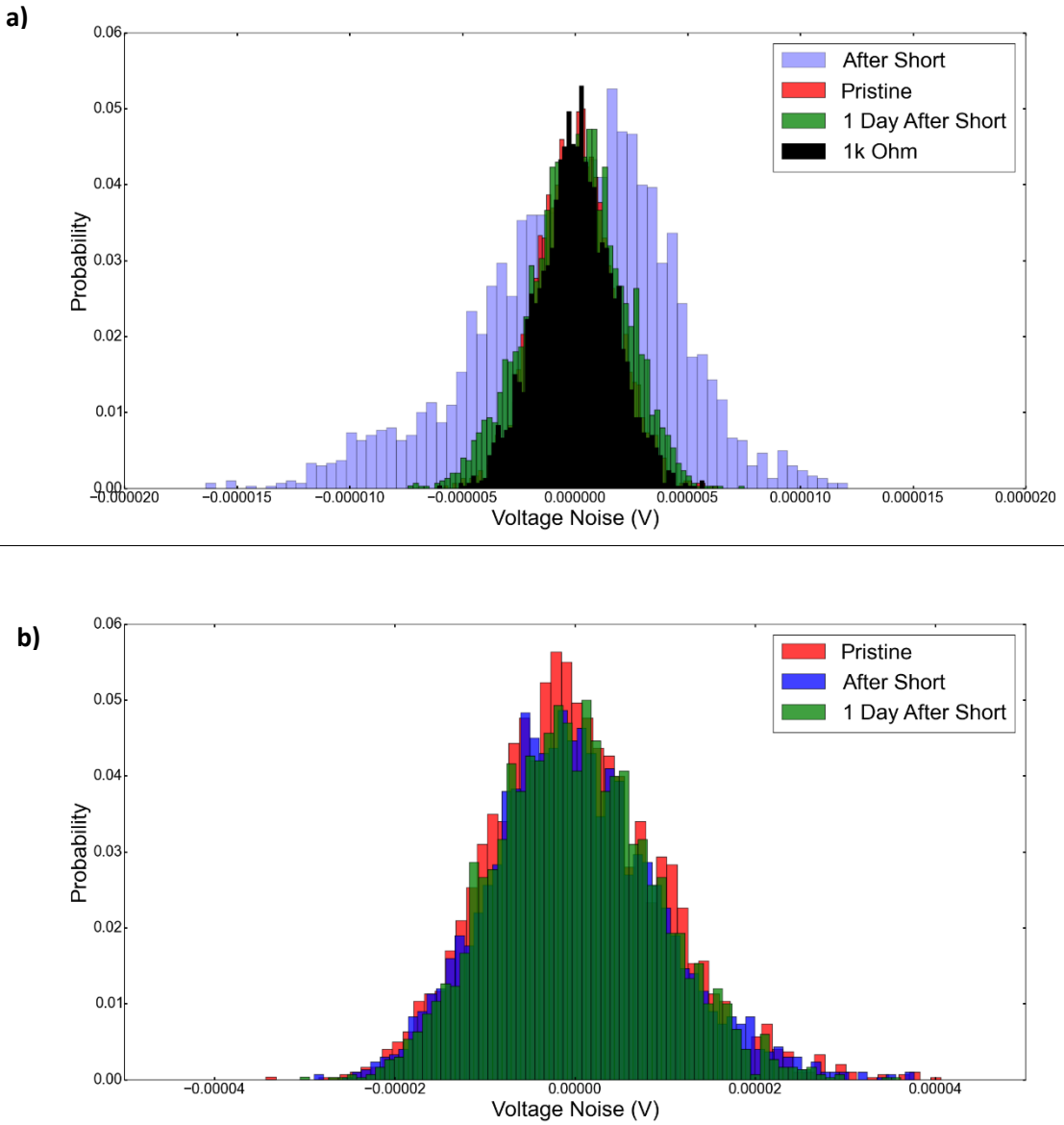

Figure 2. 10 a) Noise of two CR2032 coin-cells attached in anti-serial connection. b) Noise of the same two CR2032 coin-cells attached in parallel connection. (Figure 2.5 serves as a scale for these two graphs for ease of view.)

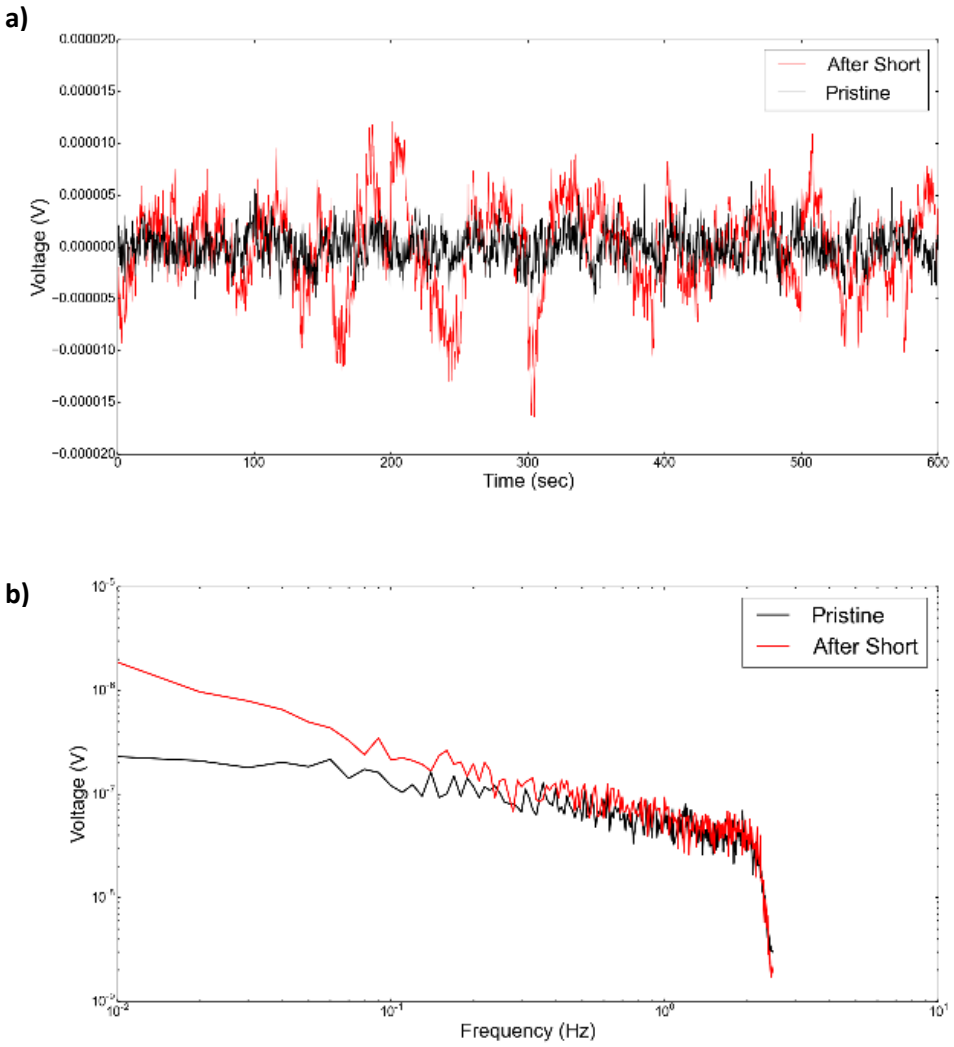

Figure 2. 11 Noise of two CR2032 coin-cells attached in anti-serial connection a) in the time domain. b) in the frequency domain.

2.4 Conclusions

Offset correction by anti-serial batteries proved to be an effective approach in differentiating between the apparent noise and the actual noise of the system. The instruments available were pushed to their limits and improved upon by the new offset reduction scheme. Although the battery noise of the large Li-Ion batteries remains elusive and not detectable within the detection limit of our instruments,

electrochemical noise of smaller coin-cells was detectable after suffering a short .

Chapter 3

3. Method for Visualizing Under-Coating Corrosion Utilizing pH Indicators before Visible Damage

(This part is also described in **Can Berk Uzundal**; Burak Ulgut, *"Method for Visualizing Under Coating Corrosion Utilizing pH Indicators before Visible Damage", Progress in Organic Coatings 2018 122: 72-78. "Reproduced with permission from* [51] *Copyright 2018")*

3.1. Introduction

Ion transport through metals in addition to ion transport in electrolytes, is also a process that can be employed for practical purposes. In this particular example, the transport of adsorbed hydrogen into the metal surface and defects is going to be employed for practical purposes.

Detecting under-coating corrosion is of importance in assessment of stability and integrity of coated metal samples. When fully coated, metal samples corrode sparingly. Corrosion mainly takes place in regions where cuts, cracks or scratches are present. Unless these faults are macroscopic, they are not easily detectable. From these positions corrosion propagates laterally and eventually disrupts coating integrity [52]. Under operational conditions, defects in the coating can result in the failure of the system. Evaluation of coatings and their anti-corrosive properties require facile and non-destructive methods. In the literature, a variety of methods spanning Electrochemical Impedance Spectroscopy (EIS) and Scanning Electrochemical Microscopy (SECM) are present for comparison of various coating materials[53–58]. Moreover, utilizing high frequency waves such as terahertz waves or near-field microwaves, local corrosion can be detected in the bulk scale. These high frequency detection techniques, however, depend on the dielectric differences between the paint, metal and the metal oxide which limits their applications as in the case of aluminum plates where dielectric constants are similar[59,60]. With these high frequency techniques, formation of the metal oxide cannot be visualized before a significant amount of metal oxide forms and the paint

swells, thus severely limiting their detection capabilities.

Employing EIS approaches to detect under paint corrosion can deduce the effects of somewhat local changes through changes in the parameters of equivalent circuit models. Yet, the precise location of the change cannot be found on the metal plate. Truly local information on under-coating corrosion can be obtained by SECM. SECM however, requires sophisticated equipment and is not readily available for routine analysis. Further, scanning large areas in SECM requires a long time and very large equipment. In fact, an SECM study conducted on aluminum alloys which show generation of H_2 and H^+ at regions of coating defects due to exposed metal sites, inspired us in developing our methodology [54,58].

In our methodology, partially inspired by the work of Devanathan, we sought to design our experiment around the H^+ that is generated in the coating defects of the coated sample[61,62] . In the classical Devanathan experiment, a metal plate is fixed in between a two compartment cell (see Figure 3.1) where on one compartment H_2 is formed by a cathodic potential while on the other compartment the diffused H is oxidized into H^+ by an anodic potential. On the latter, the current generated is monitored which yields the diffusion rate of H. The method since then, is standardized for measurement of diffusion coefficients in metal plates and measurement of metal plate thickness[63]. Recently methods that build on the classical Devanathan experiment to probe the oxygen reduction kinetics at a coating-metal interface was developed [64,65]. Although the reported approach can be used to assess overall coating integrity, local information cannot be deduced. In terms of local resolution, the potential of the Devanathan experiment was

demonstrated via Scanning Kelvin Probe Microscopy, where hydrogen permeation through micro-domains of various metals could be discerned[66].

Herein we present a modification to the Devanathan experiment to tap into the local information inherently present through a very simple visualization method: Inspired by the work of Jin et. al. where they utilize a pH indicator to visualize local regions of low pH as a result of higher catalytic activity towards methanol decomposition[67,68], we also add a pH indicator to our two compartment Devanathan setup.

3.2 Experimental

3.2.1 Method

Between the two compartments of the designed cell (see Figure 3.1), a metal plate (aluminum 2024 of 0.2mm thickness) is fixed. The bottom compartment is the generator cell where H_2 is generated by a reducing potential, while the above compartment is the detection cell where the diffusing H is oxidized into H^+ by an oxidizing potential. The generator cell contains saturated brine (saturated aqueous NaCl solution) while the detection cell contains brine adjusted to pH 9 or pH 6 (for phenolphthalein or quinine respectively) with NaOH. As the indicator, a couple drops of phenolphthalein or 370 mg/L quinine is added. One separate, floating potentiostat is attached to each compartment in a two electrode configuration where two graphite rods are used as both counter and reference electrodes in a two electrode configuration and the metal sample in the middle is the working electrode for both potentiostats. To the generator cell a negative constant potential is applied

while to the detection cell, a small positive potential (0.5 V) is applied to generate H_2 and to oxidize H into H^+ respectively. Magnitude of the potential applied on the generator cell depends on the nature of the metal sample and the ability of the metal to catalyze the hydrogen formation reaction such that the metal surface is covered with hydrogen completely. As the size of the hydrogen bubble increases the current supplied drops since the electrical contact between the metal and the solution is cut off from the generator side. The complete hydrogen coverage ensures a uniform start of diffusion across the metal sample. Routinely, potentials around 10 V were applied. A constant current cannot be imposed on the metal without overloading the potentiostat attached to the generator cell since the hydrogen bubble that forms blocks the current.

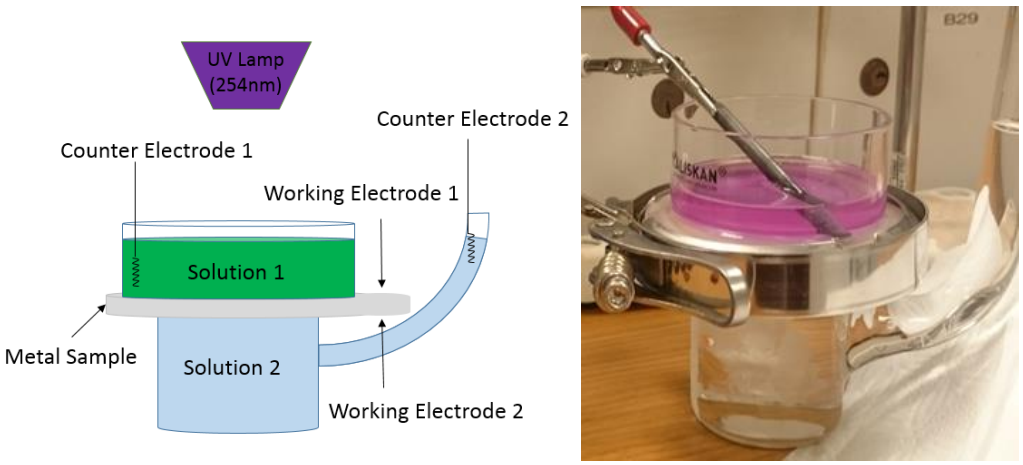

Figure 3. 1 Schematic representation of the setup (left). The actual setup (right).

Floating potentiostats are an absolute necessity in this setup since a single metal electrode acts as the working electrode of both the generator and detection cells. If two earth grounded instruments were employed, applying different potentials on the two cells would not be possible since the ground in each instrument would be fixed to the same point. Floating the potentiostats allow for the grounds of each

potentiostat to be at a different level with respect to the earth ground, allowing the application of different potentials.

In our setup, a Gamry Instruments Interface 5000E was used for the generator cell and a Gamry Instruments Interface 1000E was used for the detection cell.

For experiments conducted using phenolphthalein indicator, a camera was fixed over the electrochemical cell. The fixed camera ensures that background subtraction could reliably be made.

3.2.2 Image Processing

To increase the clarity of the images taken with phenolphthalein indicator, a background subtraction routine was utilized. Simply, the images are imported as arrays of RGB values (Red-Green-Blue) into a Python 2.7 environment. Each of the color channels individually are normalized using the following simple formula to account for minor changes in ambient light.

$$Let\ "C"\ be\ Red, Blue\ or\ Green\ Channel$$

$$Normalized\ C = \frac{C - \min(C)}{\max(C) - \min(C)} * 255$$

Then, using GIMP 2.8 image processing software, the contrast of the background subtracted images were enhanced. The contrast of an image can be thought as the difference between the brightest pixel and the darkest pixel. When the contrast of an image is increased, this difference is enhanced by making the darkest pixel darker while the brightest pixel is made brighter, where all three channels are considered in unison. The contrast enhancement was done to increase the clarity of

the images such that colors can be visualized regardless of the medium this thesis is presented (in print or in web).

For a select case, color reduction was employed to even further enhance the contrast of the images. The GIMP algorithm for color reduction is based on the following simple algebra[69];

$$Let\ "C"\ be\ the\ array\ of\ values\ corresponding\ to\ Red, Green\ or\ Blue\ channels\ with\ floating\ point\ values\ ranging\ between\ 0\ and\ 1$$

$$Color\ reduced\ C = round\left(\frac{C * \#\ of\ colors}{\#\ of\ colors}\right)$$

$where$ "# of colors $denote$" $the\ number\ of\ colors\ in\ the\ color\ reduced\ image.$

Quantification shown in Figure 3.7, is made easier using color reduction where color reduction lumps colors within a close region of color space to a single color. The size of this region is determined by the number of colors specified. Using color reduction, slight off-colors are assigned as pure green and can be accounted for in the quantification. Similar to contrast enhancement, color reduction also increases the clarity of the article in different media.

After normalization and color reduction (where applicable) the first image is subtracted from rest of the images by a simple array operation.

Throughout the article and the supporting information, the images are presented with their originals and their processed version.

In terms of quantification of the color reduced images, a 300-pixel by 300-pixel region was selected (shown in Figure 3.7). If all the pixels in the region was purely green, the total green content of the region would be 300x300x255 where the color in any channel can be a number ranging from 0 to 255. Thus, summing the green

channels of all the pixels in the region and normalizing with respect to 300x300x255, we can get a relative quantification on the amount of green in the region as shown in Figure 3.7.

3.2.3 Materials

For metal plates of different sizes, two different cells were used throughout the experiments with the same basic schematic shown in Figure 3.1. The larger cell had a detection cell outer diameter of 8 cm, the smaller cell had a detection cell outer diameter of 3.5 cm.

The experiments with the white plate and the bare metal were done using the small cell while the experiment involving the epoxy coated metal sample was conducted using the large cell due to the size differences of the samples.

Following mechanical abrasion with sandpaper (grit size P120), the metal samples were either exposed to polarization directly, or were coated with Bison 5-minute epoxy (Goes, The Netherlands) prior to being exposed to polarization. The epoxy coated samples had a total thickness of 1.6 mm. The white painted sample was procured from a local supplier.

3.3 Results and Discussion

3.3.1 Methodology

As mentioned in the introduction, following the SECM report that shows the evidence of elevated H_2 generation in the defects of coated samples, we speculated that H^+ could be generated in the reverse fashion, if H_2 is present in sufficient

amounts[54,58]. We utilize a Devanathan-like cell where H_2 is generated in the generator cell. The generated H_2 diffuses through the metal matrix and travels to the detection compartment due to the H_2 concentration gradient. When the diffused H encounters the oxidizing potential of the detection cell, it is oxidized into H^+. This oxidation is expected to occur at exposed metal sites where the metal site catalyzes the reaction. Even if H^+ is formed in regions without defects, the H^+ is expected to diffuse laterally to the defect sites where it is exposed to the solution containing pH indicator. The H^+ generated locally results in regions of low pH which is visualized by the pH indicator as can be seen in Figures 3.2-4.

3.3.2 Choice of Indicator

Our initial experiments used phenolphthalein as the indicator of choice simply due to its availability. Broadly, in around a minute, we saw the disappearance of the pink color upon the applied potentials thus indicating the generation of H^+ as expected (Figure 3.2). The loss of color, however, is hard to identify to the naked eye except when it occurs in bulk. Emergence of a color, on the other hand, would be straightforward to identify, especially if the color occurs from a transparent solution. An indicator that covers all these bases is quinine. Under UV, it is fluorescent at acidic conditions while being non-flourescent under basic conditions (pKa = 4.5).

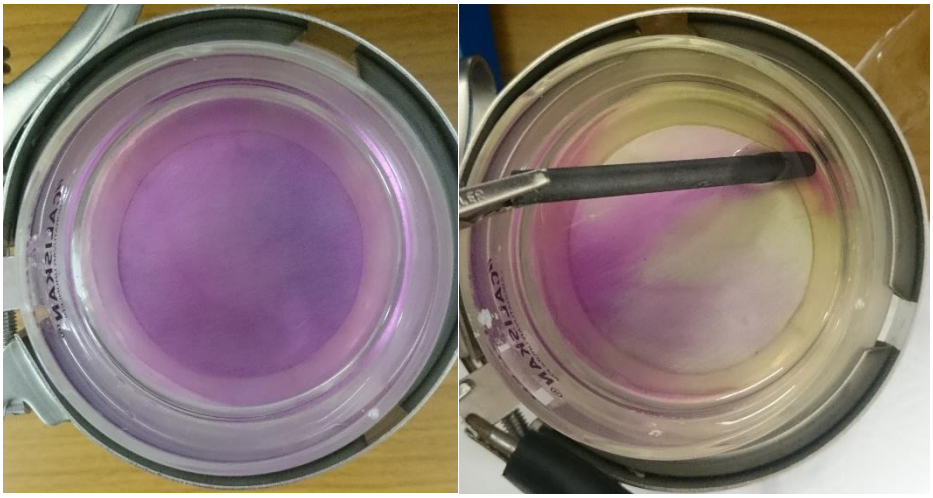

Figure 3. 2 The initial experiments with phenolphthalein indicator. Loss of bulk color can be seen on the right.

The major problem with quinine is its fluorescence quenching in the presence of halides, in particular chloride [70]. Since corrosion studies in sea-water/salt-water is industrially relevant in assessment of coating integrity, using quinine is not suitable for these applications. Further, metals coated with 5-minute epoxy, any kind of non-uniformity (bubbles, scratches etc.) and most TiO_2 based white paints are fluorescent under UV (254 nm), which interferes with the observation of fluorescence from quinine. Still, as a proof-of-concept to showcase the methods ubiquity in terms choice of indicator, the detection cell was filled with 0.1 M Na_2SO_4 containing 100 mg/L quinine. As prepared, the solution is not fluorescent (pH 6). Upon applied potential, however, fluorescence clearly emerges as shown in Figure 3.3. Similar experiments conducted with brine only shows faint fluorescence which is hard to observe. The chloride quenching limiting the applicability of the method and coating defects being fluorescent urged us to pursue an alternative indicator for our method.

Figure 3. 3 Bare metal with 0.1 M Na2SO4 containing 100 mg/L quinine, the initial picture without any fluorescence and the emergence of fluorescence with applied potential.

3.3.3 Background Subtraction

Reflecting back on the experiments with phenolphthalein, where apparent color changes were occurring, the only hurdle was our inability to observe the loss of color from the background pink of the indicator. If we were to remove this pink background, we would effectively change the response of the indicator from a color loss to an emergence of color. Fixing a camera to a certain position and then subtracting the first image (where no potential is applied) enabled us to observe localized color changes.

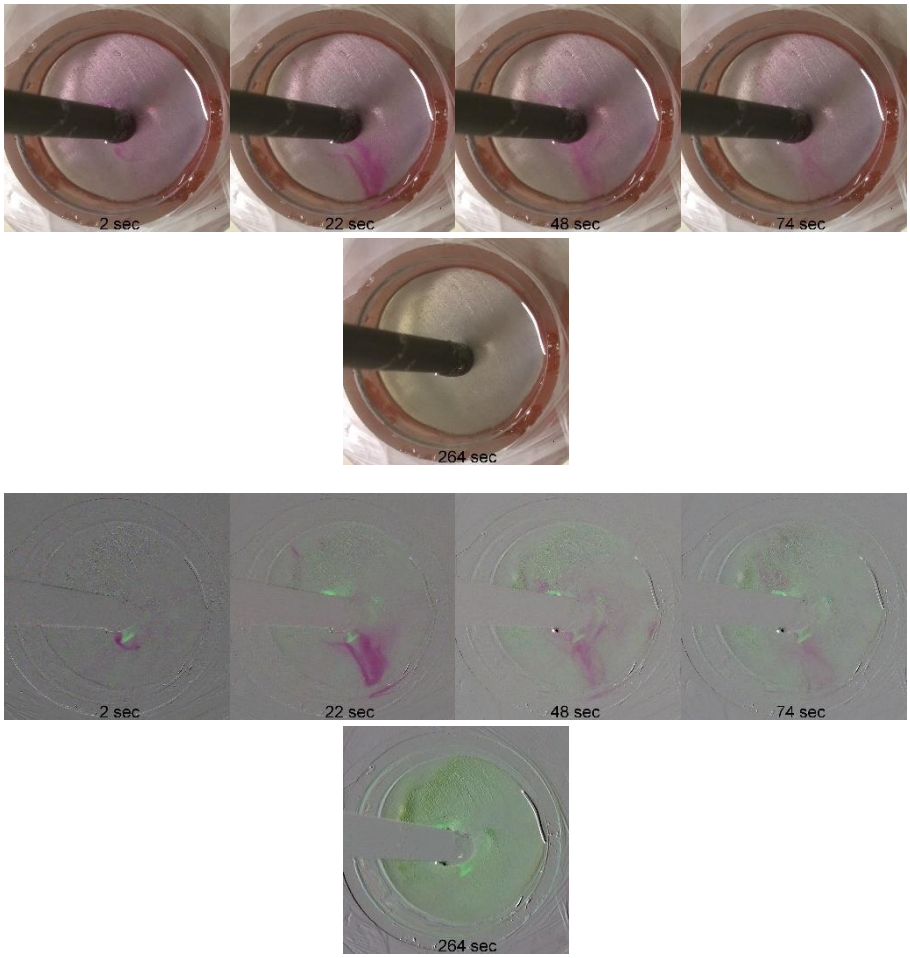

Figure 3. 4 Background subtracted images (bottom), unsubtracted images (top). Green color indicates regions of low pH while red indicates an increase in pH.

Figure 3.4 serves as a proof of concept where a metal sample (cleaned by mechanical abrasion grit size P120) is exposed to the procedure in the presence of phenolphthalein in brine adjusted to pH = 9 with NaOH. Due to the background subtraction, loss of pink/red is characterized by its complementary color, green. The red/pink spots in the background subtracted images signify elevated pH compared to the initial solution which is usually due to the counter reaction. As expected, for the bare metal, H^+ generation occurs throughout the solution uniformly as indicated by the overall green color of the background subtracted image.

3.3.4 Visualization of Local pH Gradients with Phenolphthalein Indicator

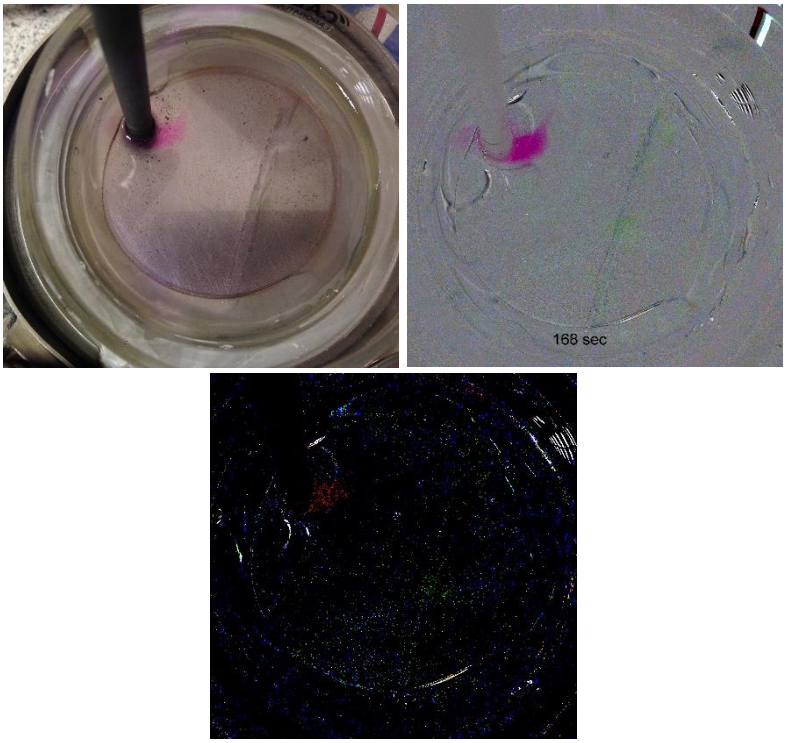

Figure 3. 5 The original image (left), background subtracted image (middle), background subtracted image with number of colors reduced to 4 (right).

To test whether we can observe the color change locally, we used a 5-minute epoxy coated metal sample with a cut. To improve the clarity of images, after background subtraction we reduced the number of colors in the image to 4. Though even in the background subtracted image faint green spots were visible, in the color reduced image the locations of lower pH are more evident (Figure 3.5). Moreover, to minimize the effect of the counter reaction on visualization, we moved our counter electrode to the opposite corner. The color reduced images in Figure 3.6, shows evidence of lower pH regions along the cut on the epoxy. No visible corrosion is yet seen, however at the end of the experiment, visible corrosion occurs along the cut. Thus, with background subtraction corrosion can be observed prior to any visual confirmation beyond the local pH changes.

It is possible to quantify the green intensity locally along the cut as demonstrated by Figure 3.7, where we selected a square region on the cut and plotted the amount of green in it. The intensity is normalized such that if all the pixels in the square are fully green, intensity would be 1.0. After about 450 seconds, significant increase in green intensity can be quantified.

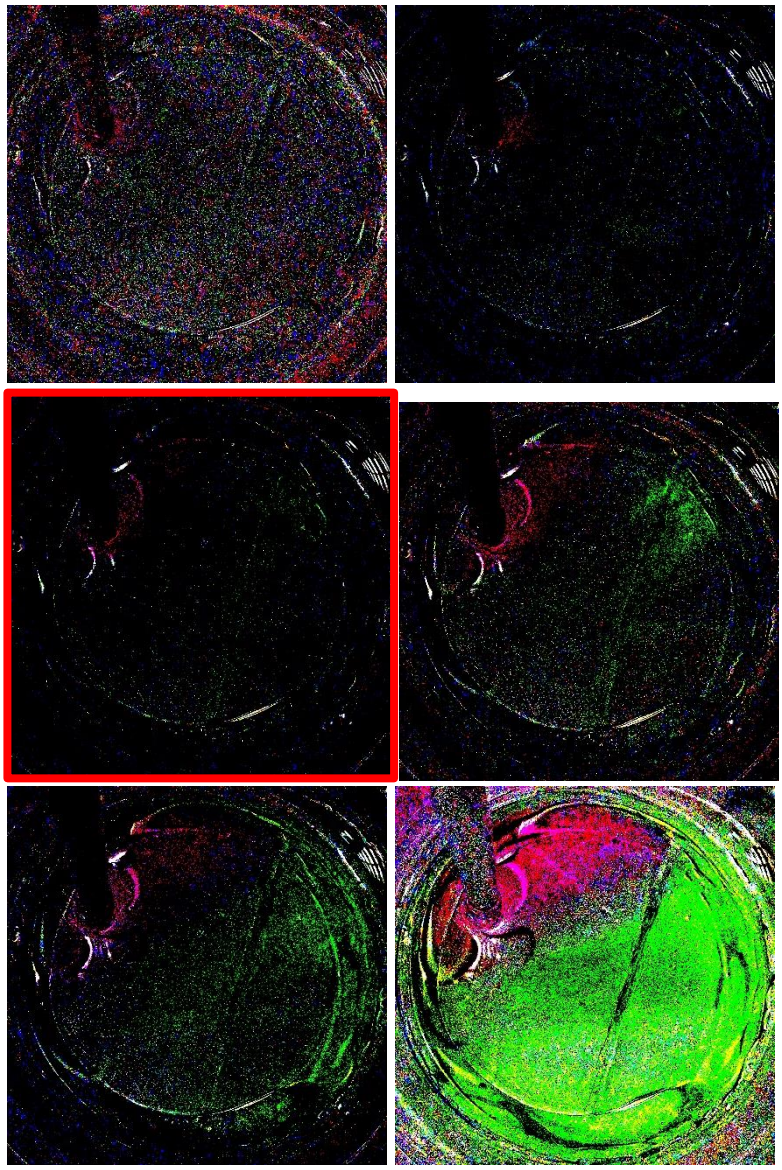

Figure 3. 6 Epoxy with a cut, a local pH change along the cut can be observed, especially for the image marked.

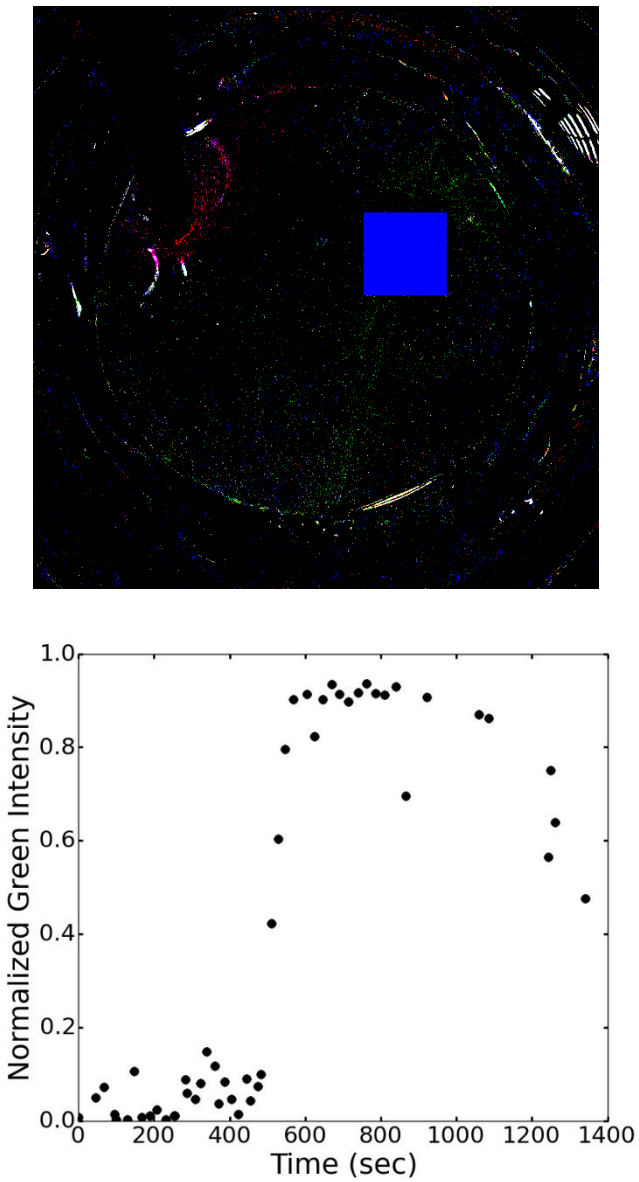

Figure 3. 7 The image of the monitored region, marked by the blue square (left). The normalized green intensity in the region as a function of time (right)[2].

Another challenge tackled was the observation of corrosion before any visual signs occur on painted samples. The panel used was a white painted panel that is manufactured as a test piece for household refrigerators (Figure 3.8). The paint that is used is based on TiO_2 as the main pigment which is highly fluorescent. Therefore,

[2] Using 10^{-7} cm^2/sec [128] as the diffusion coefficient of Hydrogen in aluminum, at 500 seconds, hydrogen diffuses 0.1 mm which is similar to the thickness of our plate (0.6 mm).

the quinine method aside from the quenching issues was not applicable in this case. A small spot that corrodes visibly in Figure 3.8, can be visualized using the local pH change prior to visible confirmation using the phenolphthalein method. This is both due to the increased intensity of the green around the location and the inherent increased clarity of the background subtracted image. To unambiguously show the lower pH around the visibly corroding region, we again monitored two regions of color reduced images throughout time. Figure 3.9 (red curve vs black curve) clearly shows that the region that corrodes at the end of the experiment gives larger green color intensities throughout time compared to a region where no visible corrosion occurs.

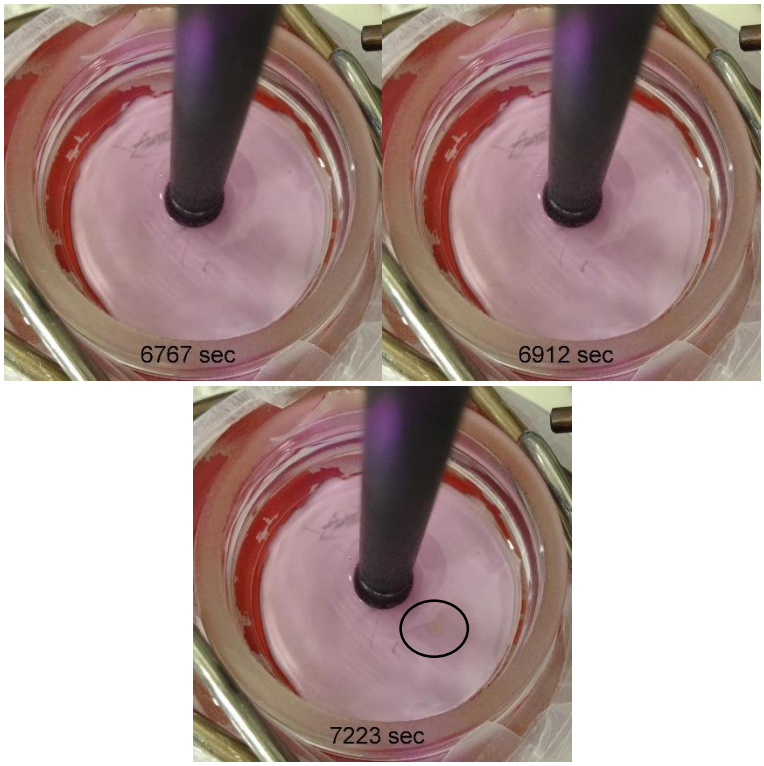

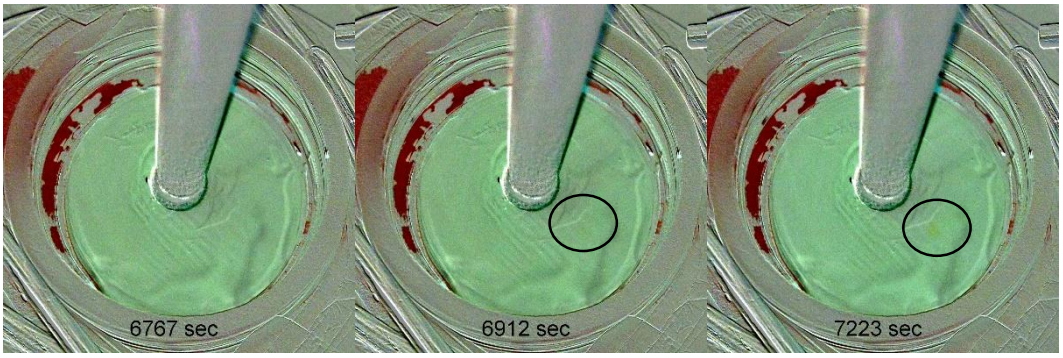

Figure 3. 8 White plate without background subtraction (top), with background subtraction (bottom). The corrosion can be detected earlier using background subtraction.

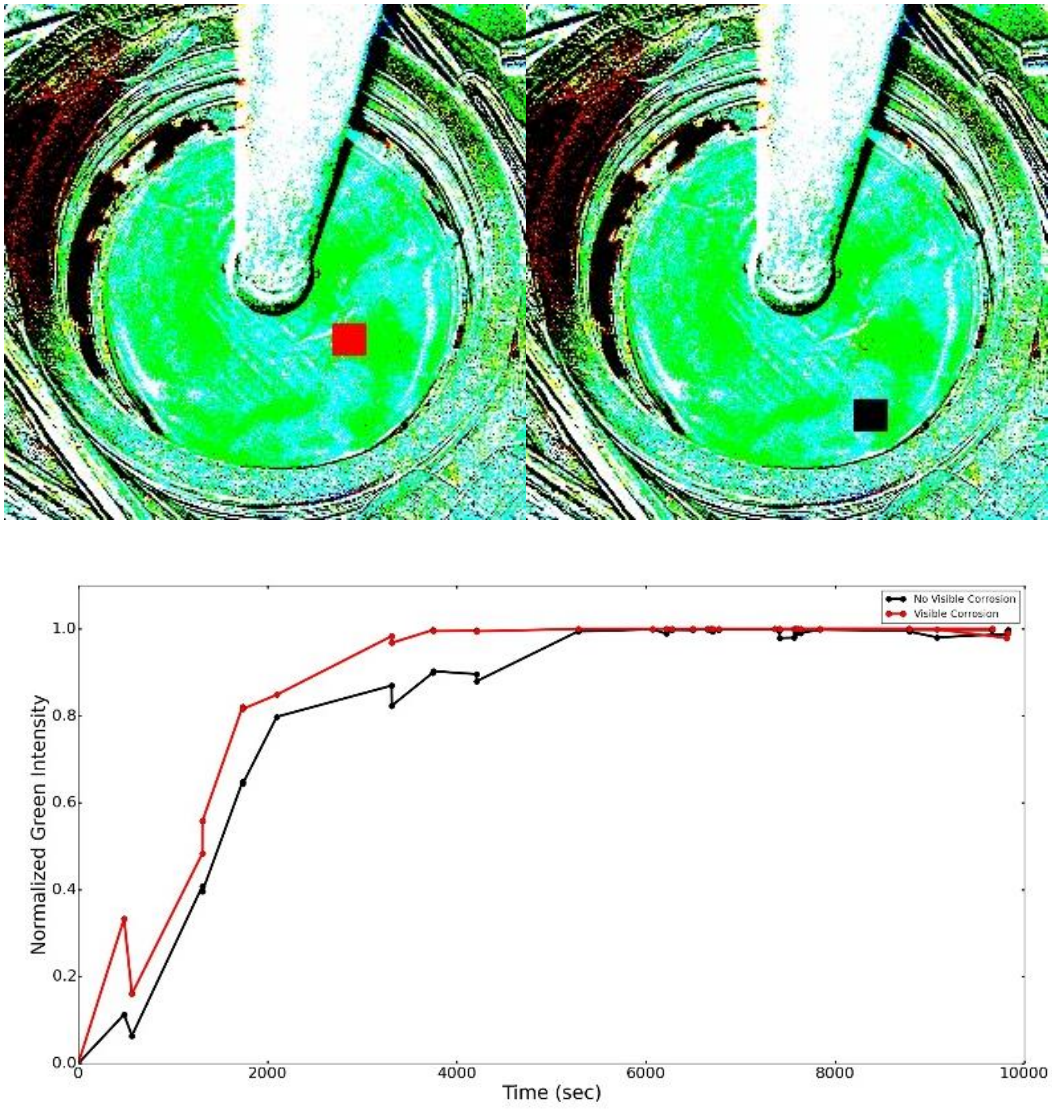

Figure 3. 9 Posterized images of the white plate with phenolphthalein indicator. The red square and the curve shows the visibly corroding region and its green intensity as a

function of time while the black square and the curve shows a region without visible corrosion at the end of the experiment[3].

3.4 Conclusions

A new method for monitoring under-paint corrosion was developed. The developed method utilizes a two compartment Devanathan cell to generate H^+ at the coating defects. These local acidic regions are visualized using simple pH indicators. The basics of the method is illustrated using two different indicators that are suitable for samples with varying degrees of fluorescence.

Moreover, a background subtraction routine was developed to accurately monitor local color changes especially for phenolphthalein indicator where loss of color is hard to follow. Though two examples were discussed in this paper in terms of indicators, it is possible to generalize the method for any indicator with the appropriate excitation to tailor for specific cases.

The method is shown to be successful in visualizing local corrosion behavior of coated metal samples where the currently available methods in the literature either lack the local information or require extremely long scans for local information on the bulk scale.

[3] This graph does not have an initiation period(see Figure 3.7) since we remove that portion for clarity

Chapter 4

4. Electrochemical Investigations of Liquid Crystal Mesophases

(This part is also described in **Can Berk Uzundal**; F. Mert Balcı, Burak Ulgut, Ömer Dağ *"*Lyotropic Liquid Crystalline Mesophase of Sulfuric Acid−Nonionic Surfactant Stabilizes Lead(II) Oxide in Sulfuric Acid Concentrations Relevant to Lead Acid Batteries*", ACS Omega, 2017, 2, 3785-3791.*

"Reproduced with permission from [71] *Copyright 2018")*

4.1 Introduction

Most theories of electrochemistry rely on the understanding of electrolytes based on dilute electrolytes [72]. These theories assume that ions within the electrolyte only interact with a solvent molecule of a single kind and not with each other. Though dilute electrolytes have been relevant in most electrochemical applications and studies, considerable amount of interest and research activity is actively devoted to employing concentrated electrolytes. Concentrated electrolytes not only provide higher conductivities, they also lead to interesting new phenomena as will be shown within this chapter. As an example, activity coefficients in a gel phase and/or a concentrated electrolyte is inherently different compared to the activities predicted for a dilute electrolyte. This chapter will investigate and detail lyotropic liquid crystalline phases which provides a gel electrolyte that is also very highly concentrated.

Given the multitude of domains that are present in the liquid crystal phase, even for a single ion, heterogeneous activity can be expected. In this chapter, a concrete, application-oriented example of this different activity compared to the dilute electrolyte counterpart of the liquid crystal will be discussed and the possible implications of this new found activity for the application will be outlined. Further, recent investigations regarding two distinctly different proton activities in a single phase will be demonstrated.

4.1.1 Lyotropic Liquid Crystalline Mesophases

Hygroscopic species, such as salts and acids can be used as solvent in the assembly of surfactants into lyotropic liquid crystalline (LLC) mesophases.[20,73–75]. Acids, such as H_3PO_4 and H_2SO_4 (SA) that have very low vapor pressure, form stable LLC mesophases in a very broad range of acid concentrations[74,75]. Notice also that SA is a strong acid and forms mesophases upon addition of a small amount of water. The mixture of concentrated SA and surfactant is a liquid that flows when it is spread over a substrate. However, in a short time period, it absorbs enough ambient water to form a rigid and stable LLC mesophase. The typical water up-take of a stable SA-$C_{12}E_{10}$ LLC phase changes with SA concentration and varies from 2.3 to 4.3 water/SA when SA/$C_{12}E_{10}$ ratio increases from 2 to 12[75]. Note also that the mesophase is 2D hexagonal up to around 3.5 SA/$C_{12}E_{10}$ and becomes micelle cubic above this mole ratio. Cubic mesophases are always better conductors than the 2D hexagonal due to 3D connectivity of the ionic species in the mesophase[76]. The SA-$C_{12}E_{10}$ mesophases have excellent proton conductivities that also increase with increasing SA concentration in the media from 2 to 19 mS/cm, while SA/$C_{12}E_{10}$ increases from 2 to 11, respectively[75].

4.1.2 Lead Acid Battery Electrolytes

Acid-surfactant and salt-surfactant mesophases have great potential to be used as gel-electrolytes in various electrochemical devices such as batteries, solar cells, supercapacitors, electrochromic devices, etc[77–82]. The LLC mesophases have already displayed excellent conductivity that is applicable to many electrochemical

systems[73,74,77–82]. In this report, this phase and its applicability to Lead-acid Batteries (LABs) will be investigated.

Recent industry projections predict that LABs will hold its dominant position in the energy storage market in the near future, owing to its current standing applications such as starter batteries in cars and uninterrupted power supplies at various institutions where low cost, reliability and relative safety of the chemistry make it unique[83]. Applications where safety is the most critical component, as is the case in military applications, LABs proven safety record makes them indispensable. For example, LABs are used to buffer the output of the reactor in nuclear submarines. The US. Department of Defense (D.O.D.) has recently awarded a contract worth US$31m to improve the batteries for this application[84]. On the flip side, sulfuric acid industry is thriving owing to the established market in LABs, where sulfuric acid is used as an electrolyte. The total annual consumption is estimated to be US$85b[85]. Therefore, new developments that improve LABs would have substantial industrial and commercial impact, even though the chemistry is mature and well-known.

In the charged state, the positive electrode of a LAB consists of Pb(IV) species and the negative electrode consists of Pb(0) species. At the end of discharge, both electrodes attain Pb(II) species. The main electrochemical reactions are the following (forward reaction indicates discharge)[86]:

$$PbO_2 + 2e^- + SO_4^{2-} + 4H^+ \leftrightharpoons PbSO_4 + 2H_2O \quad (1)$$

$$Pb + SO_4^{2-} \leftrightharpoons PbSO_4 + 2e^- \quad (2)$$

Formation of large $PbSO_4$ crystals as discharge products, which cannot be reduced back to lead during subsequent charge cycles causes battery death. This process, known as sulfation is known as one of the leading causes of lead acid battery failure. To battle sulfation, LABs are designed not to stay in the discharged state for extended periods of time. Though discharge products are always $PbSO_4$, short stays in the discharge state only allow small and reducible/oxidizable $PbSO_4$ crystals to form, which do not compromise the operation of the battery. Extended stays in the discharge state however, cause formation of large non-conducting $PbSO_4$ particles that result in the complete breakdown of the battery[87]. Attempted solutions to combat sulfation in the literature involve the addition of conductive additives to the electrode material or involve composite approaches, where current demands that would otherwise cause deep discharge are drawn from an ultracapacitor instead of the LAB[88,89].

At the end of the discharge cycle, if the Pb(II) species formed were oxides and not sulfates, it would be advantageous both in terms of kinetics of electrode reactions and conductivity. The Pb(II) oxide species is known to be more advantageous both in terms of conductivity and kinetics than the sulfate[86]. Therefore, during industrial production of LABs, the active material production starts from the PbO, and is mixed with enough water to produce tribasic $PbSO_4$ ($PbSO_4$.3PbO), which is more stable in acid solutions compared to PbO. During actual battery operation, the Pb(II) species generated on both positive and negative electrodes are the sulfate since that is the stable form according to the well-known Pourbaix diagram at any

pH below 8 as shown in Figure 4.1[86,90]. In the 6M H_2SO_4 that is typically used, the oxide species is not expected to be stable.

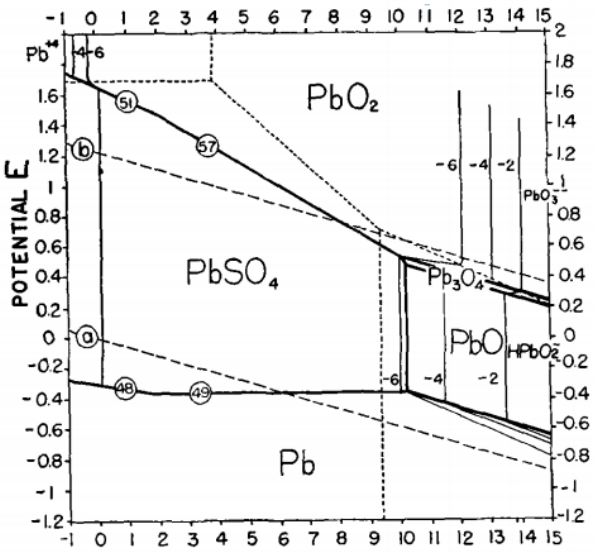

Figure 4. 1. The well-known Pourbaix Diagram for Pb species in sulfuric acid solution. Reprinted by permission from[90].

LABs using gel electrolytes are already commonplace[91,92]. Gels that are employed are made of colloidal silica that is cross linked using acid based dehydration[91,92]. The major advantage of using a gel based electrolyte is mitigating stratification. The gel keeps the electrolyte homogeneous along the height of active material plates, which keeps the entire active material area operational throughout the battery life. A lyotropic liquid crystal (LLC) that has electrochemically active SA would also potentially be a substituent for the colloidal silica gel, thus eliminating the stratification in a similar fashion.

4.2 Experimental Section

Preparation of lyotropic liquid crystalline (LLC) gels. In a general procedure, the LLC gels were prepared by varying SA/$C_{12}E_{10}$ (SA is H_2SO_4 and $C_{12}E_{10}$ is 10-lauryl ether, $C_{12}H_{25}(OCH_2CH_2)_{10}OH$) mole ratio from 2.5 to 9 (2.5 low, 6 intermediate, and 9 high) and keeping the SA/H_2O mole ratio constant at 3.0. For example, the sample with a 9 SA/$C_{12}E_{10}$ mole ratio was prepared as follows; first 9 mmol of SA (1.038 g, 85% SA) was added to 27 mmol of water (0.486 g) and stirred a few seconds by magnetic stirrer. Afterwards, 1 mmol of $C_{12}E_{10}$ (0.626 g) was added to the above clear solution. The resulting mixture was homogenized by using a vortex mixer and then heated in the heat bath at 80^oC for 48 hrs to obtain the clear gel (denoted as 9LC). The other two compositions, 2.5LC and 6LC, were prepared using 0.288 g SA, 0.135 g water, 0.626 g $C_{12}E_{10}$, and 0.692 g SA, 0.314 g water, 0.626 g $C_{12}E_{10}$ and the same procedure. For characterization, the gels were dissolved in water and then coated on glass slides via spin coating at 1000 rpm. For electrochemistry, the gel that is formed was used directly in a vial.

Measurements. The XRD patterns were recorded using a Rigaku Miniflex diffractometer equipped with a high-power Cu Kα source operating at 30 kV/15 mA and a wavelength of 1.5405 Å. The Polarized Optical Microscope (POM) images were obtained in transmittance mode by using a Zeiss Axio Scope.A1 polarizing optical microscope. The SEM images were recorded using a ZEISS EVO-40 SEM operated at 15 kV.

All electrochemical experiments were conducted on a Gamry Interface 5000E potentiostat. Pt CVs were conducted in a 3 electrodes cell with 6 mm diameter Pt working electrode (WE), graphite counter electrode (CE) and Ag/Ag_2SO_4 as a reference electrode (RE).

Polarization resistance experiments were conducted in a 2-electrode geometry, using stainless steel electrodes fitted through a Teflon frit. Each stainless-steel electrode had an area of 0.48 cm^2. Voltage sweeps were chosen to be ± 0.015 V vs. open circuit potential (E_{oc}) with sweep rate of 0.10 mV/s. 10-minute equilibration time followed by 5-hour experiment was done. The value of the self-exchange current was obtained by a linear fit to the data near 0 V (vs. E_{oc}).

Pb-CVs were collected in a 3-electrode cell with a Pb WE strip of 2 by 6 cm, graphite CE and Ag/Ag_2SO_4 as RE. The electrode area of the Pb WE was normalized by epoxy resin such that only a 6 mm diameter circular region of Pb is exposed to the solution/liquid crystal. Moreover, the surface of the Pb WE was conditioned before each sweep experiment at sufficiently negative potentials to reduce all of the electrode surface. Reported Pb in H_2SO_4 CVs were, in all cases at steady state, at least 12 cycles were done and no appreciable change was observed in subsequent cycles.

Ag/Ag_2SO_4 RE was fabricated following a literature report[93]. Briefly, a 1 mm diameter and 3.2 mm height Ag wire was oxidized under constant current of 80 μA for 3 hours in degassed 0.1 M Na_2SO_4. The formation of gray/white Ag_2SO_4 as opposed to the brown oxide was observed. Facile ion transport across the ion-

exchange membrane of RE and liquid crystal was confirmed by impedance measurements (measured Z = 346.5 Ω). The stability of the fabricated electrode was confirmed by Pt in H_2SO_4 CV's over a 24-hour period. The potential calibration was done by measuring and monitoring the open circuit potential of a 2 electrode system where the working side is a Ag/AgCl RE, while the counter side is the Ag/Ag_2SO_4 RE (E_{oc} = -0.407 V).

Chronoamperometry experiments were done at various potentials for 1, 5 and 10 hours for both 9LC and 5M H_2SO_4 solution after conditioning at the appropriate negative potential and linear sweep (at 1 mV/s) to the potential of interest. A 3-electrode setup consisting of Pb WE, graphite CE and the previously prepared Ag/Ag_2SO_4 RE was used. The lead strips were washed gently with de-ionized water and the SEM images were taken.

4.3 Results and Discussion

4.3.1. Sulfuric Acid Containing Liquid Crystals for Lead Acid Battery Applications.

Three different compositions were prepared by mixing and homogenizing quantitative amounts of $C_{12}E_{10}$, SA, and water (1:2.5:7.5, 1:6:18, and 1:9:27 mole ratios, respectively) to obtain the liquid crystalline gel phases. The 2.5 $SA/C_{12}E_{10}$ sample (denoted 2.5LC) displays a focal conic fan texture, characteristic for the 2D hexagonal columnar phase, Figure 4.2 (a). The other two samples of 6 and 9 $SA/C_{12}E_{10}$ mole ratios (denoted as 6LC and 9LC) are dark between the crossed polarizers. All three samples diffract at small angles with slight shift to lower angles

with increasing SA amount in the samples, see Figure 4.2 (b). Even though there is a single line in the diffraction patterns, the mesophase is micellar cubic in the 6LC and 9LC[75]. Notice also that surfactant molecules are not stable in concentrated SA solutions and slowly undergo dehydration to form carbon nanoparticles. A mixture of concentrated SA and surfactant is a transparent colorless liquid, but slowly turns into dark brown over time. The carbonization process is halted in the presence of a small and stoichiometric amount of water in the LLC media. For instance, if a solution of concentrated SA and $C_{12}E_{10}$ (undergoes slow carbonization) is exposed to ambient laboratory condition, the mixture slowly adsorbs enough water to transform a stable gel phase, where the $C_{12}E_{10}$ molecules are stable.

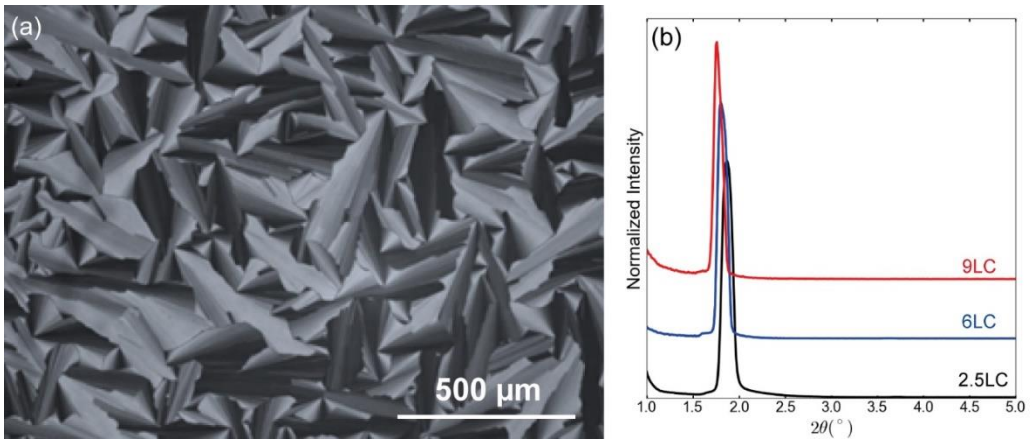

Figure 4. 2 POM image of 2.5LC (a) and small angle XRD patterns 9LC, 6LC, and 2.5LC, top to bottom (b). XRD patterns are offset for clarity.

Two separate studies have been performed in order to investigate the proton activity or apparent pH of the LC systems. Both tests are picked from the electrochemistry literature on well-established experiments using SA solutions as electrolytes. The two experiments picked, are the well-known polycrystalline Pt in SA CV experiment and standard polarization resistance experiments on stainless steels. The

CV of a 5M aqueous SA solution, 6LC, and 9LC using Pt as the WE are shown in Figure 4.3 (a) (2.5LC data not shown for clarity). CVs clearly show that both 6LC and 9LC have electrochemically active SA and display characteristic peaks of Pt in SA systems[94,95].This is a clear indication that the SA inside the LLC mesophases is electrochemically active and that the cyclic voltammetric features of hydrogen adsorption/desorption, and the oxide formation/reduction are feasible inside the LLC mesophases. The peak onsets shift to more positive potentials on the hydrogen desorption/adsorption in case of LLC phases compared to 5M SA aqueous solution. This shift, roughly 40 mV would indicate that the activities of H^+ are slightly higher in the LLC mesophases compared to the 5M aqueous SA solution. Corrosion rate measurements of stainless steel in LLC phases indicate a similar level of activity. In the literature[96], it is well-established that the rate of corrosion increases with increasing concentration until 6M and decreases going from 6M SA to concentrated SA. As shown in Figure 4.3 (b), the corrosion rates for 6LC and 9LC not only show a rate of corrosion that is commensurate with the above conclusion, but also there is a reinforcing trend of decreasing corrosion rate with increasing acid amount. Based on the CV experiments of Pt and the corrosion rates of stainless steel, the sulfuric acid inside the LLC mesophases are electrochemically active, and that the activities of the SA inside the phases correspond to activities of 5-10M SA in aqueous solutions.

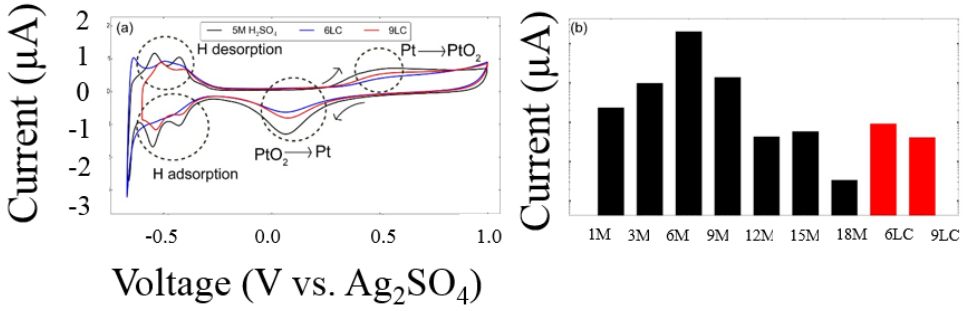

Figure 4. 3. The Pt electrode experiments (a) and the corrosion rate experiments (b) to confirm the electrochemical activity and to establish an analogy to aqueous solutions of sulfuric acid.

The electrochemistry of Pb in SA is industrially important in LABs. Therefore, we focus on investigating the LLC mesophases using Pb as the WE. The SA-$C_{12}E_{10}$ LLC mesophases show not only high conductivity but also the relevant electrochemical reactions. This highlights the applicability of LLC mesophases as an alternative electrolyte in LABs. Moreover, any change in the properties of the relevant electrode reactions may have impact on preparation and preservation of the electrodes for the traditional LABs. As a result, we mainly focused on the Pb oxidation to PbO/$PbSO_4$ and their subsequent reduction to Pb metal, which is the negative electrode half-reaction in LABs.

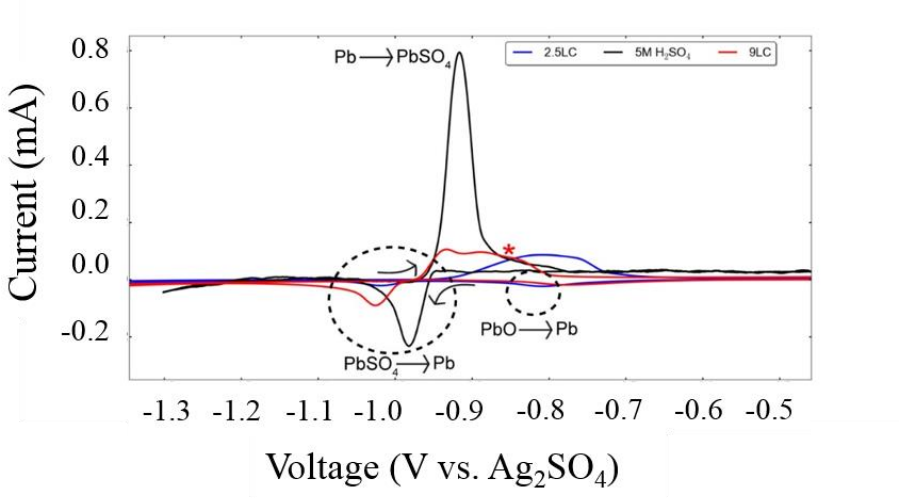

Figure 4. 4 The Cyclic voltammetry profiles for Pb electrodes in an aqueous solution (black) compared to two LLC phases (2.5LC in blue and 9LC in red)

A typical Pb CV of 5M SA is shown in Figure 4.4. It displays an oxidation peak due to Pb to $PbSO_4$ oxidation on the oxidation side and a much smaller reduction peak, attributed to the reduction of $PbSO_4$ back to Pb, as also shown in the literature[97–99]. The weak reduction peak is attributed to formation of large non-conducting $PbSO_4$ crystallites that cannot be reduced[86]. Corresponding CVs in the 2.5LC and 9LC mesophases display distinctively different voltammograms. Notice that the single oxidation peak in the 5M SA becomes two in the SA-$C_{12}E_{10}$ samples. We focused our attention on the 9LC due to its higher SA activity (as confirmed by polarization resistance and Pt electrode experiments). Looking at the data more carefully, not only the oxidation peak has a shoulder, but also a new reduction peak, distinct from the reduction of $PbSO_4$ is present. This shows the unique effect of SA-$C_{12}E_{10}$ mesophases on the Pb redox products. There is clearly a new species that gets reduced at a distinctly more positive potential than the sulfate. Furthermore, the ratio of $PbSO_4$ reduction peak current to the Pb oxidation peak current is also markedly larger in the LLC system at 1 mV/s compared to 5M

SA solution, suggesting a more reversible reaction, as shown in Table 1. The LLC system leads to smaller $PbSO_4$ products that are more readily reducible than their counterparts formed in the aqueous solution.

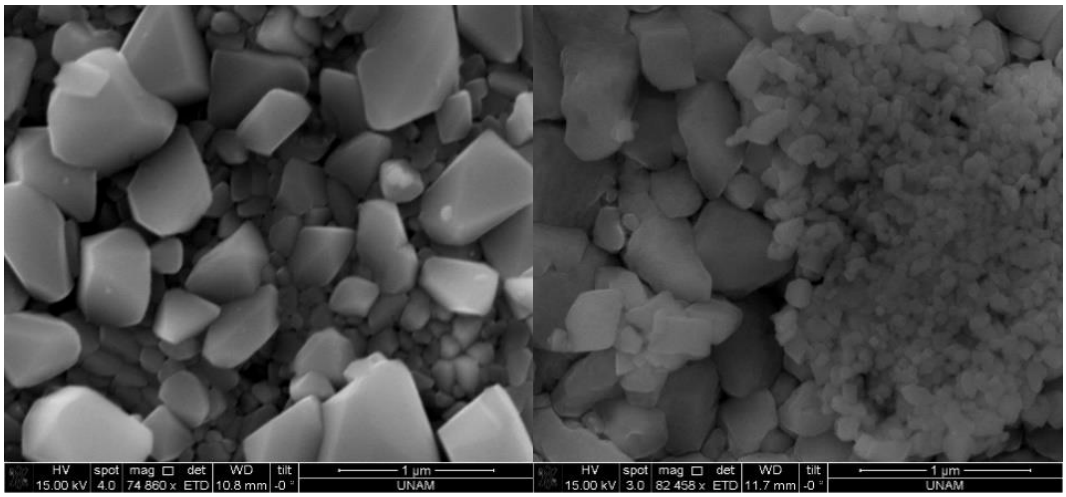

Figure 4. 5 SEM images of a lead strip after 10 hours of chronoamperometry at -0.91V (vs. Ag2SO4) (left) in 5M H2SO4 and in 9LC (right).

Electrolytes	Oxidation peak current (µA)	Reduction peak current (µA)	Ratio (%)
9LC	107.8	101.6	**94.2**
6LC	225.2	46.08	**20.5**
5M H_2SO_4	979.6	270.5	**27.6**

Table 1 PbSO4 oxidation and reduction peak currents at 1 mV/s sweep rate

Shoulder peaks can only be resolved at low sweep rates, such as 1 mV/s, indicating the slow kinetics of the process. To identify the new species formed in the LLC system, we conducted chronoamperometry experiments at various potentials to grow films over the Pb electrode and characterized using XRD and SEM. First inspection of Pb electrodes after this process shows a distinct difference between

electrodes obtained from 5M SA and 9LC in terms of color of the Pb surface. The Pb electrode has a yellow/brown color in the SA-$C_{12}E_{10}$ compared to gray/white in the 5M SA solution (see Figure 4.7 for pictures). We further analyzed electrodes by collecting their XRD patterns. Figure 4.6 displays two sets of XRD patterns of the Pb electrodes after conditioning and chronoamperometry experiments. The XRD patterns of both electrodes, after conditioning using 5M SA and 9LC only displayed Pb(0) diffraction lines. However, the electrode prepared from the chronoamperometry experiment distinctively displayed lines originating from the PbO and $PbSO_4$ in the 9LC system (I) compared to predominantly $PbSO_4$ in the 5M SA solution (II), see Figure 6 (b). The PbO lines are relatively broad due to formation of PbO nanoparticles, preferentially grown along the [200] axis. The average particle size of the PbO particles was determined to be 14 nm, obtained from the Scherer equation. Both forms of PbO with similar particle sizes (α-PbO and β-PbO with a higher concentration of β-PbO) are observed in the pattern obtained from the 9LC electrode. The SEM images of these two electrodes, prepared using 9LC and 5M SA, display quite different surface morphology. Crystalline surface species, over the surface of electrode used in 9LC, are more uniform and much smaller than that of the electrode used in 5M SA and consistent with the electrochemical and XRD results, see Figure 4.5. One explanation for this observed result is that PbO forming on the surface of the Pb electrode is stable when it is in contact with the LLC phase opposed to the high instability in SA solution.

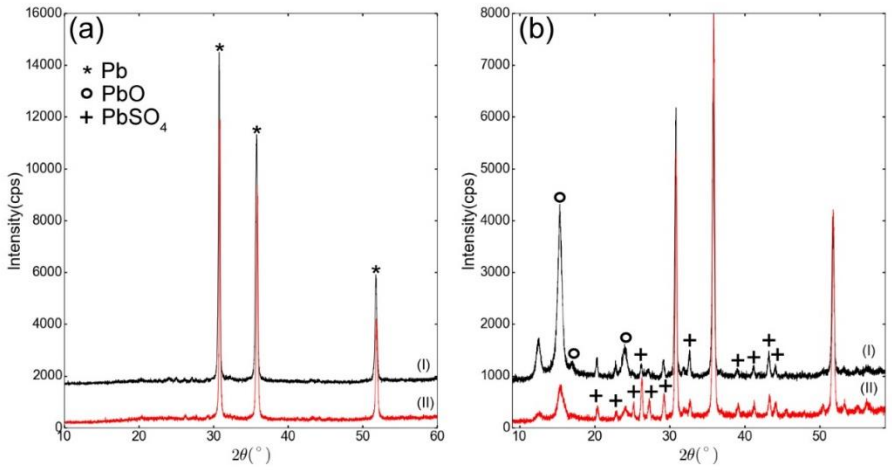

Figure 4. 6 The XRD patterns for as conditioned Pb electrodes (a) and after oxidation (b). The black curves (I) show the results in LC and the red curves (II) show the aqueous solution. XRD patterns are offset for clarity.

To test this hypothesis, the resulting $PbO/PbSO_4$ grown on Pb electrode using the 9LC was submerged in 5M SA solution. The loss of the initial yellow/brown color hints at the instability of the formed oxide in the solution phase. Linear sweep voltammogram (LSV) of the $PbO/PbSO_4$ after submerging in 5M SA solution (for 24 hours), showing a single reduction peak, which is attributed to the lead sulfate reduction back to lead, is shown in Figure 4.7 (b). Similarly, LSV of a pristine $PbO/PbSO_4$ shows a shoulder peak (Figure 4.7 (a)), thus suggesting the presence of another species on the coating, which is not stable in the aqueous SA solution. Further cycling the potential for this lead strip did not yield the same shoulder peak as shown in Figure 4.7 (c). These results clearly show that the oxide species, as expected, are not stable in the solution phase, while they do form in LLC mesophases and are stable.

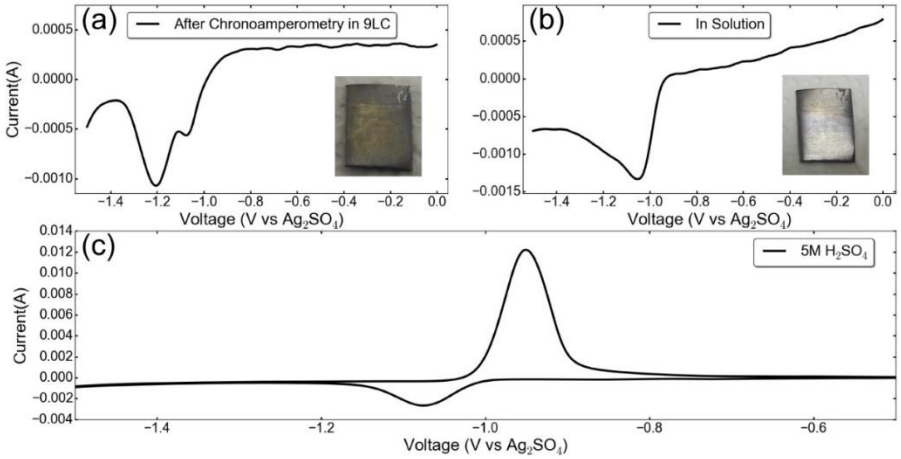

Figure 4. 7 PbO-PbSO4 film is developed on top of a lead strip in 9LC by 10 hours CA, then in aq. H2SO4, LSV is done (a). Another similar film is kept in aq. H2SO4 for 24 hours then LSV is done (b). The CV after submerging in aq. H2SO4 for 24 hours (c).

The reduction peak that is attributed to the reduction of PbO was also observed in aqueous systems, only when the CV is performed to very oxidizing potentials that also lead to PbO_2. This behavior was also shown in the literature[98,99]. Under these conditions, the two reduction peaks are present and the peak at the more positive potentials is attributed to the reduction of PbO. In the current work, the reduction peak attributed to PbO is visible even when potentials are never swept to as positive potentials.

4.3.2 Ion Activities in LLC Phases

The above detailed picture clearly suggests that through kinetic barriers to the conversion of the oxide to the thermodynamically favored sulfate, preferential stabilization of the oxide phase can be sustained in these LC phases. A clear picture, however, in terms of the species responsible for such distinct activity is not available within our expectations as guided by the dilute electrolyte theories.

Focusing on the easily followed ions, namely the proton in this acidic liquid crystal, by varying the relative concentrations of acid and surfactant, it is possible to obtain different gel phases as mentioned in the previous chapter. By following electrochemical signatures of these different gel phases and comparing them to the various concentrations of their aqueous counterparts ranging from fully concentrated to pure water, it is possible to obtain a relative scale on the proton activity and hence the pH of the system. Further, by incorporating another redox couple that is pH sensitive to the gel phase and by again comparing the electrochemical signatures obtained to the electrochemical activity of their aqueous counter parts it is possible to have at least two independent parameters on the proton activity observed. Similar studies are not limited to only the sulfuric acid containing liquid crystals reported here, as will be shown, phosphoric acid containing systems are amenable to the same treatment as well.

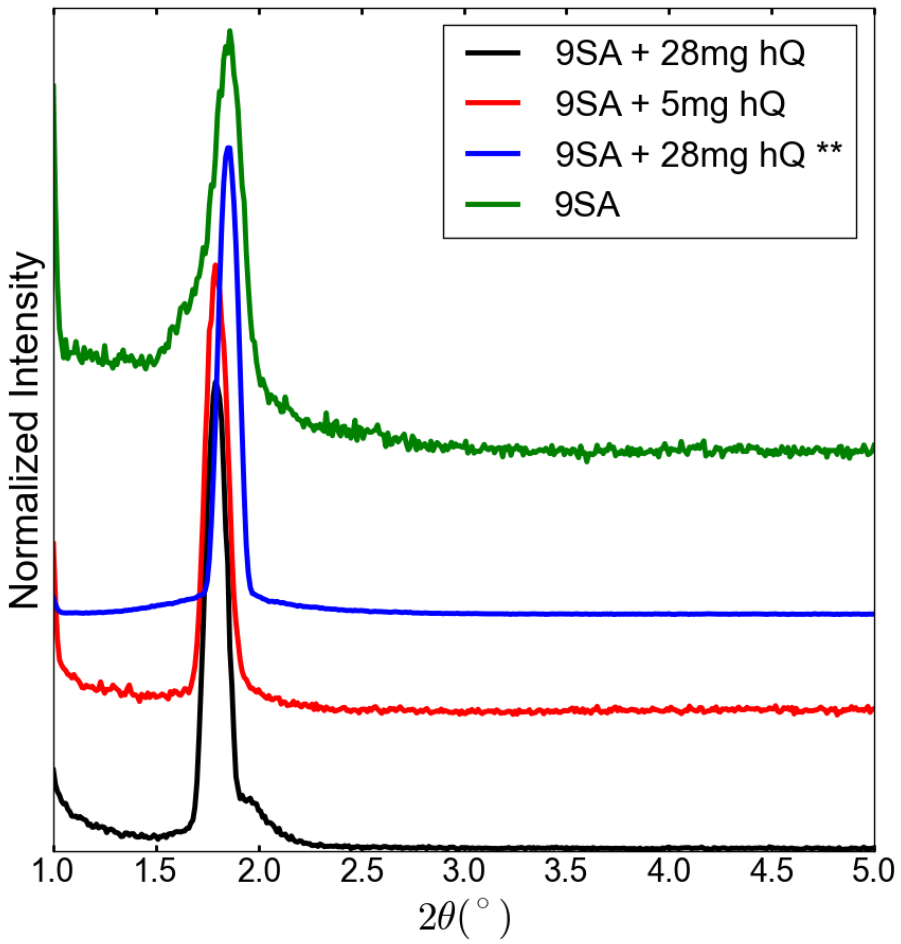

Figure 4. 8 Low angle XRD measurements on Liquid Crystals containing hydroquinone (hQ) and the pristine hQ (green).

For the sulfuric acid containing liquid crystals, a small amount of hydroquinone (5 mg) was incorporated into the gel phase without significantly distorting the gel as shown by the small angle XRD (Figure 4.8). Similar solutions containing small amounts of hydroquinone was prepared inside aqueous sulfuric acid solutions ranging from 3M to fully concentrated (~18.4M). For each of these solutions and for three liquid crystals of different sulfuric acid to surfactant ratios (9:1, 6:1, 2.5:1) a cyclic voltammogram using glassy carbon as working electrode and Ag/Ag_2SO_4

as reference electrode was obtained. The obtained voltammograms are expected to be fully reversible and should show the characteristic Nernstian peak shape with a small peak separation (Figure 4.9). At low water contents, however, a splitting in the peak shape is observed for both the gel phases and the aqueous solutions. A quick literature survey on the electrochemistry of quinones show that this splitting behavior is consistent with the stabilization of the intermediate species of the hydroquinone oxidation through sparse hydrogen bonding[100–104]. Especially in aprotic solvents upon the addition of small amounts of water, such peak splitting was shown to occur [101,102]. Nernst equation, as described in the basics of electrochemistry section of the introduction, suggests that the activities/concentrations of the species that appear in the equilibrium expression shifts the thermodynamics of the system. In cyclic voltammetry, such shifts in thermodynamic potentials can be quantified as shifts in the peak potentials observed. For a reversible couple, the peak potential average of the oxidation and the reduction waves, called $E_{1/2}$ can be related to the electrochemical potential and can directly quantify this shift in redox potentials [22]. Using this and obtaining $E_{1/2}$ for the solutions and the three liquid crystals, the following trends with increasing acid concentrations can be quantified.

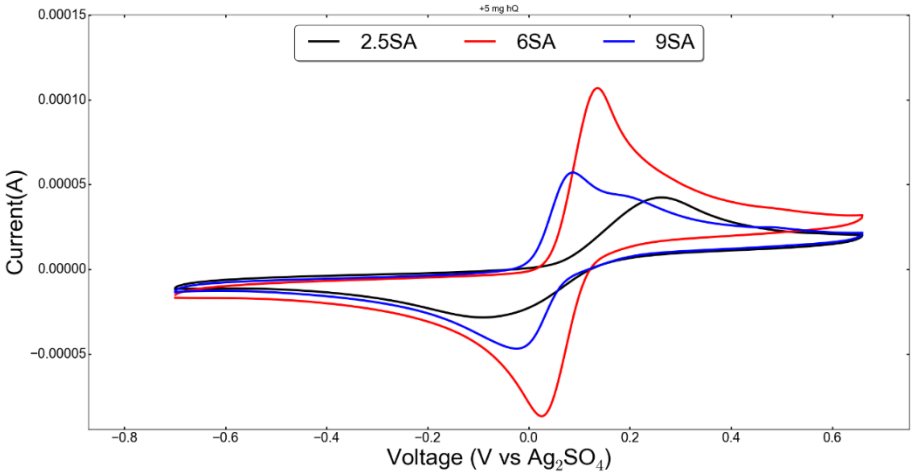

Figure 4. 9 Cyclic voltammograms of Liquid crystals containing different sulfuric acid ratios (9,6 and 2.5). CV was taken at 50 mV/s, with Glassy Carbon working electrode.

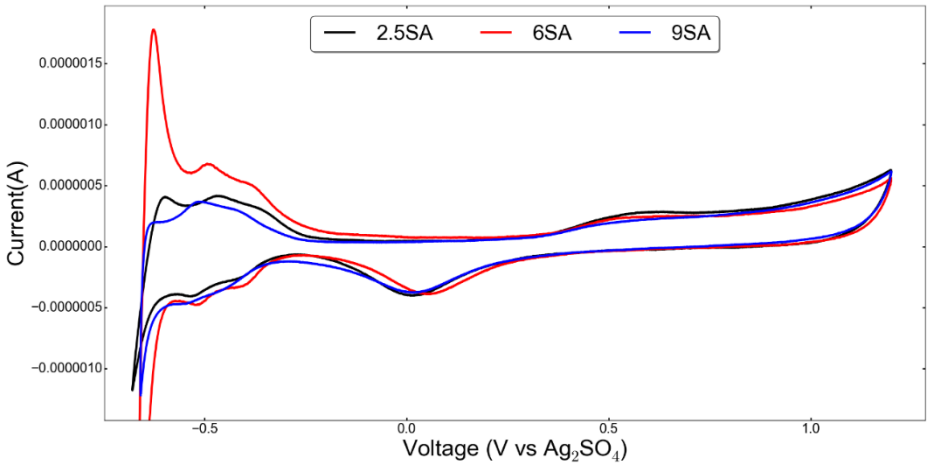

Figure 4. 10 Pt in acid cyclic voltammograms of Liquid crystals containing different sulfuric acid ratios (9,6 and 2.5). CV was taken at 10 V/s, with Pt working electrode.

A similar treatment to the hydrogen desorption-adsorption region observed for the Pt in acid cyclic voltammograms shown in the previous section (and in Figure 4.10) can be done and $E_{1/2}$ for those liquid crystals and the aqueous solutions can be compared to quantify the trends with respect to acid concentrations (Figure 4.11).

Strikingly, the trends obtained from the hydroquinone and Pt in acid cyclic voltammograms (Figure 4.10) are opposite to each other (compare the order of red-blue and green in Figure 4.11 and 4.12). This brings the proton activity observed for the surface species (i.e. adsorption on to polycrystalline Pt) and solution species (i.e. redox reactions of hydroquinone) in question. Apparently the activity order for these two species are reversed. Similar reversal of trends for the proton activity towards Pt surface and hydroquinone can be observed for phosphoric acid containing liquid crystals as well. The activity, however, for the phosphoric acid case, does not fall within the scale provided by the aqueous counterparts, presumably because of the overall slower kinetics of the processes in the phosphoric acid as evidenced by the peak separations and the peak shapes observed by the cyclic voltammograms. Further studies to pinpoint the domains responsible for this activity is ongoing through ^{1}H and ^{31}P NMR studies, as well as further electrochemical studies with different redox couples are being conducted.

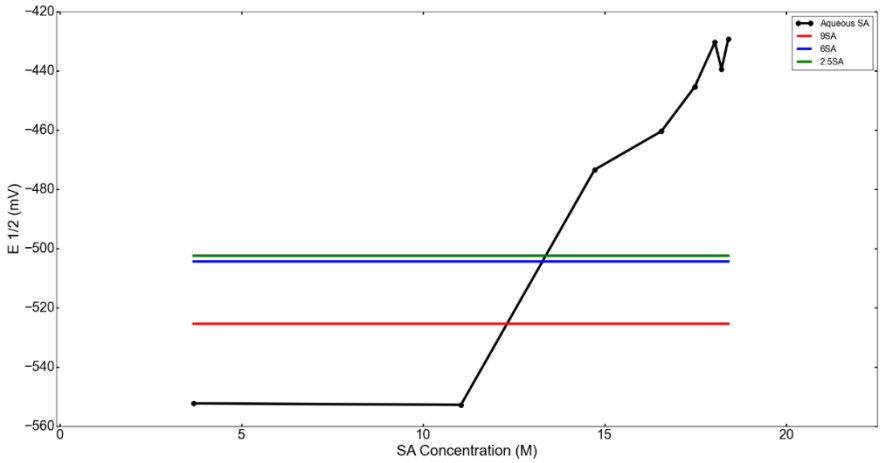

Figure 4. 11 $E_{1/2}$ for hydrogen adsorption on Pt, obtained for aqueous solutions of various concentrations (black) compared to different liquid crystals.

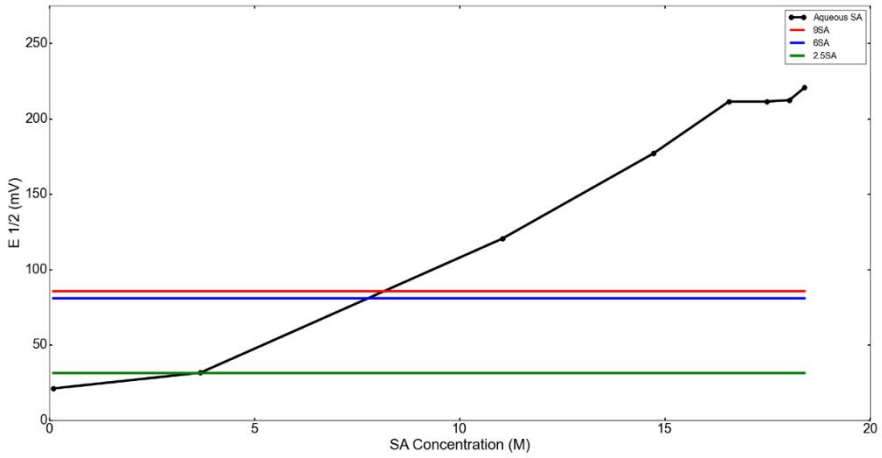

Figure 4. 12 $E_{1/2}$ for hydroquinone redox, obtained for aqueous solutions of various concentrations (black) compared to different liquid crystals.

4.4 Conclusions

SA forms LLC mesophases with a non-ionic surfactant (such as $C_{12}E_{10}$) and displays electrochemical activity similar to aqueous SA. The SA-$C_{12}E_{10}$ mesophases, however, produce stable PbO in addition to $PbSO_4$ during oxidation or discharge of LABs, which can be utilized industrially. It is likely that the PbO always forms during oxidation of lead in the discharge of LABs. However, PbO converts into insoluble, non-conducting $PbSO_4$ in ordinary LABs, due to its high instability in aqueous SA solution. The formation and high stability of PbO in the case of LLC as the electrolyte would be a vital improvement for the development of gel-electrolyte LABs over traditional LABs.

One possible explanation for this effect is that the contact between the electrode and electrolyte is hindered by the surfactant molecules. This stabilizes the PbO formed over the electrode surface. Otherwise a direct contact of SA solution to the electrode surface is detrimental for the PbO particles and decompose into PbSO4.

The mesophases are electrochemically active but chemically protective for the formation and stability of PbO. The change in order of the proton activity that results in this changed order of activity is being investigated by electrochemical pH measurements and NMR studies.

Chapter 5

5. Ultrafast Spectro-Electrochemistry of Conjugated Polymer Films

5.1 Introduction

As mentioned in the introduction chapter, electrochemical methods can demonstrate the underlying mechanisms involved in a given electron transfer process. The method of choice in these investigations is usually cyclic voltammetry where a triangular waveform is applied to the working electrode. The details of the method is explained briefly in the basics of electrochemistry section of the introduction and in more detail elsewhere[22,24]. Briefly, depending on the rate at which the linear waveform is swept (i.e. sweep rate), the timescale of the

experiment can be tuned and access to various domains of competing processes can be achieved. For conventional potentiostats, the sweep rate ranges from mV/min to 10 V/s thus allowing almost 6 orders of magnitude in terms of the accessible time domain for a single method.

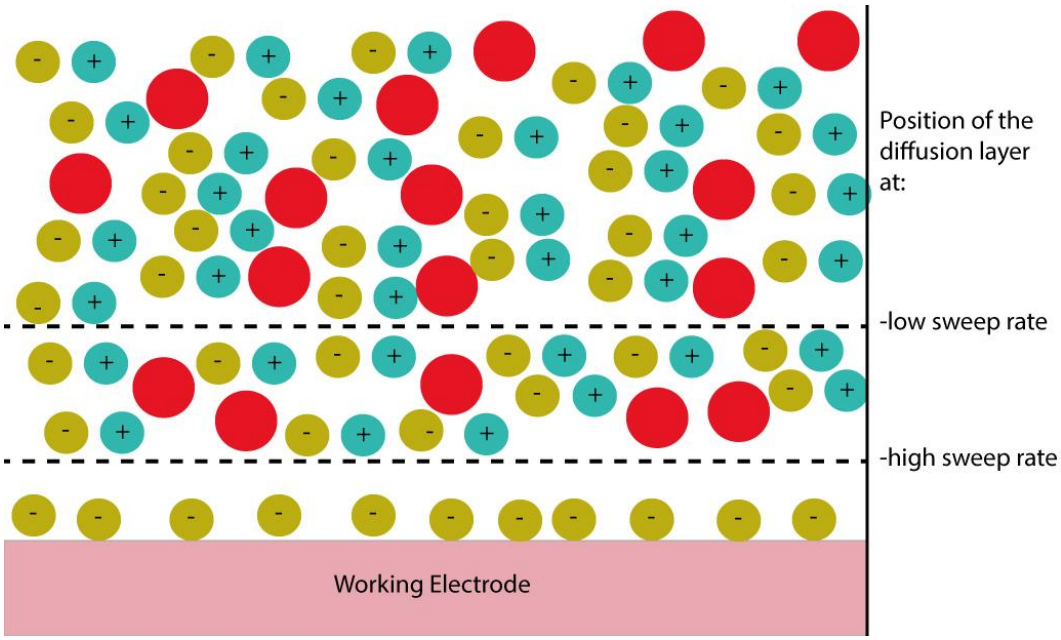

Figure 5. 1 The depiction of the position of diffusion layer with respect to sweep rate. Red circles denote electroactive species while the rest are electrolyte ions

The timescale of cyclic voltammetry derives from the construct of a diffusion layer, where the measured current can only be due to the electroactive species that can undergo redox reactions at the electrode surface by diffusing the length of the diffusion layer before the scan direction is reversed. This constitutes a region in the electrolyte where the concentration of these electroactive species are different than the corresponding concentrations in the bulk, (as explained in more detail in the Basics of electrochemistry section) this region is called the diffusion layer. Though their names are similar, the diffusion layer and the diffuse double layer should not

be confused where the latter is the result of a non-faradaic process while the former is the result of a faradaic one. The length of the diffusion layer, thus, depends on the sweep rate where at high sweep rates a small diffusion layer is present while at a low sweep rate the diffusion layer can extend further into the electrolyte as shown in Figure 5.1. At the large diffusion layer limit, a couple of factors limit the length of the diffusion layer, one is the length of the container the electrolyte is stored in while more importantly, contribution from convection during such a long experiment would limit the length of the diffusion layer, as well as thermal fluctuations due to the current passing. Further, no real benefit is gained from such a long diffusion layer where the mass transport properties of the species involved can already be extracted at more manageable timescales. At the small diffusion layer limit, however, it is possible to investigate heterogeneous electron transfer reactions without the limits imposed by the diffusion of the electroactive species where inherently diffusion is much slower compared to the electron transfer reactions[105]. The setup, however, is complicated by instrumental limitations due to the extremely high sweep rates (~$10^{5\text{-}6}$ V/s) required. The technique is called Ultrafast Cyclic Voltammetry and has been utilized in investigation of electron transfer in redox active dendritic structures, self-assembled monolayers and in accurate determination of electron transfer rate of fast heterogeneous electron transfer reactions [105–111]. At these high sweep rates/short timescales, factors that are neglected in regular cyclic voltammetry investigations become extremely important and need to be either eliminated or corrected for [105]. First, the OpAmps chosen for the potentiostat need to be able to follow the fast signal waveform

applied while still maintaining reasonable gain at a low input bias. Slew rate[4] of an OpAmp in this case becomes an important metric in selecting the appropriate OpAmp for high sweep rates. For an ideal OpAmp slew rate is infinite (i.e. any change in the applied voltage is reflected at the same time to the output of the OpAmp) while for common OpAmps such as LM741 the slew rate is 0.7 V/μs and for LF356 (which is used in our in house Ultrafast Potentiostat) it is 12 V/μs. Do note that slew rate not only depends on time but also on the voltage amplitude. To put these numbers in perspective, let's consider an OpAmp to which a sinewave of the following form is input;

$$V(t) = Asin(2\pi ft)$$

For faithful reflection of this input, the slew rate of the OpAmp should at least match the highest rate of change in the input (i.e. highest slope in the voltage applied). The derivative of the above waveform evaluated at the zero crossing (t = 0) gives the highest slope for this sinewave as the following;

$$\frac{\partial V(t)}{\partial t} = 2\pi fAcos(2\pi ft)$$

$$\frac{\partial V(t)}{\partial t}\Big|_{t=0} = 2\pi fA$$

For a sine wave of 1 $V_{p\text{-}p}$ and a frequency of 1 MHz the highest slope is then 3.14 V/μs. For the LM741, the slew rate is slower compared to this value. As such if this OpAmp was used to for example follow this voltage in the Voltage Follower

[4] Slew rate of an OpAmp is the rate at which the output responds to a sudden/step change in the input.

Geometry, the output would not be a true representation of the input. In the case of LF356, however, faithful reproduction of the applied sine wave would be achieved and the voltage follower would work as expected.

A similar and typically stricter constraint on the system is imposed by the time constant of the electrochemical cell. The area scales with the square of the electrode size, "r", while the resistance of the electrode decreases as 1/r. Therefore overall, the time constant, for most cases, scale linearly with electrode size[22] Even if the instrument can match the applied waveform perfectly, if the time constant of the electrochemical cell is large, the electrode will not be at the desired potential in the given timescale as explained in the Chapter 1 of this thesis for Cottrell equation [22]. Therefore, to achieve high sweep rates, electrodes of small radius (~μm) (to reduce the electrode capacitance), are routinely utilized in well supported electrolyte media (to reduce the electrolyte resistance) [112–114]. Especially without corrections to the electrolyte resistance this time constant quickly becomes a limit on the sweep rates achievable for a given electrochemical setup.

In addition to increasing the time constant, the resistance in the cell creates errors in the measured electrochemical potential. In conventional cyclic voltammetry, the potential lost to bulk resistance of the electrolyte is ignored since at these sweep rates the current passing (~μA) through the electrolyte resistance (~Ω) yields a negligible loss of potential (~μV) where usually instruments report voltages with a lower sensitivity (±1 mV) than the potential lost. However, at high sweep rates due to the high currents involved as predicted by Randles' Sevcik equation (see Chapter 1), this loss becomes non-negligible and can even over power the applied

voltage[109]. Therefore, to achieve high sweep rates this Ohmic loss, coined the iR drop, needs to be corrected.

Post-run iR correction can be achieved by adding the iR drop to each voltage point measured during the experiment as the following [22];

$$V_{corrected} = V_{measured} + i_{measured}R_{solution}$$

Although post-run iR correction is utilized in obtaining potentials without the interference of the solution resistance to extract kinetic information[115,116], it is not a viable option at high sweep rates. Numerically adding the lost potential does not change the fact that the working electrode does not reach the potential desired during the experiment. For instance, a solution resistance of 10Ω while passing 100 mA current causes an ohmic drop of 1V. Therefore, instead of enabling redox reactions at the electrode-electrolyte interface, most of the applied potential will be spent on the bulk electrolyte solution. If the iR drop is corrected after the experiment, this correction will not change where the applied potential is effective in the electrochemical cell during the experiment. Approaches that can correct for the iR drop as the experiment is conducted is required. One such method is called current interrupt iR compensation [117,118]. Consider the simplified Randles' Cell as the equivalent circuit representation of the electrochemical cell explained in the Basics of Electrochemistry section

.

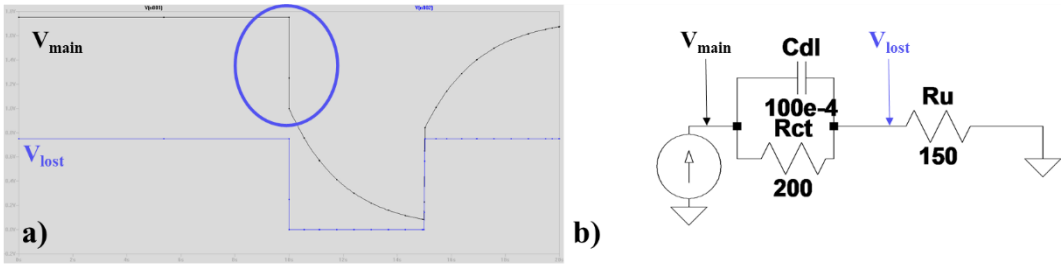

Figure 5. 2 LTspice simulation demonstrating the basics of current interrupt technique a) the voltage response of the main node and the voltage over the resistor Ru b) The simulated simplified Randle's Cell.

Under a constant voltage, a current of certain magnitude passes through the cell. If for an instance the applied voltage is lifted and the voltage of the cell is very quickly measured, the potential measured will be the voltage measured over the capacitor in the equivalent circuit. A better way of implementing this is through galvanostatic control where at a certain time the current applied to the electrochemical cell is forced to 0 (by turning off the cell-switch, thus the name current interrupt), while monitoring the voltage of the electrochemical cell. The method and the obtained waveform as a result of current interrupt is shown in Figure 5.2. The voltage measured by a potentiostat can be thought as the main node potential (V_{main}) while the voltage lost to ohmic drop is shown as V_{lost}. When the current source is shutdown at a certain time, the main node voltage suddenly drops to a certain value (as marked by a circle in Figure 5.2-a). Verifying the magnitude of this drop by comparing it to V_{lost}, we can confirm that this drop in potential is indeed the potential lost to the resistance of the electrolyte solution. Therefore, the difference between the applied potential and the measured voltage after the current interrupt yields the iR drop. By implementing an analog or a digital control loop this value

can be corrected during the experiment by applying potentials that are larger than the desired voltage (i.e. $V_{applied} = V_{intended} + iR$). Current interrupt works best for DC experiments where potentials are either not changed or slowly changed, therefore it is not applicable to high sweep rate experiments[118]. Instead on-line iR compensation through a positive feedback loop is utilized to achieve high sweep rates in cyclic voltammetry [105]. An OpAmp that has a variable gain through a user controlled resistor is employed such that the voltage lost in the iR drop is constantly added to the function generator input. The specific circuitry of this type of a potentiostat, as well as a regular potentiostat will be discussed in the next section of this chapter. The potential lost on the bulk electrolyte solution reflects as a washing out of the expected cyclic voltammogram. Especially at the edges of the voltammograms, as sweep rate increases an oval shape instead of the square like rises is seen. When the solution resistance is compensated, however, this rise is much sharper and recovers its square like shape as seen in Figure 5.3.

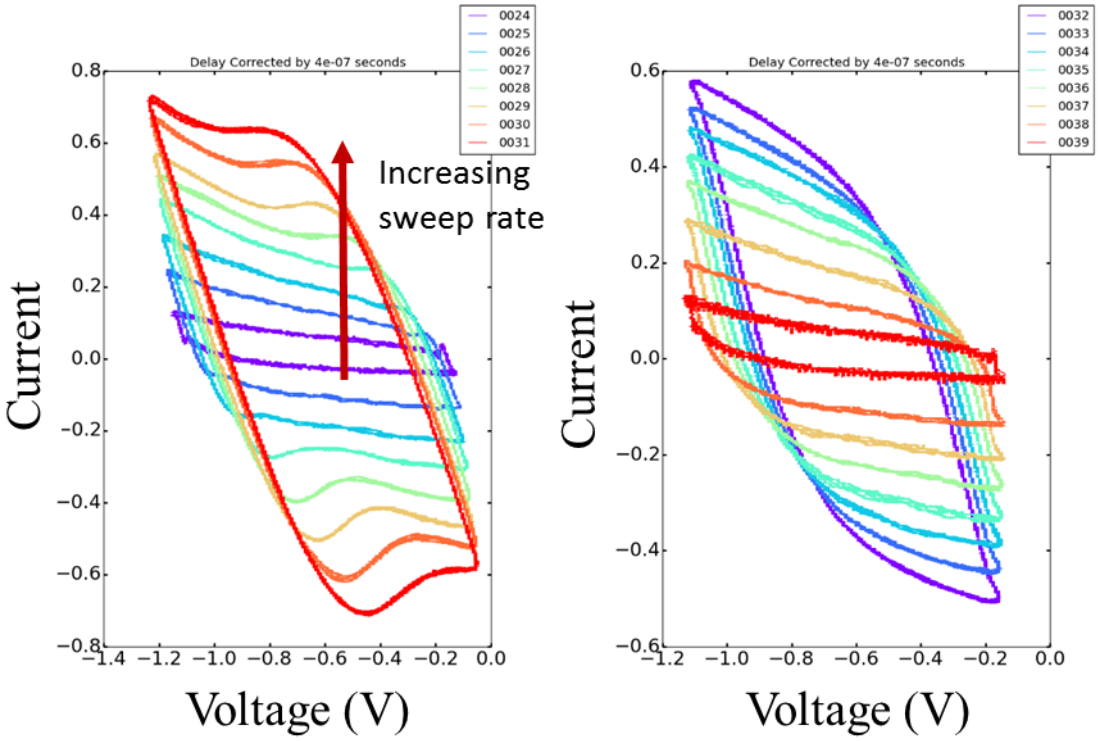

Figure 5. 3 The effect of iR drop compensation on a voltammogram of clean Pt electrode in a MeCN solution containing 0.1M TBAP. Voltammogram with iR compensation(left), without iR compensation (right).

As briefly mentioned previously, the benefit of the high sweep rates afforded by a custom instrument that can correct for the iR drop while still following and applying voltages at the specified timescales is the possibility of decoupling stepwise processes. One example of such process, as briefly mentioned in Chapter 1 of this thesis, is the electrochromic behavior of conjugated polymer films. These materials change color under bias and is utilized in smart glass applications in cars, airplanes and windows. Among the limiting factors in widespread utilization of these electrochromic devices in different applications (such as displays) is the time scale of the color change (~ ms-s) especially for larger devices. Although the color change process is a simple redox reaction that is initiated by an electron transfer

due to the applied potential (which should happen much quicker), the color change occurs at a much longer timescale. This is due to the time required for the built up charge to be compensated by the diffusion of the counter ion. The limiting presence of the counter ion diffusion on the electron transfer kinetics of conjugated polymers are well known and is summarized in the following z-scheme in Figure 5.4 where redox reactions are denoted with the diffusion of the corresponding counter ion [21]. The electrochemical kinetics of these well investigated materials are all operated under this limiting case.

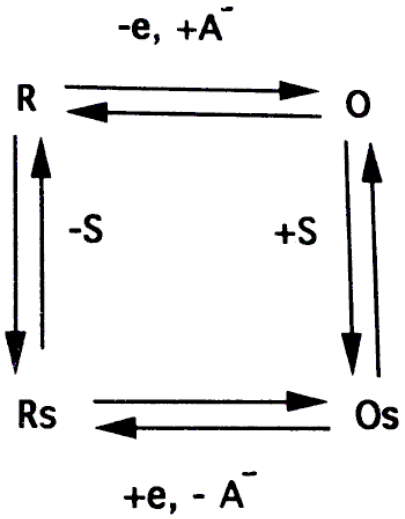

Figure 5. 4 Square scheme of electron transfer kinetics as depicted in the literature for a conjugated polymer. Reproduced with permission from [21].

For a polymer film deposited onto an electrode, using ultrafast cyclic voltammetry, it is possible to achieve high sweep rates such that the diffusion layer thickness becomes comparable to the thickness of the polymer film where the effect of diffusion on the measured behavior is decoupled as depicted in Figure 5.5. As cyclic voltammograms are collected at different sweep rates, this behavior is signified by

a change in the dependence of peak currents to the sweep rate. At the diffusion controlled regime, as determined by the Randles-Sevcik equation (as mentioned in the Basics of Electrochemistry section), a $v^{1/2}$ dependence is observed while for lower sweep rates the dependence becomes v which is a signature of the electrochemical activity of the surface bound species, in this case the conjugated polymer. Therefore, by investigating the sweep rate dependence of a given peak, it is possible to extract the critical timescale for the electrochemical process where the diffusion limit is lifted.

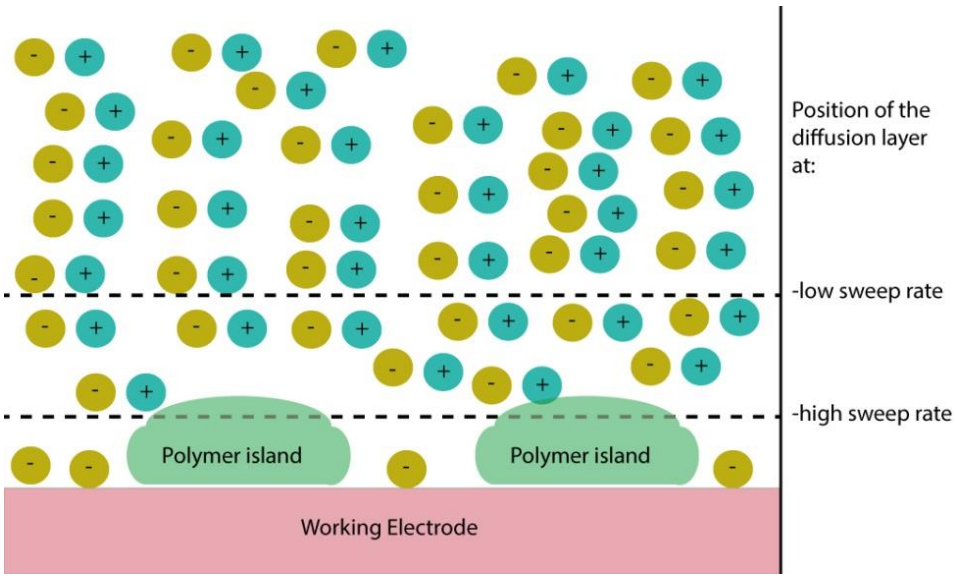

Figure 5. 5 The depiction of the diffusion layer at high and low sweep rates when a polymeric island is deposited on to an electrode.

For electrochromic materials, a complementary method for the above outlined Ultrafast Cyclic Voltammetry is UV-Vis Spectroscopy where UV-Vis spectra can show the relative amount of contributions from the two color states of the electrochromic material. The problem, however, is that the spectra acquisition times for a given UV-Vis Spectrometer cannot catch up to the sweep rates of interest in

Ultrafast Cyclic Voltammetry. In the literature, fast electrochemistry of electrochemically-generated chromophores was investigated using absorption spectroscopy in scattering geometry. Two variable wavelength lasers of relatively low power was used and partial absorption spectra of transient species were obtained. The high resistance of the electrodes employed, however, limit the method where the study employs a potentiostat without iR compensation capabilities. Two issues arise for such an experiment; first the presence of high electrode internal resistance limits the sweep rates achieved while the partial absorption spectra take a long time to collect since it is collected wavelength by wavelength [119]. Instead, in our setup, we utilize a fiber optic UV-Vis spectrometer that acquires full spectra while cyclic voltammograms at high sweep rates are swept using the Ultrafast Potentiostat outlined. As mentioned, the spectrometer cannot keep up with the speed of the electrochemical sweeps employed, thus, the obtained individual spectra are expected to be super position of various color states that are measured during many sweeps. Data analysis tools such as Principal Component Analysis and Linear Discriminant Analysis can then be used to separate the relative contributions from each color state at different timescales (determined by the sweep rate). By obtaining a definitive picture of the processes taking place across multiple timescales afforded by Ultrafast cyclic voltammetry, it will be possible to fine tune the electrochromic response for optimal device operations by characterizing the effect of various counter ions, morphology of the polymer film, identity of the polymer, possibility of additives to facilitate ion transport etc...

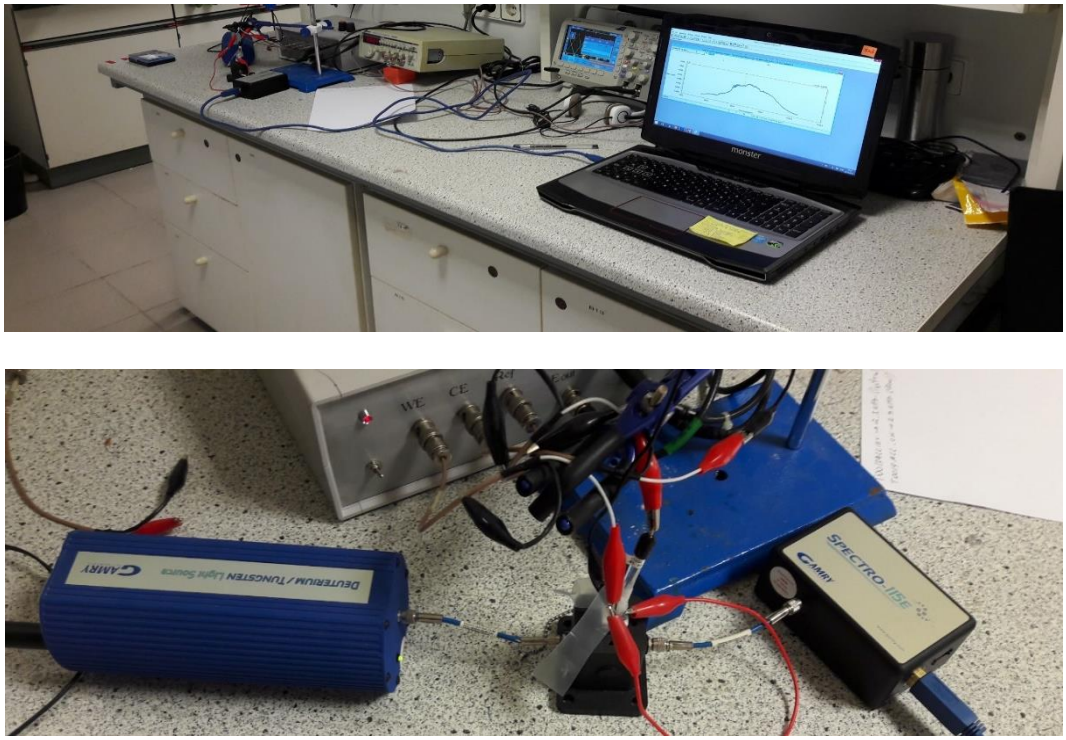

Figure 5. 6 The Ultrafast Spectroelectrochemistry setup with a function generator to generate the triangular excitation and an oscilloscope to follow the response with a Gamry fiber optic UV-Vis Spectrometer (top). The three electrode setup inside the spectrometer chamber (bottom).

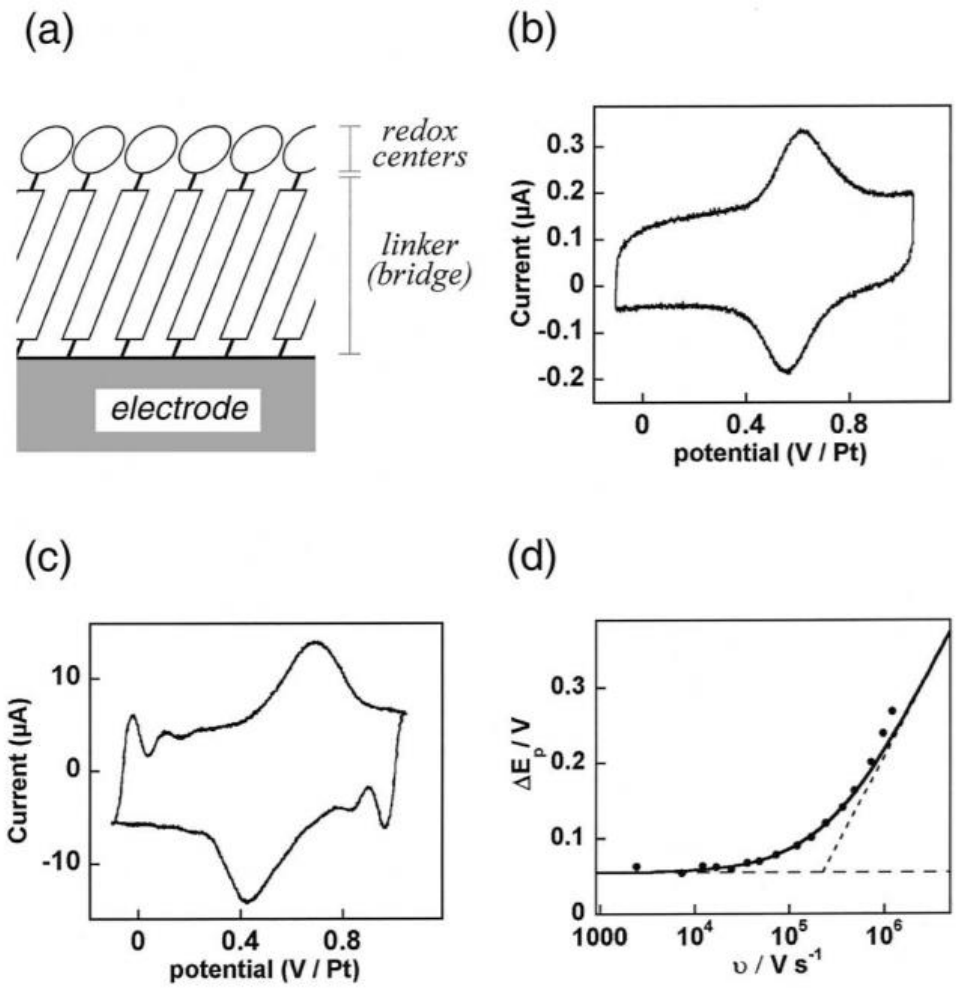

Figure 5. 7 a) Self assembled monolayer adsorbed on to a working electrode with pendant redox centers. b) The peak shape at a relatively low sweep rate. c) The peak shape at a high sweep rate. d) Peak separation vs. sweep rate. Reproduced with permission from [109].

In the literature, ultrafast cyclic voltammetry with on-line iR compensation has been used to elucidate the details of the heterogeneous electron transfer reactions the results are reviewed elsewhere[109]. In a particular example, the electron transfer kinetics of a redox active self-assembled monolayer was probed using conventional and ultrafast cyclic voltammetry [110]. The peak shape at low sweep rates is symmetrical and Nernstian while at higher sweep rates, the peak shapes

become slanted. Especially the anodic reaction becomes kinetically limited as evidenced by the peak shape. Quantitatively, the behavior is seen in the peak separation where two distinct dependencies can be obtained. At low sweep rates, the peak separation is constant (at ~55mV) with sweep rate while at higher sweep rates the peak separation increases rapidly. As sweep rate becomes larger, the timescale of the experiment becomes smaller and smaller where at a certain point, the kinetics are limited by the electron transfer taking place at the electrode surface. The measured heterogeneous electron transfer rate constant ($k = 4x10^6\ s^{-1}$) is consistent with strong coupling between the electrode surface and the redox centers. Further work using dendritic assemblies adsorbed onto electrodes reveal that this coupling is through the translation of the redox centers towards the electrode surface to pick up/let go of electrons [109]. These findings demonstrate the power of the method where the rather stationary picture of electron transfer becomes dynamic at the timescales unlocked.

5.2 Potentiostat Circuitry

As mentioned briefly in the Basics of Electrochemistry section, potentiostatic control over the system of interest is achieved by the utilization of OpAmps. OpAmps are linear circuit elements that allow a variety of operations as their name suggests such as addition, subtraction, multiplication, integration and differentiation. Moreover, their high input impedance and low output impedance allows potentials to be measured without adverse effects on the potential to be measured and without changing the load respectively. Usually OpAmps have two

inputs, an inverting and a non-inverting. The basic operation of an OpAmp is to subtract the inverting input from the non-inverting input and output a signal that is proportionally larger than this difference as shown;

$$E_{out} = A(E_{inverting} - E_{non-inverting})$$

"A" here is called the open loop gain of the OpAmp and constitutes the upper bound on the amount of amplification that can be achieved by a given OpAmp at a particular bandwidth. To demonstrate the working principle of an OpAmp, looking at a simplified equivalent circuit is helpful and is as follows. Inputs of the OpAmp can be thought to be connected to each other via a large resistor (>10MΩ) which constitutes its high input impedance. The output side then can be visualized as an individual voltage source with a small resistor in series (<10Ω) which is the output impedance of the OpAmp as shown in Figure 5.8.

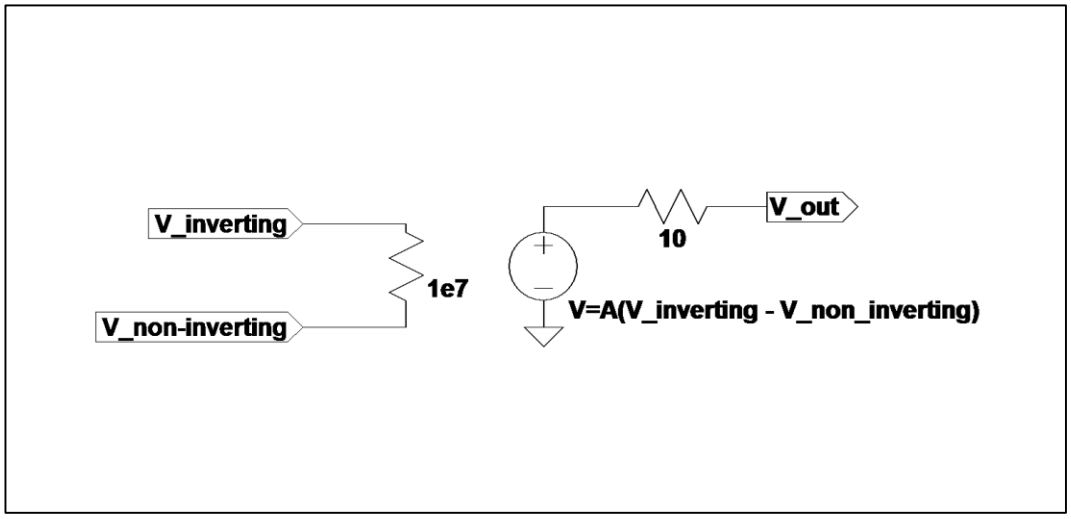

Figure 5. 8 The equivalent circuit model of a real OpAmp.

As shown, the high resistance between inputs forces both of the inputs to the same value without drawing appreciable current from either such that the current input to

the OpAmp is negligible while the output voltage is generated from a source that is not directly connected to the inputs (i.e. the current that is required to match the voltages of the inputs are not drawn from the inputs but rather the power supply of the OpAmp is used to draw the current). This allows the input voltages to be read without modulating the system while still amplifying the input signals by the gain "A".

In Figure 5.9 a conventional potentiostat with a couple of twists can be seen. The potentiostat was designed for long term experiments (water splitting) where constant potentials over periods of weeks were to be applied at relatively high currents (mA to A) to a 3 electrode setup. Although a commercial potentiostat can easily be used for such purposes, they are much more expensive compared to the instrument outlined here. Moreover, commercial potentiostats can be used for variety of other/more complicated experiments. Therefore, using a commercial potentiostat for a simple experiment that takes weeks is not efficient utilization of instrument time. Instead, a simple potentiostat can be built. For this circuit LM741 OpAmps were used owing to their wide availability and their high stability. These OpAmps, however, do not have enough output currents for our application. To achieve the current requirements, two transistors (one for negative currents and one for positive currents) were used as current boosters. The utilization of these boosters necessarily required us to adopt a grounded working electrode. If the working electrode is not grounded, then the potential at the working electrode (with respect to the circuit ground) presents itself as an offset potential such that the transistors cannot be turned on. When the working electrode is grounded, however, this offset

does not exist and the transistors symmetrically transmit for both positive and negative currents. Moreover, rather than using a function generator to apply the constant potential, a voltage divider with a variable resistor is used to drive the voltage output of an OpAmp in the comparator geometry as shown as OPAMP1. This signal is then fed into the summing point of the function generator compared to the potential of the reference. The function generator input is completely optional for this circuit and in standard operation of this potentiostat, it is not used. A simple mathematical representation of the feedback loop that controls and measures the potential at the electrochemical cell is as follows;

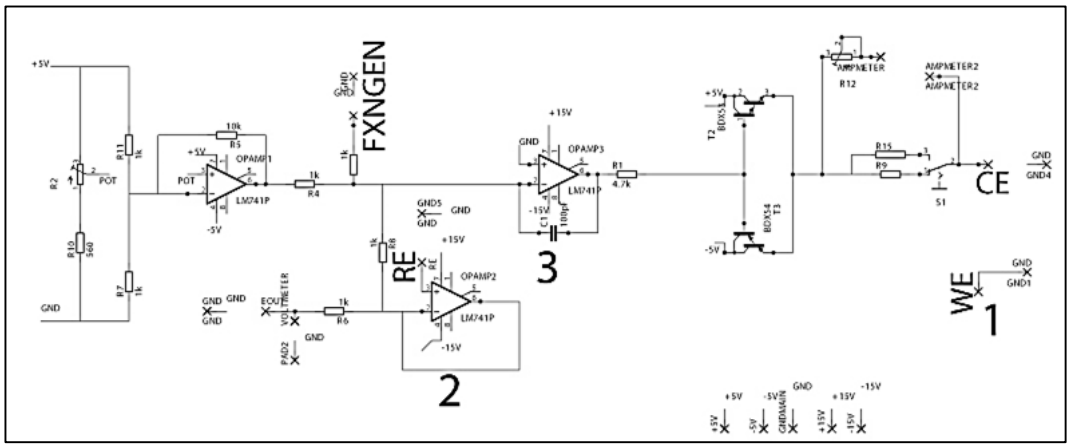

Figure 5. 9 Circuit schematic of a high stability potentiostat with current boosters and a step voltage generator.

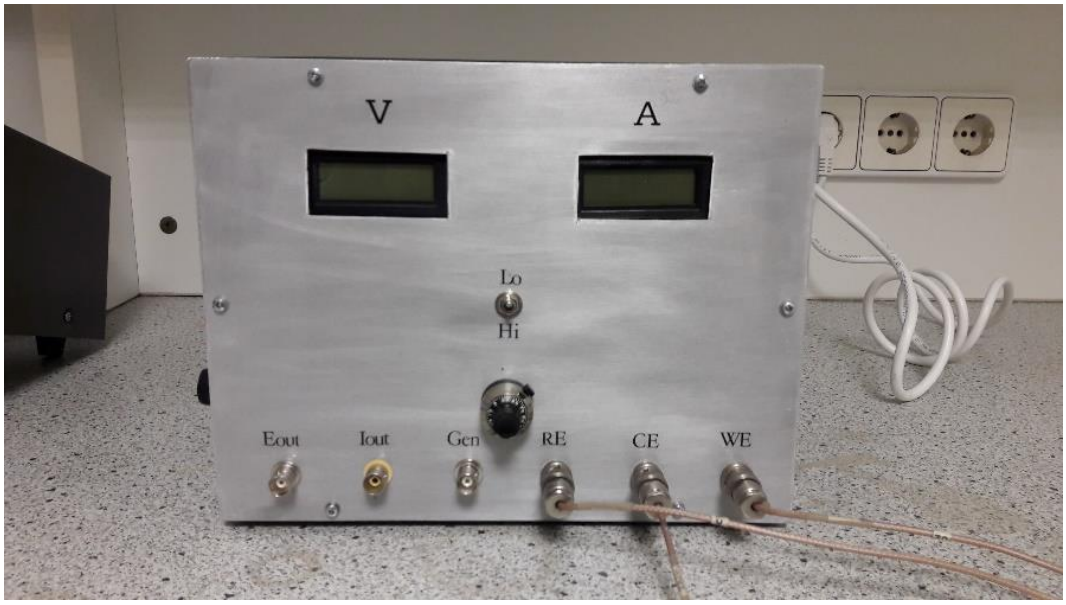

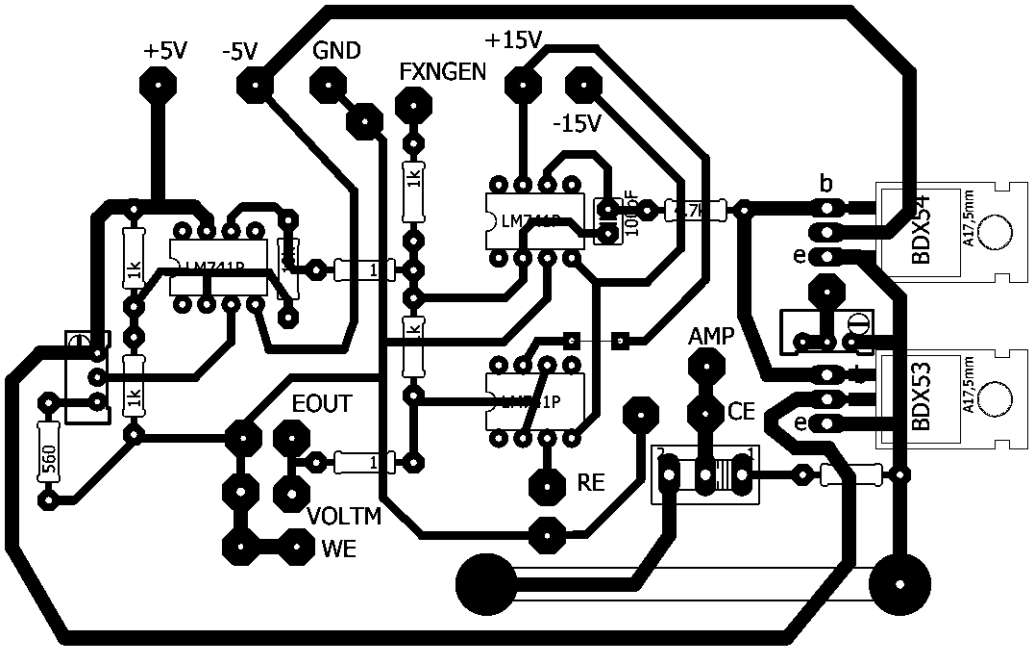

Figure 5. 10 The built instrument with two multimeters to follow the voltage and the current (top). The circuit design for a printed circuit board (PCB) (bottom).

The DC potential that is going to be applied is generated by the voltage divider at the left hand side where the 5V input is divided into 2.5V and fed into the inverting input of the OpAmp while the same potential is divided into R2/((10kΩ-R2) +

560Ω) and fed into the non-inverting input. R2 here is a variable resistor which is controlled by the operator. For example, when R2 is adjusted such that its value is 3.52 kΩ, the ratio becomes 1/2 and the potential at the inverting input becomes 2.5V, in this case OPAMP1 has 2.5V in both its inputs therefore it outputs exactly 0V. Similarly, when R2 is adjusted to 4kΩ, the ratio becomes 0.61 and a potential of 3.04V is applied to the non-inverting input, a negative constant potential is generated. To generate the same potential, however in the opposite bias, R2 is simply adjusted to 3kΩ, the non-inverting input becomes 1.98V and therefore a positive bias is generated. For simplicity let's call this user controlled potential E_{DC}. OPAMP2 here is called an electrometer and is responsible for measuring the potential difference between the input potentials ($E_{DC} + E_{FXNGEN}$) and the reference potential (E_{RE}). The output of this electrometer forms the net applied potential and the output is read from the E_{out} output where;

$$E_{out} = -[(E_{DC} + E_{FXNGEN}) - E_{RE}]$$

This output is then fed into the control amplifier, OPAMP3, and is compared to the circuit ground;

$$E_{out} - E_{ground} = 0$$

Recognizing that the working electrode is at the circuit ground (i.e. $E_{ground} = E_{WE}$);

$$E_{out} - E_{WE} = 0$$

Plugging in E_{out};

$$E_{WE} - E_{RE} = -(E_{DC} + E_{FXNGEN})$$

Therefore, the potential difference between the working and the reference electrodes are controlled at the potential imposed by the inputs. The current required to hold the potential at this value is then supplied to the counter electrode by the transmission of the appropriate transistor and the current is read over a shunt resistor (R15 or R9) of known value.

The ultrafast potentiostat works using a similar circuit, however, the working electrode is not strictly grounded but rather its potential is compared to the ground using another OpAmp [105]. Moreover another OpAmp with a variable gain (user controlled) is employed to compensate for the iR drop[5].

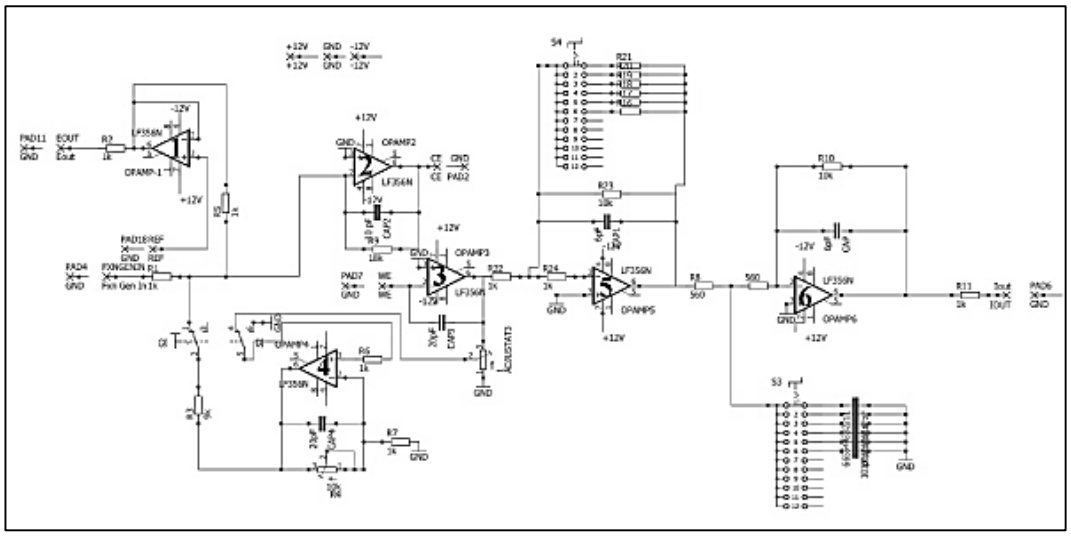

Figure 5. 11 The circuit schematic of an Ultrafast Potentiostat with positive feedback iR compensation.

[5] Small tweaks to the circuit published in the reference [105] were made for our instrument.

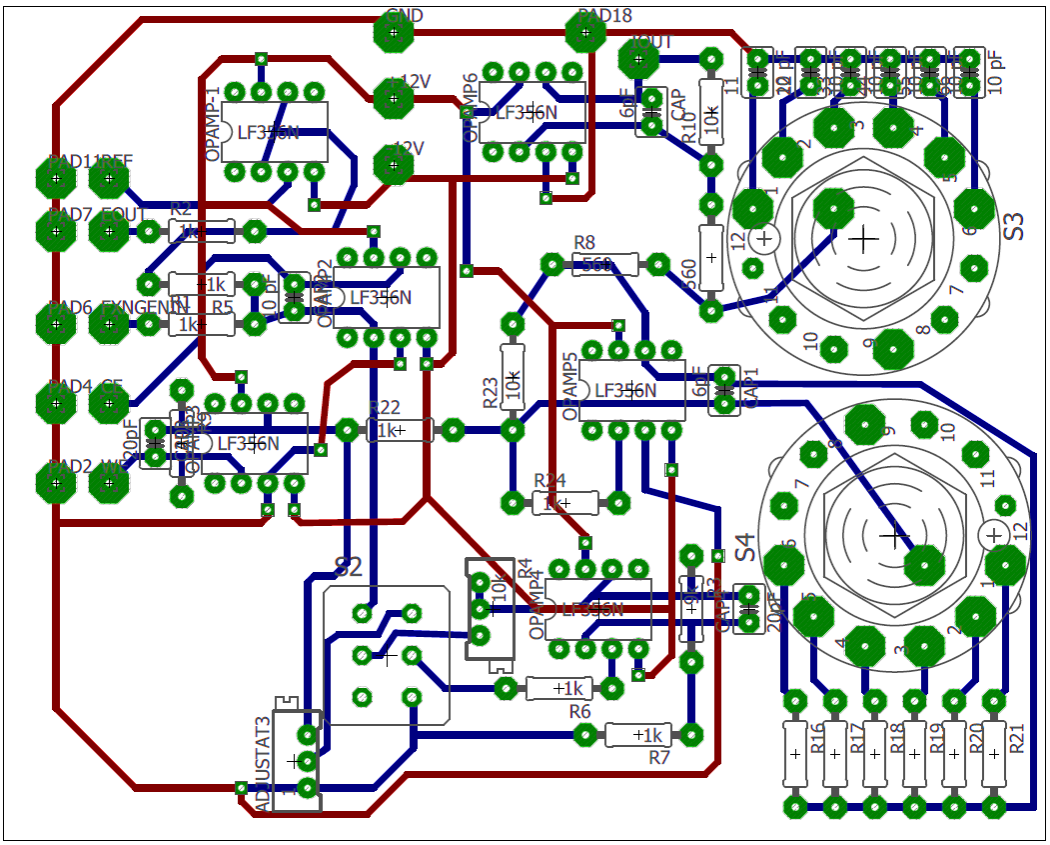

Figure 5. 12 A two layered PCB of the Ultrafast Potentiostat.

In Figure 5.11 OpAmp denoted by 1, similar to OPAMP2 in the previous schematic is in the electrometer/voltage follower geometry and is responsible for following the voltage difference between the reference potential and the circuit ground ($E_{electrometer} = E_{RE} - E_{ground}$). The current passing through the electrochemical cell, is measured as a voltage after an amplification (OpAmp labeled as "5") and a low pass filter stage (OpAmp labeled as "6"). The amplifier "5" has the current supplied by the OpAmp labeled as "3" as an input in the inverting amplifier geometry. Depending on the user controlled value of the resistance in the feed-back path of "5", the voltage signal is amplified. The variable gain allows the instrument to be operated for large range of currents (nA to mA). Following amplification, a

low pass filter whose frequency is user controlled is employed. The value of the capacitor that goes to the ground determines the critical frequency of this filter and usually current is read without any filters since the waveforms of interest are fast. The previous instrument introduced, the conventional potentiostat with current boosters, achieves current to voltage conversion (I/E conversion) simply by reading the voltage developed over a resistance of known value. The two stage I/E conversion shown is superior to this simple approach in multiple ways. Amplification and filtering allows high current resolution while more importantly, the low output impedance of the OpAmps (as shown in Figure 5.8) is utilized to read the current without modulation. The simple I/E converter that employs a resistor of known value necessarily modulates the load by introducing a resistor in series to the load. iR compensation is accomplished by the OpAmp denoted as "4". It gets the current output at the working electrode and generates a voltage based on the value of the user controlled resistor in the feedback path. Let's call this voltage output E_{IR}. This potential is then added to the function generator input and the output of the electrometer. This summed signal ($E_{electrometer} + E_{IR} + E_{FXNGEN}$) is then sent to the control amplifier ("2") which generates the most of the current that flows through the circuit. The non-inverting input of the control amp is at the circuit ground that is;

$$E_{electrometer} + E_{IR} + E_{FXNGENIN} = 0$$

Noting that the electrometer measures the reference potential with respect to the circuit ground;

$$E_{RE} - E_{ground} + E_{IR} + E_{FXNGENIN} = 0$$

Further, the potential of the working electrode is held at the circuit ground by the current follower labeled “3”.

$$E_{RE} - E_{WE} + E_{IR} + E_{FXNGENIN} = 0$$

Rearranging the equation;

$$E_{WE} - E_{RE} = E_{IR} + E_{FXNGENIN}$$

Thus, the potential between the working and reference electrodes are hold at the potential dictated by the function generator while the potential lost to the solution resistance is compensated by E_{IR}.

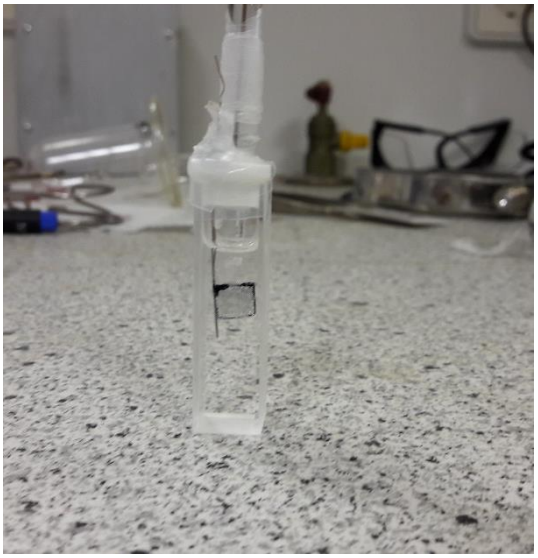

Figure 5. 13 The three electrode setup in a quartz cuvette.

5.3 Discussions and Future Work

The conjugated polymer to be investigated needs to be deposited on to a conducting working electrode to be able to run these experiments. Moreover, the electrode needs to be transparent enough to obtain UV-Vis spectra. FTO glass slides were initially used as such an electrode, however, overall high resistance of FTO inherently causes large time constants and complicate the experiments. Instead a Pt mesh electrode was used. Polymer films can be obtained either by drop casting from the already polymerized material or by electropolymerization of the monomer solution which after polymerization directly deposits onto the electrode surface. For the initial work outlined below, a thick PEDOT:PSS film was drop casted onto the Pt electrode. The electrode setup in a quartz cuvette can be seen in Figure 5.13. Using a conventional potentiostat, the slow sweep rate behavior of the polymer film can be probed. A large oxidation wave followed by a large and broad reduction can be seen at the slow sweep rates.

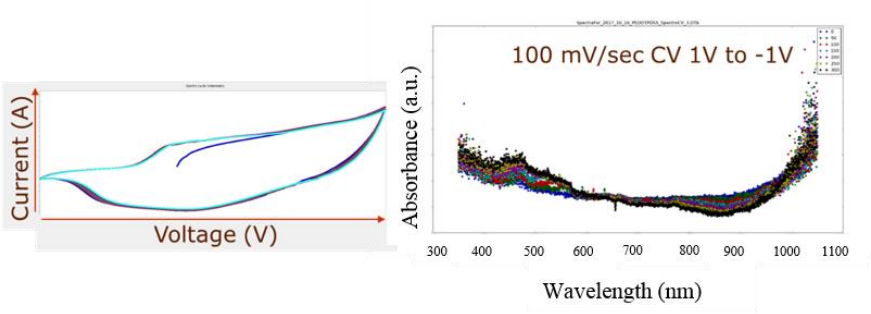

Figure 5. 14 Cyclic voltammograms at 100 mV/s (left) of drop cast PEDOT:PSS film onto Pt mesh electrode, UV-Vis Absorbance spectra collected simultaneously (right).

Cyclic voltammetry at higher sweep rates however point towards a couple of issues with this PEDOT: PSS film. First the obtained voltammograms are all capacitive

even when iR compensation is fully employed. This is due to the high resistance of the visibly very thick PEDOT: PSS on the electrode. The resistance is so high that we need a larger resistance in the feedback path of the OpAmp labeled "4" in Figure 5.11.

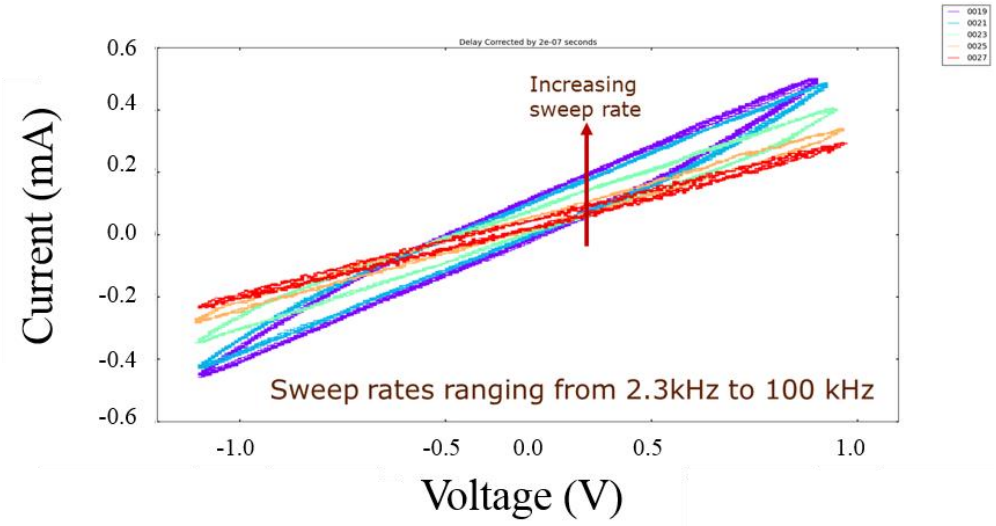

Figure 5. 15 Cyclic voltammograms of a drop cast PEDOT: PSS film onto Pt mesh electrode.

Without any analog modifications to the system, this can be remedied by drop casting a thinner polymer film and will be the direction of the future work. Another issue with this particular PEDOT: PSS film is its stability as evidenced by the UV-Vis spectra collected over a period of 15 minutes while the potential is swept at the specified sweep rates continuously in Figure 5.16. Although the evolution of the spectra with no applied potential is distinct from the cases where a potential is applied, the fact that no appreciable change in progression between the UV-Vis spectra obtained for the polymer film across 2 orders of magnitude in terms of timescale points towards a stability issue rather than an actual polymer response. Further investigations with the Ultrafast Potentiostat, however, at slow sweep rates

to match the results with the commercial potentiostats is required for experiment credibility as well as to show the benefits of iR compensation even at mild sweep rates.

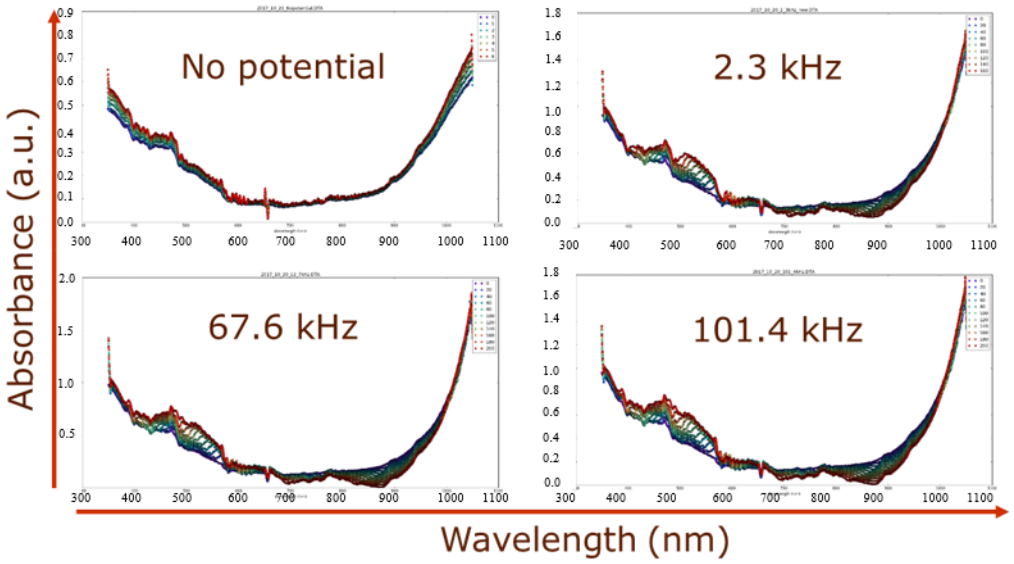

Figure 5. 16 Aggregate UV-Vis Spectra of a drop cast PEDOT: PSS film onto Pt mesh electrode during ultrafast cylic voltammetry experiments at the specified sweep rates (Wavelengths ranging from 300 to 1100nm). (Colors going from blue to red signify later times.)

5.4 Conclusion

The premise of Ultrafast Spectroelectrochemistry is being developed to investigate electron transfer kinetics of conjugated polymers decoupled from the consequent counter ion transport to achieve electroneutrality. The need to achieve high sweep rates and the increase in Ohmic losses requires special instruments to be built for this custom application. The specific circuitry to build a potentiostat that can sustain the sweep rates required while correcting for the Ohmic loss is discussed, along with the operational principles of a regular potentiostat in terms of analog circuitry.

A potential way of obtaining broadband spectra to probe the color states of conjugated polymers for electrochromic devices was described along with initial results regarding the Ultrafast Spectroelectrochemistry of PEDOT: PSS films.

Chapter 6

6. Ionic Liquid Modelling

6.1 Introduction

Ionic liquids attract attention as green and safe alternatives to conventional electrolytes owing to their low vapor pressures and thermal stability. Aside from applications in material synthesis and sensors, they attract interest from the energy storage and conversion community as the choice of electrolyte for both conventional fuel cells/batteries and the next generation devices [120]. Especially their non-volatility allows devices to meet strict safety criteria while still maintaining their high performances

In the so called “beyond Li-Ion batteries”, a common problem is the stability of the active materials where the regularly used carbonate based organic solvents are decomposed rapidly by the highly active electrode materials. For instance, in Li-O_2 and Li-S chemistries, these common electrolytes cannot be employed. Ionic liquid electrolytes constitute an interesting alternative where the ionic behavior of the electrolyte can be tuned depending on the structure of the ion pairs utilized, thus allowing them to be tailored as electrolytes for specific applications. Trying all combinations of different ions for every application, where there are extremely high number of available structures for both ions, is not viable. Regardless, studies to tailor the electrolyte for specific energy storage systems have been recently reviewed [120]. Although device safety is improved by utilizing tailored ionic liquids, most of these studies especially for the current commercial technologies (such as Li-Ion batteries), show that device performance is hindered. For instance, Li-Ion batteries with tailored ionic liquid electrolytes either show poor cycling capabilities [121] or only show good cycling stability at low C rates (such as 0.05C) [122]. Thus, fundamental understanding on the response of the ionic liquid and the processes that govern this response, aside from the choice of ionic liquid should be examined. To lay a solid foundation for investigations towards the faradaic processes which are inherently different compared to their dilute electrolyte counterparts (see Chapter 1 and 4) a better understanding on the non-faradaic processes, namely double layer formation and its kinetics need to be developed.

Even though ionic liquids are entirely based on ions, reports show that a significant fraction of the ions exist in an equilibrium with the ion-pairs[11]. Measurements

indicate that the ion pairing is significant depending on the structure of the ion and can get up to 10%. Further, an often overlooked aspect of the ion pairing is the fact that the event is dynamic, that is the ion pairs can form and break as the system equilibrates in response to a perturbation.

Both experimental and theoretical studies attract attention in the literature where the low volatility of ionic liquids allows vacuum techniques to be utilized while on the theory side, mean field models are employed. Experimentally, X-Ray Photoelectron Spectroscopy (XPS) have been utilized to follow the response of ionic liquids[13,16,123–125] and characterize ion screening effects at extended distances [16] while mean field models were developed to explain ion movement right at the ionic liquid-electrode interface [2,14]. Since these mean-field models are computationally expensive, it is not possible to extend these theories to the experimentally relevant length and time scales. Moreover, due to the X-Ray spot-size of a conventional/laboratory XPS, it is not possible to push the resolution down to the length scales explained by mean field models. To bridge this gap in length scales and also to be able to dynamically model the response of an ionic liquid across multiple timescales ($10^{4\text{-}5}$ Hz), a much simpler coarse grained electrostatic model is described in the following sections.

6.2 Modelling Considerations

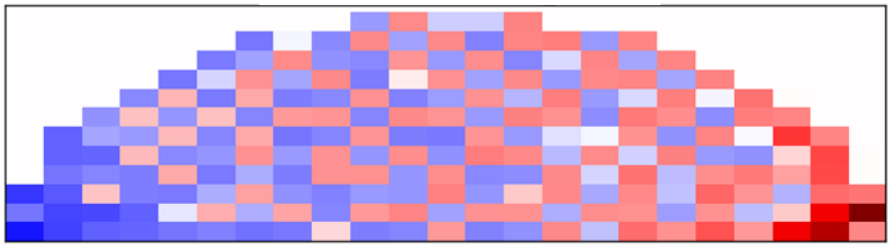

Figure 6. 1 The depiction of the dissected ionic liquid drop in terms of rectangular grids.

Using a Python dictionary, the ionic liquid drop is dissected into rectangular grids containing charged (positive and negative) and neutral (ion pairs) particles as shown in Figure 6.1. Each grid is assigned as a key in the dictionary with the two dimensional position of the grid as the value of the key. Each key is structured such that it has an array of 4 values, the number of positive, negative and pair particles and the voltage of the given key. A semi-circle is chosen as the modelled geometry. Owing to angular symmetry, projection into higher dimensions or a full circle is possible, yet it unnecessarily would increase simulation runtimes. Each grid in the semi-circle is defined by their initial amounts of particles (positively/negatively charged and pairs), voltage and their positions. The voltage of each grid is assigned initially by assuming a linear drop with position much like a resistor[123]. Excess charges on every grid exerts an electrical potential in all other grids calculated from a simple coulomb formula. This potential due to excess charges is added to the initial voltage assigned. Once the potential of each grid is calculated, an electric field is formed based on voltage differences between neighboring grids. The formed

electric field migrates charges between grids based on a simple definition of charge mobility. Particle diffusion is handled by generating uniform random numbers that cycle through possible neighboring grids. The amount of particles each grid can hold is limited by a threshold. If through migration and diffusion this threshold is exceeded, the excess particles are moved away from grid in question towards their neighbors. If the neighbors exceed the particle threshold, then those particles are again moved further away from the concentrated region until all grids satisfy the given threshold. In the end, the following association equilibrium is maintained for each grid.

$$positive + negative \leftrightarrow pair \qquad K = \frac{n_{pair}}{n_{neg} \cdot n_{pos}}$$

The above mentioned actions are repeated for each time step. The number of time steps for a given configuration is fixed to ensure uniformity in terms of data points in the simulations. The implicit time between these constant number of time steps is however subject to change depending on the frequency simulated. The implicit timescale (with a defined mobility of the ions) forms an upper limit for the least amount of electric field that can displace a single charge between two adjacent grids and depending on this electric field threshold, migration is handled as described above.

For all time steps, the above considerations are repeated and the resulting voltages can be visualized as a voltage-time trace for all grids in the simulation. The collections of these voltage-time traces for all boxes can then be further processed to other physical observables (using XPS) such as the probability density or the

mean voltages. The probability density 3-d histograms were plotted by binning the V vs t trace of all surface grids and then by plotting them as a function of horizontal distance. The mean voltages can be obtained by subtracting the voltages simulated when positive potentials are applied by the voltages simulated when negative potentials are applied. The resulting values can be visualized as a 3D bar chart with the z axis as the voltage amplitude simulated.

For all simulations (see the figure caption for frequency chosen), the following parameters were used;

number_of_pairs = 250, number_of_grids = 200, nplus = 500, nminus = 500, lateral_drop_length = 2, mobility = 5e3, transference_plus = 1.0, transference_minus = 1.0, K_association = 0.1, excess = 10, number_of_time_steps = 100

The simulations and the data processing were all done in Python 2.7.10.0 using a Python(x,y) shell with Numpy, Scipy, Matplotlib and Mayavi open source packages.

6.3 Results and Discussions

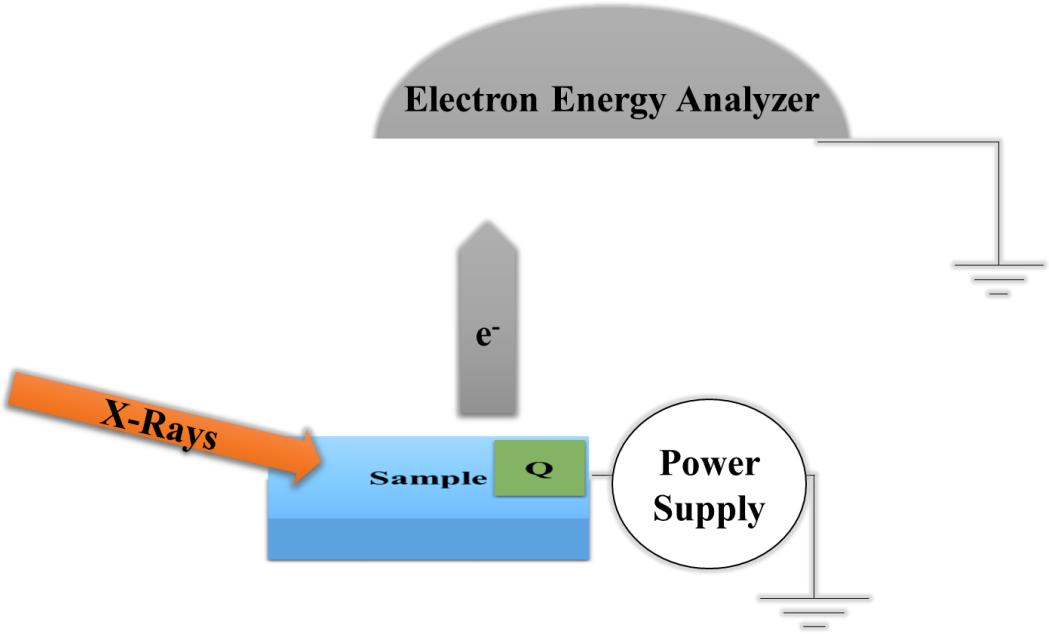

Figure 6. 2 The depiction of the photoelectron ejection upon X-Ray irradiation under external bias supplied by the power supply with surface charge "Q" introduced by the ejected electrons.

XPS measures binding energies of core level electrons by exciting samples using X-Rays of known energy. The kinetic energy of the ejected electrons as a result of photoelectric effect is measured as shown in Figure 6.2 and Eq. 6.1. The conservation of energy, considering the incoming X-Ray energy, the kinetic energy of the ejected electron, the potential introduced by the surface charge and under an external applied bias can be written as the following;

$$B.E = hv_{X-Ray} - KE\ (e^{-}) - \Phi - V(due\ to\ Q) - V(external) \qquad (6.1)$$

Thus, for a conducting sample which has negligible surface charging and without an external bias, the difference between the energy of the incoming X-Ray and the kinetic energy of the particular electron coming from a certain, element specific

core level, yields the binding energy for that level. As shown in Eq. 6.1, under external bias, binding energies shift with respect to the applied potential, similar to binding energy shifts due to surface charging as a result of the ejected electrons for an insulating sample without any external bias. Thus, in essence, XPS can be used as an oscilloscope with spatial resolution and chemical resolution by mapping the surface binding energies. Spatial resolution of the technique is limited by the X-Ray spot-size (~30 μm for the instrument used), while the temporal resolution is limited by the time required to collect a single spectrum.

During a routine XPS experiment on ionic liquids, the binding energies while applying bias constitute a vast dataset, especially when obtained in a time resolved fashion. Data visualization can be achieved either by taking line scans over the ionic liquid surface (Figure 6.3-a) and following the shift in the binding energy with respect to the unbiased signal or by mapping a specific region of binding energy over the ionic liquid surface (Figure 6.3-b). If an alternating voltage (such as a square wave or a triangular wave) is applied, due to the timescale of a line scan, both the minimum and the maximum of the applied voltages are reflected as a voltage response at the same time. In the line scan this is directly seen as two distinct lines while for the surface mapped plot this is seen as the peak potential difference (i.e. 4V – (-4V) = 8V). Correlating the simulated data to these observables can be achieved either by generating histograms of the modeled voltage response and then stacking them with respect to position (Figure 6.4-a) or by looking at the mean differences in positive and negative cycles of a simulated square wave and plotting them as a function of distance (Figure 6.4-b).

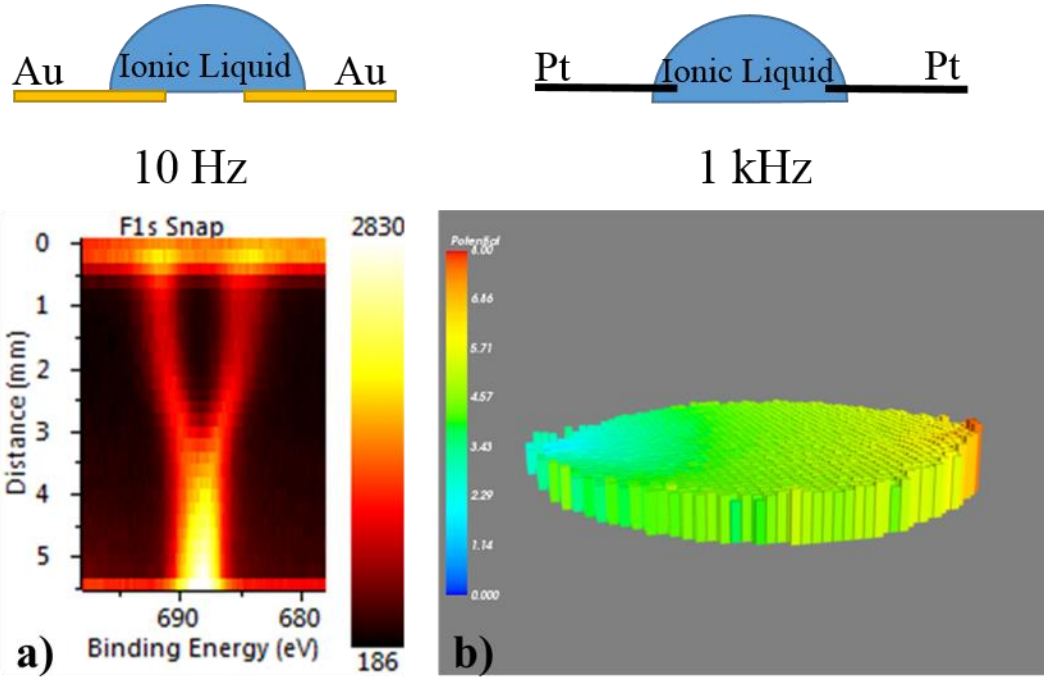

Figure 6. 3 The binding energy shift under square wave bias (alternating between 4V and -4V) a) visualized by a line scan for an ionic liquid drop between two planar Au electrodes. b) visualized by mapping the whole ionic liquid surface for two Pt point contacts (the colorbar and the height represents the voltage of the particular point).

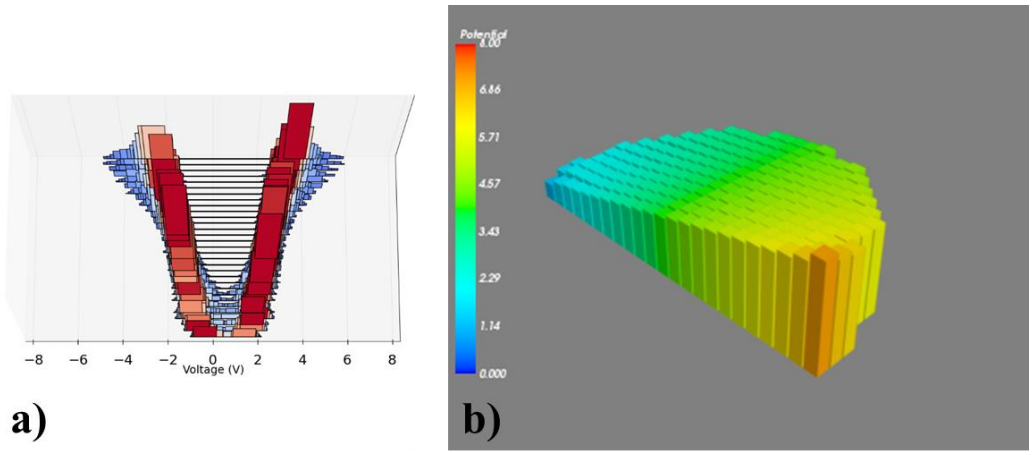

Figure 6. 4 Simulated voltage response of the ionic liquid, the obtained voltage profile is visualized a) as histograms b) as a surface plot of mean potential difference in the positive and negative cycles (the colorbar and the height represents the voltage of the particular point).

Applying square wave voltages to ionic liquids using electrodes with symmetric contact areas while monitoring the binding energy shifts using XPS show that, if

given enough time to equilibrate and reach a steady state, a binding energy shift that is half of the applied amplitude is observed. The difference in potential between the applied and the measured potentials is due to potential lost at various interfaces. Namely, around the vicinity of the electrode as a response to the applied potential, charge rearrangement occurs and an electrochemical double layer forms. Noticing that there are two symmetrical contacts, one at the source electrode side and one at the grounded electrode side, equal amounts of potential is screened across the two double layers and therefore at the steady state, exactly half of the applied potential is seen as the major binding energy shift throughout the surface of the ionic liquid. Although near the source and grounded electrodes, simple equivalent circuit models involving RC circuits can explain the voltage evolution over time and frequency as previously published for ionic liquids [16], SiO_2 samples to extract the parameters of the equivalent circuit [126] and to investigate the effects of surface charging at various surface heterogeneities[127]. Such models, however, fail to capture the spatial dependence of the voltage. Equivalent circuit models with the given time constant cannot explain the various position dependent voltage traces obtained away from the electrode simply due to the fact that a regular capacitor does not have a spatial component. The equivalent circuit fits, however, in their region of relevance show that electrostatic models can be effective in explaining the voltage screening behavior in these systems. Thus the only issue that needs to be tackled in adequately modelling these systems, in the time scales and length scales relevant to the experimental results, is the addition of spatial arguments to the electrostatic

model supplied by the equivalent circuit fits which we have achieved through the above explained modelling considerations.

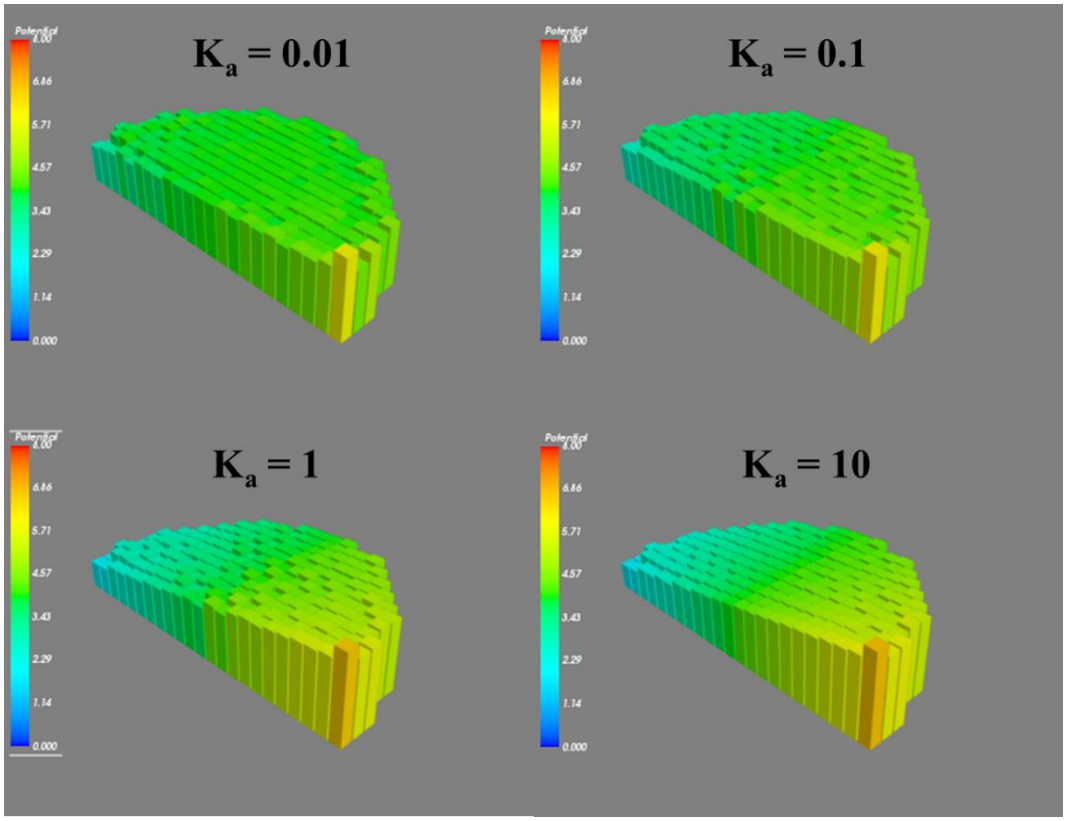

Figure 6. 5 Simulated voltage profiles as a function of the association constant at the same simulated frequency.

The profound effect of association equilibrium on the observed voltage profiles can be seen in Figure 6.5. Association equilibrium directly controls the number of available charged particles. These charged particles are the ones that screen and shield the applied potential therefore if the tendency to form pairs is high (i.e. if the association constant is high) the external bias applied is no longer shielded and shows resistive behavior as characterized by the linear voltage-distance relationship in the timescale of the simulations. Similar unscreened, resistive behavior can be experimentally demonstrated under XPS for a graphene sheet under external bias

[123]. For graphene devices the observed resistive behavior is the result of purely electronic voltage distribution without contribution from ion transport to screen the voltage which is similar to the high association constant case simulated in Figure 6.5. Association equilibrium therefore, is a crucial factor in appropriately modelling the charge screening effects in ionic liquids since the amount of association can explicitly switch the mechanism of ion screening from mostly ionic to purely resistive which are distinctly different from each other. Similar shifts from purely resistive to shielded and capacitive voltage profiles are obtained when the timescale of both experiments and simulations are decreased such that charge movement cannot be completed in the given timescale since it is inherently a slower process.

The switching between the resistive and shielded behavior and the critical frequency at which this transition occurs can be modeled with the coarse grained electrostatic model described here as shown in Figure 6.6 and 6.7 for different device geometries. Two different device geometries differing only in terms of their choice of electrode can be fabricated as illustrated in Figure 6.3. The ionic liquid can be placed in between two Au planar contacts or two Pt point contacts. As previously explained, due to the timescale of a line scan both the positive and the negative cycles of an 8 V_{pp} square wave is measured simultaneously. In Figure 6.6, the relatively unchanging region in the experimental data from 3 to 5 mm is due to the direct contact between the Au electrode and the ionic liquid. For this region the ionic liquid perfectly follows the Au signal and does not undergo screening. This shows that the contact resistances in this device geometry is negligible. For both geometries the overall nature of the observed binding energy shifts ranges from

resistive (at high frequencies) to shielded at lower frequencies as shown in Figure 6.6-a and Figure 6.7-a. The same behavior can be captured by the simulations as shown in Figure 6.6-b and Figure 6-7-b.

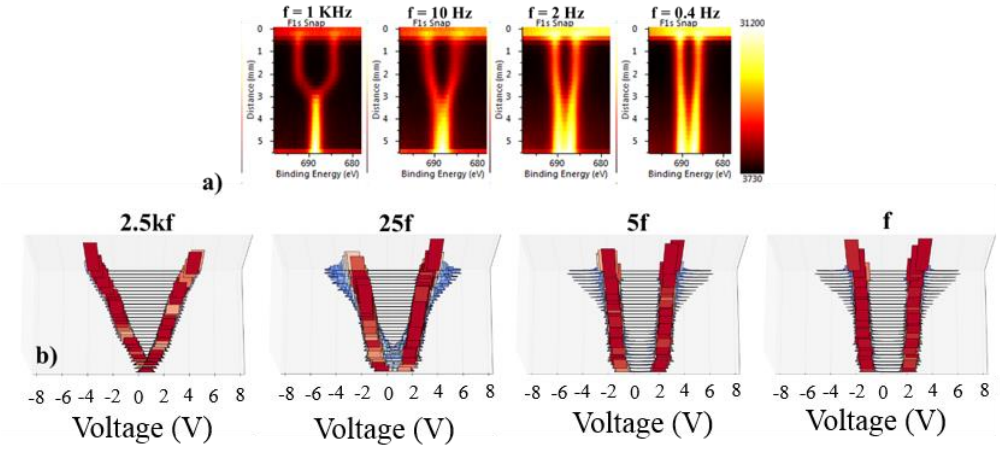

Figure 6. 6 The response of the ionic liquid to an 8 V_{p-p} square wave at varying frequencies a) measured by XPS for a device with two planar Au contacts, b) simulated by the coarse grained electrostatic model.

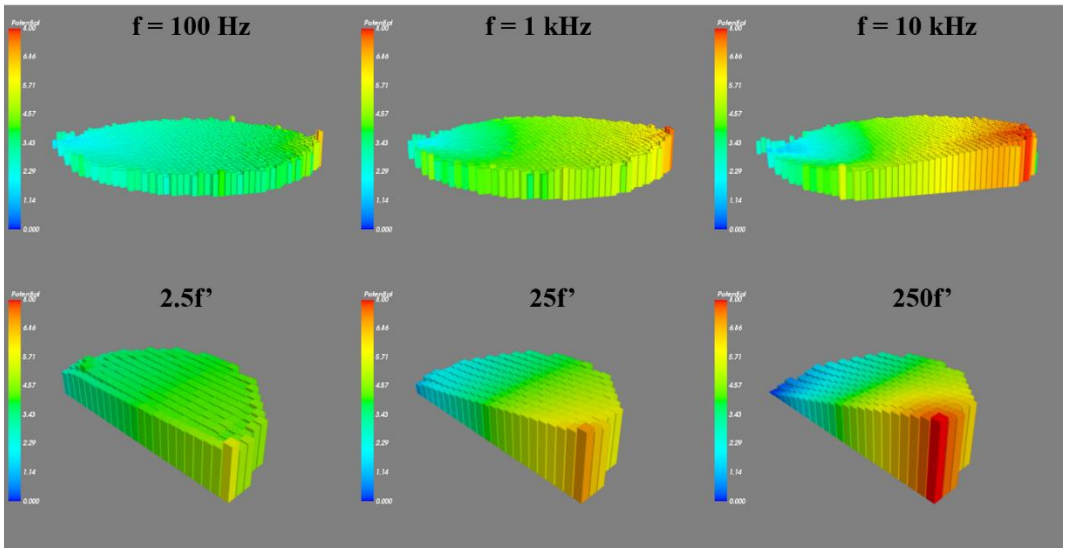

Figure 6. 7 The response of the ionic liquid to an 8 Vp-p square wave at varying frequencies a) measured by XPS for a device with two Pt point contacts, b) simulated by the coarse grained electrostatic model

Aside from being able to explain the ion screening effects at extended distances, another important insight gained by this model is the ability to track the number of

particles at various positions in the ionic liquid. Tracking number of particles corroborate the picture depicted in Figure 6.6 and Figure 6.7. At low frequencies where ions have enough time to properly screen the external bias, charged species are concentrated at the electrode surfaces while at higher frequencies charged species are equally distributed throughout the ionic liquid as shown in Figure 6.8.

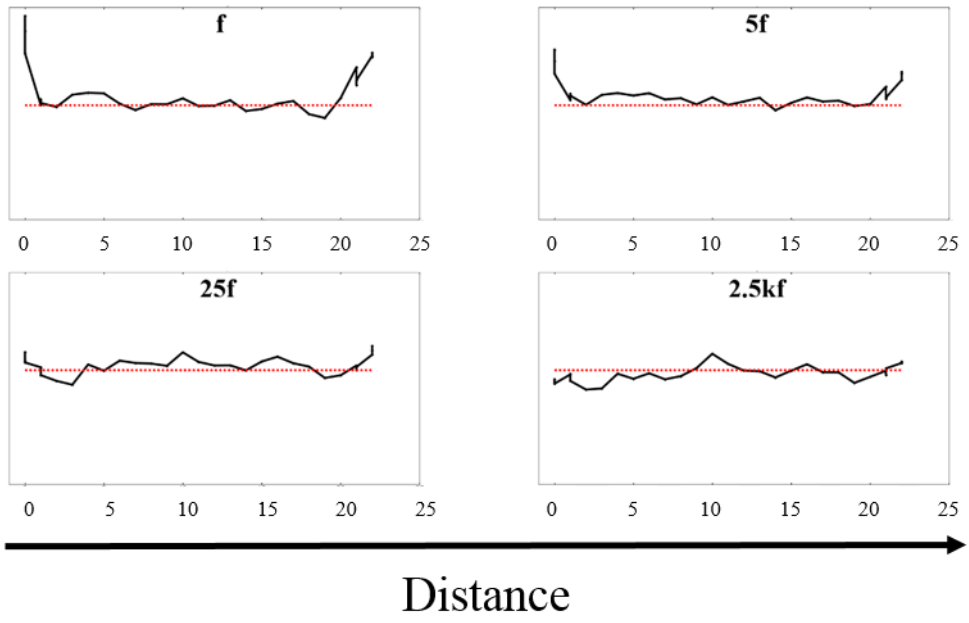

Figure 6. 8 Number of particles at various positions at the ionic liquid surface across different timescales (red line is the initial number of particles).

Considering the number of particles as a function of time at different frequencies of simulated square waves as shown in Figure 6.9, we can see that whenever the polarity is altered a quick drop in charged particles is seen. This is reflected in the voltage profile as a peak higher than the applied voltage for the side where the potential is applied (the source electrode) while it is reflected as a slow rise on the grounded side (the grounded electrode), consistent with an equivalent circuit of RC for each electrode. Almost 200 particles are in flux during this transient as shown

in Figure 6.9. As seen for the histograms and the surface maps shown in Figure 6.6 and Figure 6.7, at higher frequencies, these particles do not have enough time to appropriately screen the bias prior to its switch in polarity. The high number of particles in flux across long distances (~mm) suggests a mixed form of ion transport. Aside from migration; Pairs, starting from the grids near/at the electrodes, participate in the association equilibrium to quickly shuttle appropriate charges to the electrodes. For instance, consider a grid where an applied bias of 4V is already at the steady state (i.e. the majority of the boxes near the middle of the ionic liquid show 2V), this grid has an abundance of negative charges to screen the applied potential. Once the polarity is switched, however, these charges need to be either shuttled away or stored as pairs near the grid in question, where shuttling alone is modeled as a relatively slow process[6]. Further, the effect of association equilibrium at the same modeled time scale (Figure 6.5) also suggests a similar picture, where if the tendency to form pairs is high, once charges are paired, they can no longer split at the opposite electrode to shield the applied bias at the given timescale. Rather, screening is achieved by the migration of the sparse number of charged species which is inherently slower.

[6] given that the timescale of the simulations are normalized such that the highest possible field movement can only move a particle across one grid

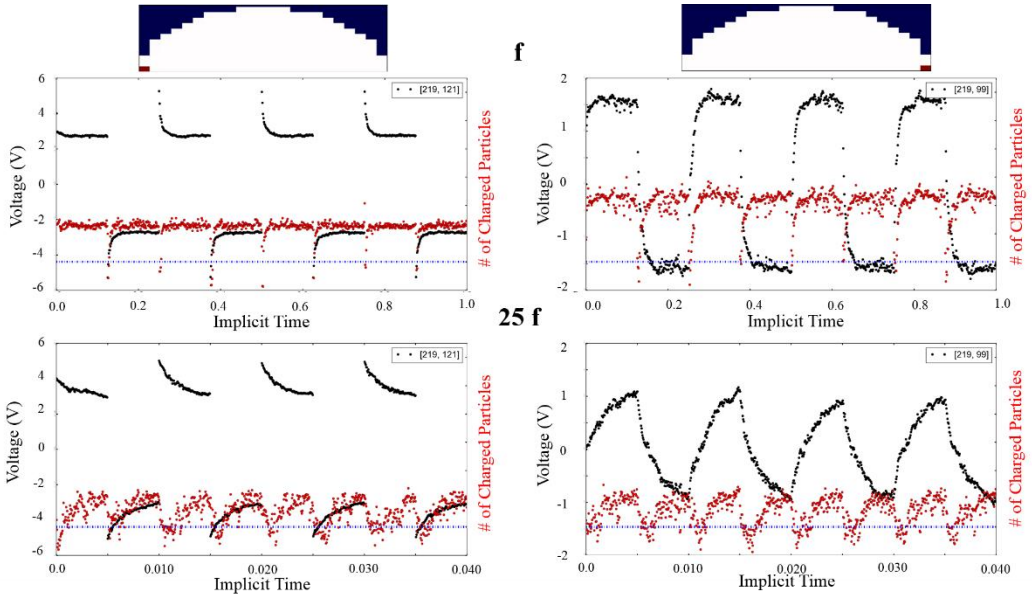

Figure 6. 9 The simulated voltage response of the ionic liquid at different frequencies of 8 $V_{p\text{-}p}$ square wave (black), the corresponding change in total number of particles at the given grid (red). The left panels show the response of a grid near the source electrode while right panels show the response near the grounded electrode.

6.4 Conclusions

The otherwise unexplained effects of double layer formation at extended distances (~mm) observed experimentally for ionic liquid drops under external bias using XPS [16] is modeled using a computationally inexpensive coarse grained electrostatic model. The model can match the frequency evolution of the ionic liquid response from resistive to screened while highlighting the importance of the pairing equilibrium in ion transport, especially at extended distances.

Chapter 7

7. Conclusion and Future Work

7.1 Conclusion and Future Work

Towards development of better electrochemical devices, studies outlined in this thesis involve both experimental and modelling efforts. On the experimental side both development of new electroanalytical tools that improve upon the state of the art and fundamental studies on electrochemically uncharted electrolytes or timescale regimes are presented. Although all described studies are firmly under the field of electrochemistry, know-how in terms of analog electronics, basic computer science and data science was integral in effectively reaching conclusions throughout our studies outlining the variety of the problems tackled in this thesis. Investigations and interrogations to further control over ion transport at various media and interfaces will be continued in the systems outlined both through fundamental electrochemical studies of various materials and development of novel electroanalytical tools. In terms of fundamental electrochemical studies

unconventional electrolytes (such as Liquid Crystals and Ionic Liquids) by presenting novel properties compared to their dilute electrolyte counterparts present interesting alternatives especially for various energy applications. Overall achieved goals and the future perspectives for each of the chapters discussed is the following;

- Liquid Crystal mesophases were shown as a possible electrolyte substitute similar to gel electrolytes. Investigations towards the different domains present and the distinct electrochemical behavior of these domains with regards to both ion activity and transport will be investigated using not only electrochemical tools but also with other more chemically resolved tools such as NMR will be pursued.
- A coarse grained electrostatic model to explain experimentally observed charge screening behavior of Ionic Liquids was developed. The developed electrostatic model will be screened to search for critical physical parameters that can improve device performance.
- A new Spectroelectrochemical method that can decouple the limiting effects of ion transport on electron transfer was outlined for electrochromic devices. The long investigated charge transport in conjugated polymers will be revisited with the developed Ultrafast Spectroelectrochemical method to

investigate the effects of film properties in detail without transport limits imposed by the counter ion.

- Electrochemical noise measurement and analysis, for the first time for high capacitance electrodes, was shown as a promising tool in diagnosis of battery health. Electrochemical noise as a quality control tool for commercial batteries will be further investigated with respect to battery cycling and other forms of battery abuse (aside from the short circuit scenario investigated). Moreover, development of time domain analysis tools such as auto correlation and recurrence quantification analysis to elucidate details in the stochastic data to both improve the predictive ability of the method and to identify processes responsible for the observed noise will be pursued.
- Hydrogen permeation and facile proton formation/diffusion at coating defects were leveraged to obtain local corrosion and defect information. A similar methodology under cathodic protection will be developed to ensure coating integrity throughout the experiment such that local information can be obtained non-destructively.

.

Bibliography

[1] P.F. Smith, K.J. Takeuchi, A.C. Marschilok, E.S. Takeuchi, Holy grails in chemistry: Investigating and understanding fast electron/cation coupled transport within inorganic ionic matrices, Acc. Chem. Res. 50 (2017) 544–548. doi:10.1021/acs.accounts.6b00540.

[2] M. V. Fedorov, A.A. Kornyshev, Ionic liquids at electrified interfaces, Chem. Rev. 114 (2014) 2978–3036. doi:10.1021/cr400374x.

[3] X. Ren, P.G. Pickup, Coupling of ion and electron transport during impedance measurements on a conducting polymer with similar ionic and electronic conductivities, J. Chem. Soc. Faraday Trans. 89 (1993) 321. doi:10.1039/ft9938900321.

[4] M. Doyle, T.F. Fuller, J. Newman, Modeling of Galvanostatic Charge and Discharge of the Lithium/Polymer/Insertion Cell, J. Electrochem. Soc. 140 (1993) 1526. doi:10.1149/1.2221597.

[5] A.N. Dey, B.P. Sullivan, The Electrochemical Decomposition of Propylene Carbonate on Graphite, J. Electrochem. Soc. 117 (1970) 222. doi:10.1149/1.2407470.

[6] D. Aurbach, B. Markovsky, M.. Levi, E. Levi, A. Schechter, M. Moshkovich, Y. Cohen, New insights into the interactions between electrode materials and electrolyte solutions for advanced nonaqueous batteries, J. Power Sources. 81-82 (1999) 95–111. doi:10.1016/S0378-7753(99)00187-1.

[7] E. Peled, Advanced Model for Solid Electrolyte Interphase Electrodes in Liquid and Polymer Electrolytes, J. Electrochem. Soc. 144 (1997) L208. doi:10.1149/1.1837858.

[8] A. Wang, S. Kadam, H. Li, S. Shi, Y. Qi, Review on modeling of the anode

solid electrolyte interphase (SEI) for lithium-ion batteries, Npj Comput. Mater. 4 (2018). doi:10.1038/s41524-018-0064-0.

[9] H. Liu, A. Banerjee, B. Ziv, K.J. Harris, N.P.W. Pieczonka, S. Luski, G.A. Botton, G.R. Goward, D. Aurbach, I.C. Halalay, Elucidating the Li-Ion Battery Performance Benefits Enabled by Multifunctional Separators, ACS Appl. Energy Mater. 1 (2018) acsaem.8b00436. doi:10.1021/acsaem.8b00436.

[10] A. Banerjee, B. Ziv, Y. Shilina, S. Luski, D. Aurbach, I.C. Halalay, Acid-Scavenging Separators: A Novel Route for Improving Li-Ion Batteries' Durability, ACS Energy Lett. 2 (2017) 2388–2393. doi:10.1021/acsenergylett.7b00763.

[11] D.R. MacFarlane, M. Forsyth, E.I. Izgorodina, A.P. Abbott, G. Annat, K. Fraser, On the concept of ionicity in ionic liquids, Phys. Chem. Chem. Phys. 11 (2009) 4962. doi:10.1039/b900201d.

[12] E.J.F. Dickinson, J.G. Limon-Petersen, R.G. Compton, The electroneutrality approximation in electrochemistry, J. Solid State Electrochem. 15 (2011) 1335–1345. doi:10.1007/s10008-011-1323-X.

[13] M.T. Camci, B. Ulgut, C. Kocabas, S. Suzer, In-situ XPS Reveals Voltage Driven Asymmetric Ion-Movement of an Ionic Liquid through the Pores of a Multi-Layer Graphene Electrode, J. Phys. Chem. C. (2018). doi:10.1021/acs.jpcc.8b02759.

[14] M.Z. Bazant, B.D. Storey, A.A. Kornyshev, Double layer in ionic liquids: Overscreening versus crowding, Phys. Rev. Lett. 106 (2011) 6–9. doi:10.1103/PhysRevLett.106.046102.

[15] A.A. Lee, S. Kondrat, D. Vella, A. Goriely, Dynamics of Ion Transport in Ionic Liquids, Phys. Rev. Lett. 115 (2015) 1–5. doi:10.1103/PhysRevLett.115.106101.

[16] M.T. Camci, P. Aydogan, B. Ulgut, C. Kocabas, S. Suzer, XPS enables visualization of electrode potential screening in an ionic liquid medium with temporal- and lateral-resolution, Phys. Chem. Chem. Phys. 18 (2016) 28434–28440. doi:10.1039/C6CP04933H.

[17] R.A. Noulty, D.G. Leaist, Activity coefficients and diffusion coefficients of dilute aqueous solutions of lithium, sodium, and potassium hydroxides, J. Solution Chem. 13 (1984) 767–778. doi:10.1007/BF00647692.

[18] V.A. Azov, K.S. Egorova, M.M. Seitkalieva, A.S. Kashin, V.P. Ananikov, “Solvent-in-salt” systems for design of new materials in chemistry, biology and energy research, Chem. Soc. Rev. 47 (2018) 1250–1284. doi:10.1039/C7CS00547D.

[19] L. Suo, F. Han, X. Fan, H. Liu, K. Xu, C. Wang, “Water-in-Salt” electrolytes enable green and safe Li-ion batteries for large scale electric energy storage applications, J. Mater. Chem. A. 4 (2016) 6639–6644. doi:10.1039/C6TA00451B.

[20] O. Celik, Ö. Dag, A new lyotropic liquid crystalline system:oligo(ethylene oxide) surfactants with [M(H2O)n]Xm Transition metal complexes, Angew. Chem. Int. Ed. (2001) 3800–3803.

[21] M.E.G. Lyons, Electroactive Polymer Electrochemistry, Springer US, Boston MA, 1994.

[22] A.J. Bard, L.R. Faulkner, Electrochemical Methods: Fundamentals and Applications, 2nd ed., John Wiley and Sons Inc, n.d.

[23] W.H. Reinmuth, Three-Dimensional Representation of Voltammetric Processes, Anal. Chem. 32 (1960) 1509–1512. doi:10.1021/ac60167a035.

[24] R.S. Nicholson, I. Shain, Theory of Stationary Electrode Polarography: Single Scan and Cyclic Methods Applied to Reversible, Irreversible, and Kinetic Systems, Anal. Chem. 36 (1964) 706–723. doi:10.1021/ac60210a007.

[25] S.R. Belding, J.G. Limon-Petersen, E.J.F. Dickinson, R.G. Compton, Cyclic voltammetry in the absence of excess supporting electrolyte offers extra kinetic and mechanistic insights: Comproportionation of anthraquinone and the anthraquinone dianion in acetonitrile, Angew. Chemie - Int. Ed. 49 (2010) 9242–9245. doi:10.1002/anie.201004874.

[26] R.A. Cottis, Interpretation of Electrochemical Noise Data, Corrosion. 57 (2001) 265–285.

[27] S. Ritter, F. Huet, R.A. Cottis, Guideline for an assessment of electrochemical noise measurement devices, Mater. Corros. 63 (2012) 297–302. doi:10.1002/maco.201005839.

[28] G. Blanc, C. Gabrielli, M. Keddam, Measurement of the electrochemical noise by a cross correlation method, Electrochim. Acta. 20 (1975) 687–689. doi:10.1016/0013-4686(75)90069-9.

[29] K. Hladky, J.L. Dawson, The measurement of localized corrosion using electrochemical noise, Corros. Sci. 21 (1981) 317–322. doi:10.1016/0010-938X(81)90006-8.

[30] W. Liu, D. Wang, X. Chen, C. Wang, H. Liu, Recurrence plot-based dynamic analysis on electrochemical noise of the evolutive corrosion process, Corros. Sci. 124 (2017) 93–102. doi:10.1016/j.corsci.2017.05.012.

[31] R. Maizia, A. Dib, A. Thomas, S. Martemianov, Proton exchange membrane fuel cell diagnosis by spectral characterization of the electrochemical noise, J. Power Sources. 342 (2017) 553–561. doi:10.1016/j.jpowsour.2016.12.053.

[32] A. Szewczyk, Lentka, J. Smulko, P. Babuchowska, F. Béguin, Measurements of flicker noise in supercapacitor cells, 2017 Int. Conf. Noise Fluctuations, ICNF 2017. (2017) 2–5. doi:10.1109/ICNF.2017.7985985.

[33] P.R. Roberge, R. Beaudoin, G. Verville, J. Smit, Voltage noise measurements on sealed leadacid batteries, J. Power Sources. 27 (1989) 177–186. doi:10.1016/0378-7753(89)80131-4.

[34] S. Martinet, R. Durand, P. Ozil, P. Leblanc, P. Blanchard, Application of electrochemical noise analysis to the study of batteries: state-of-charge determination and overcharge detection, J. Power Sources. 83 (1999) 93–99. doi:10.1016/S0378-7753(99)00272-4.

[35] B. Ulgut, Analysis of electrochemical noise in NiCd batteries throughout their lifetime, Turkish J. Chem. (2018) 1–10. doi:10.3906/kim-1710-84.

[36] S. Martemianov, N. Adiutantov, Y.K. Evdokimov, L. Madier, F. Maillard, A. Thomas, New methodology of electrochemical noise analysis and applications for commercial Li-ion batteries, J. Solid State Electrochem. 19 (2015) 2803–2810. doi:10.1007/s10008-015-2855-2.

[37] C.A. Little, R. Xie, C. Batchelor-McAUley, E. Katelhon, X. Li, N.P. Young, R.G. Compton, A Quantitative Methodology for the Study of Particle-Electrode Impacts, Phys. Chem. Chem. Phys. (2018) 13537–13546. doi:10.1039/C8CP01561A.

[38] A.R. Zeradjanin, E. Ventosa, A.S. Bondarenko, W. Schuhmann, Evaluation of the catalytic performance of gas-evolving electrodes using local electrochemical noise measurements, ChemSusChem. 5 (2012) 1905–1911. doi:10.1002/cssc.201200262.

[39] S.M. Lambert, M. Armstrong, P.S. Attidekou, P.A. Christensen, J.D. Widmer, C. Wang, K. Scott, Rapid nondestructive-testing technique for in-line quality control of li-ion batteries, IEEE Trans. Ind. Electron. 64 (2017) 4017–4026. doi:10.1109/TIE.2016.2643601.

[40] M. Petzl, M.A. Danzer, Nondestructive detection, characterization, and quantification of lithium plating in commercial lithium-ion batteries, J. Power Sources. 254 (2014) 80–87. doi:10.1016/j.jpowsour.2013.12.060.

[41] Technavio, Global Primary Battery Market 2018-2022, 2018. https://www.technavio.com/report/global-primary-battery-market-analysis-share-2018.

[42] E. Ozdemir, IMPEDANCE BASED MODELING OF BATTERY PARAMETERS AND BEHAVIOR, (2017).

[43] A. Aballe, M. Bethencourt, F.J. Botana, M. Marcos, Using wavelets transform in the analysis of electrochemical noise data, Electrochim. Acta. 44 (1999) 4805–4816. doi:10.1016/S0013-4686(99)00222-4.

[44] Y. Hoshi, N. Yakabe, K. Isobe, T. Saito, I. Shitanda, M. Itagaki, Wavelet transformation to determine impedance spectra of lithium-ion rechargeable battery, J. Power Sources. 315 (2016) 351–358. doi:10.1016/j.jpowsour.2016.03.048.

[45] Y. Hou, C. Aldrich, K. Lepkova, L.L. Machuca, B. Kinsella, Monitoring of carbon steel corrosion by use of electrochemical noise and recurrence quantification analysis, Corros. Sci. 112 (2016) 63–72. doi:10.1016/j.corsci.2016.07.009.

[46] P.R. Roberge, Analysis of electrochemical noise by the stochastic process detector method, Corrosion. 50 (1994) 502–512. doi:10.5006/1.3294350.

[47] J.D. Hunter, Matplotlib: A 2D graphics environment, Comput. Sci. Eng. 9 (2007) 99–104. doi:10.1109/MCSE.2007.55.

[48] S. Van Der Walt, S.C. Colbert, G. Varoquaux, The NumPy array: A structure for efficient numerical computation, Comput. Sci. Eng. 13 (2011) 22–30. doi:10.1109/MCSE.2011.37.

[49] J.A. Motchenbacher, C.D., Connelly, Low-Noise Electronic System Design, 1st ed., John Wiley & Sons, Inc., New York, NY, USA, 1993.

[50] S. Piller, M. Perrin, A. Jossen, Methods for state-of-charge determination and their applications, J. Power Sources. 96 (2001) 113–120.

doi:10.1016/S0378-7753(01)00560-2.

[51] C.B. Uzundal, B. Ulgut, Method for visualizing under-coating corrosion utilizing pH indicators before visible damage, Prog. Org. Coatings. 122 (2018) 72–78. doi:10.1016/j.porgcoat.2018.05.011.

[52] X.G. Zhang, Under-Paint Corrosion, in: Corros. Electrochem. Zinc, 1st ed., Springer Science, New York, 1996: pp. 315–336.

[53] P.L. Bonora, F. Deflorian, L. Fedrizzi, Electrochemical Impedance Spectroscopy as a Tool for Investigating Underpaint Corrosion, Electrochim. Acta. 41 (1996) 1073–1082.

[54] M.B. Jensen, A. Guerard, D.E. Tallman, G.P. Bierwagen, Studies of Electron Transfer at Aluminum Alloy Surfaces by Scanning Electrochemical Microscopy, J. Electrochem. Soc. 155 (2008) C324. doi:10.1149/1.2916734.

[55] G.P. Bierwagen, Reflections on corrosion control by organic coatings, Prog. Org. Coatings. 28 (1996) 43–48. doi:10.1016/0300-9440(95)00588-9.

[56] M. Yan, C.A. Vetter, V.J. Gelling, Corrosion inhibition performance of polypyrrole Al flake composite coatings for Al alloys, Corros. Sci. 70 (2013) 37–45. doi:10.1016/j.corsci.2012.12.019.

[57] H. Ochs, J. Vogelsang, G. Meyer, Enhanced surface roughness of organic coatings due to UV-degradation: An unknown source of EIS-artifacts, Prog. Org. Coatings. 46 (2003) 182–190. doi:10.1016/S0300-9440(03)00004-3.

[58] W. Shi, S.B. Lyon, Investigation using localised SVET into protection at defects in epoxy coated mild steel under intermittent cathodic protection simulating inter-tidal and splash zones, Prog. Org. Coatings. 102 (2017) 66–70. doi:10.1016/j.porgcoat.2016.04.035.

[59] R.F. Anastasi, E.I. Madaras, Terahertz NDE for under paint corrosion detection and evaluation, AIP Conf. Proc. 820 I (2006) 515–522. doi:10.1063/1.2184571.

[60] D. Hughes, Microwave Nondestructive Detection of Corrosion Under Thin Paint and Primer in Aluminum Panels, AIP Conf. Proc. 557 (2001) 460–466. doi:10.1063/1.1373793.

[61] M.A. V. Devanathan, Z. Stachurski, The mechanism of hydrogen evolution on iron in acid solutions by determination of permeation rates, J.

Electrochem. Soc. 111 (1964) 619–623. doi:10.1149/1.2426195.

[62] M.A. V Devanathan, Z. Stachurski, The Adsorption and Diffusion of Electrolytic Hydrogen in Palladium, Proc. R. Soc. A Math. Phys. Eng. Sci. 270 (1962) 90–102. doi:10.1098/rspa.1962.0205.

[63] American Society for Testing Materials, Standard Practice for Evaluation of Hydrogen Uptake , Permeation , and Transport in Metals by an Electrochemical Technique, G148-97. i (2011) 1–10. doi:10.1520/G0148-97R11.

[64] D. Vijayshankar, A. Altin, C. Merola, A. Bashir, E. Heinen, M. Rohwerder, Probing the Buried Metal-Organic Coating Interfacial Reaction Kinetic Mechanisms by a Hydrogen Permeation Based Potentiometric Approach, J. Electrochem. Soc. 163 (2016) C778–C783. doi:10.1149/2.0971613jes.

[65] D. Vijayshankar, T.H. Tran, A. Bashir, S. Evers, M. Rohwerder, Hydrogen Permeation as a Tool for Quantitative Characterization of Oxygen Reduction Kinetics at Buried Metal-Coating Interfaces, Electrochim. Acta. 189 (2016) 111–117. doi:10.1016/j.electacta.2015.12.030.

[66] S. Evers, M. Rohwerder, The hydrogen electrode in the dry: A Kelvin probe approach to measuring hydrogen in metals, Electrochem. Commun. 24 (2012) 85–88. doi:10.1016/j.elecom.2012.08.019.

[67] J. Jin, M. Prochaska, D. Rochefort, D.K. Kim, L. Zhuang, F.J. DiSalvo, R.B. van Dover, H.D. Abruña, A high-throughput search for direct methanol fuel cell anode electrocatalysts of type PtxBiyPbz, Appl. Surf. Sci. 254 (2007) 653–661. doi:10.1016/j.apsusc.2007.06.077.

[68] E. Reddington, A. Sapienza, B. Gurau, R. Viswanathan, S. Sarangapani, Combinatorial Electrochemistry : A Highly Parallel , Optical Screening Method for Discovery of Better Electrocatalysts Combinatorial Electrochemistry : A Highly Parallel , Optical Screening Method for Discovery of Better Electrocatalysts, 280 (1998) 2–5. doi:10.1126/science.280.5370.1735.

[69] V. Boudon, G. Pierre, H. Bürger, High-Resolution Spectroscopy and Analysis of the ν4 Bending Region of SF6 near 615 cm−1, J. Mol. Spectrosc. 205 (2001) 304–311. doi:10.1006/jmsp.2000.8267.

[70] B. Verity, S.W. Bigger, The dependence of quinine fluorescence quenching on ionic strength, Int. J. Chem. Kinet. 28 (1996) 919–923.

[71] C.B. Uzundal, F. Mert Balci, B. Ulgut, Ö. Dag, Lyotropic Liquid Crystalline Mesophase of Sulfuric Acid–Nonionic Surfactant Stabilizes Lead(II) Oxide in Sulfuric Acid Concentrations Relevant to Lead Acid Batteries, ACS Omega. 2 (2017) 3785–3791. doi:10.1021/acsomega.7b00833.

[72] R.A. Robinson, R.H. Stokes, Electrolyte Solutions, Dover Publications, 1955.

[73] C. Albayrak, A. Cihaner, Ömer Dag, A new, highly conductive, lithium salt/nonionic surfactant, lyotropic liquid-crystalline mesophase and its application, Chem. A Eur. J. 18 (2012) 4190–4194. doi:10.1002/chem.201103705.

[74] E. Tunkara, C. Albayrak, E.O. Polat, C. Kocabas, Ö. Dag, Highly proton conductive phosphoric acid-nonionic surfactant lyotropic liquid crystalline mesophases and application in graphene optical modulators, ACS Nano. 8 (2014) 11007–11012. doi:10.1021/nn505199q.

[75] E.B. Olutaş, F.M. Balcl, Ö. Dag, Strong Acid-Nonionic Surfactant Lyotropic Liquid-Crystalline Mesophases as Media for the Synthesis of Carbon Quantum Dots and Highly Proton Conducting Mesostructured Silica Thin Films and Monoliths, Langmuir. 31 (2015) 10265–10271. doi:10.1021/acs.langmuir.5b02225.

[76] T. Ichikawa, M. Yoshio, A. Hamasaki, J. Kagimoto, H. Ohno, T. Kato, 3D interconnected ionic nano-channels formed in polymer films: Self-organization and polymerization of thermotropic bicontinuous cubic liquid crystals, J. Am. Chem. Soc. 133 (2011) 2163–2169. doi:10.1021/ja106707z.

[77] M. Armand, F. Endres, D.R. MacFarlane, H. Ohno, B. Scrosati, Ionic-liquid materials for the electrochemical challenges of the future, Nat. Mater. 8 (2009) 621–629. doi:10.1038/nmat2448.

[78] S. Yazaki, M. Funahashi, J. Kagimoto, H. Ohno, T. Kato, Nanostructured liquid crystals combining ionic and electronic functions, J. Am. Chem. Soc. 132 (2010) 7702–7708. doi:10.1021/ja101366x.

[79] J. Sakuda, E. Hosono, M. Yoshio, T. Ichikawa, T. Matsumoto, H. Ohno, H. Zhou, T. Kato, Liquid-crystalline electrolytes for lithium-ion batteries: Ordered assemblies of a mesogen-containing carbonate and a lithium salt, Adv. Funct. Mater. 25 (2015) 1206–1212. doi:10.1002/adfm.201402509.

[80] T. Kobayashi, T. Ichikawa, T. Kato, H. Ohno, Development of Glassy Bicontinuous Cubic Liquid Crystals for Solid Proton-Conductive Materials, Adv. Mater. 29 (2017). doi:10.1002/adma.201604429.

[81] E. Yılmaz, E.B. Olutaş, G. Barım, J. Bandara, Ö. Dag, Lithium salt–nonionic surfactant lyotropic liquid crystalline gel-electrolytes with redox couple for dye sensitized solar cells, RSC Adv. 6 (2016) 97430–97437. doi:10.1039/C6RA19979H.

[82] D. Högberg, B. Soberats, S. Uchida, M. Yoshio, L. Kloo, H. Segawa, T. Kato, Nanostructured two-component liquid-crystalline electrolytes for higherature dye-sensitized solar cells, Chem. Mater. 26 (2014) 6496–6502. doi:10.1021/cm503090z.

[83] J. Garche, E. Karden, P.T. Moseley, D.A.J. Rand, Lead Acid Batteries for Future Automobiles, 1st ed., Elsevier Science, Amsterdam, 2017.

[84] D.P.A.T. III, Submarine Valve Regulated Lead Acid Batteries, (n.d.). http://www.dpatitle3.com/dpa_db/project.php?id=198 (accessed August 5, 2017).

[85] W.G. Davenport, M. King, Sulfuric Acid Manufacture, 1st ed., Elsevier Science, Amsterdam, 2005.

[86] D. Pavlov, Lead-Acid Batteries: Science and Technology: A Handbook of Lead-Acid Battery Technology and Its Influence on the Product, 1st ed., Elsevier Science, Amsterdam, 2011.

[87] B. Culpin, D. a. J. Rand, Failure modes of lead/acid batteries, J. Power Sources. 36 (1991) 415–438. doi:10.1016/0378-7753(91)80069-A.

[88] K. Sawai, T. Funato, M. Watanabe, H. Wada, K. Nakamura, M. Shiomi, S. Osumi, Development of additives in negative active-material to suppress sulfation during high-rate partial-state-of-charge operation of lead-acid batteries, J. Power Sources. 158 (2006) 1084–1090. doi:10.1016/j.jpowsour.2006.01.096.

[89] A.W. Stienecker, T. Stuart, C. Ashtiani, An ultracapacitor circuit for reducing sulfation in lead acid batteries for Mild Hybrid Electric Vehicles, J. Power Sources. 156 (2006) 755–762. doi:10.1016/j.jpowsour.2005.06.014.

[90] P. Delahay, M. Pourbaix, P. Van Rysselberghe, Potential-pH Diagram of Lead and its Applications to the Study of Lead Corrosion, J. Electrochem.

Soc. 98 (1951) 101. doi:10.1149/1.2778110.

[91] B.P. Varma, Lead acid battery with gel electrolyte, 6,143,967, 1982. https://www.google.com/patents/US4317872.

[92] D.W.H. Lambert, P.H.J. Greenwood, M.C. Reed, Advances in gelled-electrolyte technology for valve-regulated lead-acid batteries, J. Power Sources. 107 (2002) 173–179. doi:10.1016/S0378-7753(01)01072-2.

[93] M. Velický, K.Y. Tam, R.A.W. Dryfe, On the stability of the silver/silver sulfate reference electrode, Anal. Methods. 4 (2012) 1207. doi:10.1039/c2ay00011c.

[94] Z. Dongping, J. Velmurugan, M. V. Mirkin, Adsorption/desorption of hydrogen on Pt nanoelectrodes: Evidence of surface diffusion and spillover, J. Am. Chem. Soc. 131 (2009) 14756–14760. doi:10.1021/ja902876v.

[95] G.S. Attard, Mesoporous Platinum Films from Lyotropic Liquid Crystalline Phases, Science (80-.). 278 (1997) 838–840. doi:10.1126/science.278.5339.838.

[96] Z. Panossian, N.L. de Almeida, R.M.F. de Sousa, G. de S. Pimenta, L.B.S. Marques, Corrosion of carbon steel pipes and tanks by concentrated sulfuric acid: A review, Corros. Sci. 58 (2012) 1–11. doi:10.1016/j.corsci.2012.01.025.

[97] E. Rocca, J. Steinmetz, Mechanism of passivation of Pb(Ca)-Sn alloys in sulfuric acid: role of tin, Electrochim. Acta. 44 (1999) 4611–4618. doi:10.1016/S0013-4686(99)00186-3.

[98] T. Hirasawa, K. Sasaki, M. Taguchi, H. Kaneko, Electrochemical characteristics of Pb-Sb alloys in sulphuric acid solutions, J. Power Sources. 85 (2000) 44–48.

[99] A. Czerwiński, M. Żelazowska, M. Grdeń, K. Kuc, J.D. Milewski, A. Nowacki, G. Wójcik, M. Kopczyk, Electrochemical behavior of lead in sulfuric acid solutions, J. Power Sources. 85 (2000) 49–55. doi:10.1016/S0378-7753(99)00381-X.

[100] B.R. Eggins, J.Q. Chambers, Proton Effects in the Electrochemistry of the Quinone Hydroquinone System in Aprotic Solvents, J. Electrochem. Soc. 117 (1970) 186. doi:10.1149/1.2407462.

[101] N. Gupta, H. Linschitz, Hydrogen-bonding and protonation effects in electrochemistry of quinones in aprotic solvents, J. Am. Chem. Soc. 119

(1997) 6384–6391. doi:10.1021/ja970028j.

[102] Y. Hui, E.L.K. Chng, C.Y.L. Chng, H.L. Poh, R.D. Webster*, Hydrogen-Bonding Interactions between Water and the One and Two-Electron-Reduced Forms of Vitamin K1, J Am Chem Soc. 131 (2009) 1523–1534.

[103] R.S. Kim, W. Park, H. Hong, T.D. Chung, S. Kim, Quinone electrochemistry altered by local hydrophobic environment and hydrogen bonding interactions, Electrochem. Commun. 41 (2014) 39–43. doi:10.1016/j.elecom.2014.01.005.

[104] M. Quan, D. Sanchez, M.F. Wasylkiw, D.K. Smith, Voltammetry of quinones in unbuffered aqueous solution: Reassessing the roles of proton transfer and hydrogen bonding in the aqueous electrochemistry of quinones, J. Am. Chem. Soc. 129 (2007) 12847–12856. doi:10.1021/ja0743083.

[105] C. Amatore, C. Lefrou, F. Pflüger, On-line compensation of ohmic drop in submicrosecond time resolved cyclic voltammetry at ultramicroelectrodes, J. Electroanal. Chem. 270 (1989) 43–59. doi:10.1016/0022-0728(89)85027-2.

[106] C. Amatore, Y. Bouret, E. Maisonhaute, J.I. Goldsmith, H.D. Abruña, Ultrafast voltammetry of adsorbed redox active dendrimers with nanometric resolution: An electrochemical microtome, ChemPhysChem. 2 (2001) 130–134.

[107] P. Fortgang, E. Maisonhaute, C. Amatore, B. Delavaux-Nicot, J. Iehl, J.F. Nierengarten, Molecular motion inside an adsorbed [5:1] fullerene hexaadduct observed by ultrafast cyclic voltammetry, Angew. Chemie - Int. Ed. 50 (2011) 2364–2367. doi:10.1002/anie.201007289.

[108] X.S. Zhou, B.W. Mao, C. Amatore, R.G. Compton, J.L. Marignier, M. Mostafavi, J.F. Nierengarten, E. Maisonhaute, Transient electrochemistry: Beyond simply temporal resolution, Chem. Commun. 52 (2015) 251–263. doi:10.1039/c5cc07953e.

[109] C. Amatore, E. Maisonhaute, When voltammetry reaches nanoseconds., Anal. Chem. 77 (2005) 303A–311A. doi:10.1021/ac053430m.

[110] C. Amatore, Y. Bouret, E. Maisonhaute, H.D. Abruña, J.I. Goldsmith, Electrochemistry within molecules using ultrafast cyclic voltammetry, Comptes Rendus Chim. 6 (2003) 99–115. doi:10.1016/S1631-0748(03)00019-5.

[111] C. Amatore, E. Maisonhaute, G. Simonneau, Ultrafast cyclic voltammetry: Performing in the few megavolts per second range without ohmic drop, Electrochem. Commun. 2 (2000) 81–84. doi:10.1016/S1388-2481(99)00150-2.

[112] D.O. Wipf, E.W. Kristensen, M.R. Deakin, R.M. Wightman, Fast-scan cyclic voltammetry as a method to measure rapid heterogeneous electron-transfer kinetics, Anal. Chem. 60 (1988) 306–310. doi:10.1021/ac00155a006.

[113] R.B. Keithley, P. Takmakov, E.S. Bucher, A.M. Belle, C. a. Owesson-White, J. Park, R.M. Wightman, Higher sensitivity dopamine measurements with faster-scan cyclic voltammetry, Anal. Chem. 83 (2011) 3563–3571. doi:10.1021/ac200143v.

[114] M.L. a V Heien, M. a Johnson, R.M. Wightman, Resolving neurotransmitters detected by fast-scan cyclic voltammetry., Anal. Chem. 76 (2004) 5697–704. doi:10.1021/ac0491509.

[115] D. Britz, iR elimination in electrochemical cells, J. Electroanal. Chem. 88 (1978) 309–352. doi:10.1016/S0022-0728(78)80122-3.

[116] H.W. VandenBorn, D.H. Evans, Determination of Electrochemical Kinetic Parameters in High Resistance Solutions Using Semiintegration, Anal. Chem. 46 (1974) 643–646. doi:10.1021/ac60342a005.

[117] L.F.G. Williams, R.J. Taylor, iR correction. Part I. A computerised interrupt method, J. Electroanal. Chem. 108 (1980) 293–303. doi:10.1016/S0022-0728(80)80338-X.

[118] GamryInstruments, A Basic Understanding of iR Compensation, (n.d.). https://www.gamry.com/application-notes/instrumentation/understanding-ir-compensation (accessed July 17, 2018).

[119] R.S. Robinson, R.L. McCreery, Absorption Spectroelectrochemistry with Microelectrodes, Anal. Chem. 53 (1981) 997–1001. doi:10.1021/ac00230a017.

[120] M. Watanabe, M.L. Thomas, S. Zhang, K. Ueno, T. Yasuda, K. Dokko, Application of Ionic Liquids to Energy Storage and Conversion Materials and Devices, Chem. Rev. 117 (2017) 7190–7239. doi:10.1021/acs.chemrev.6b00504.

[121] A. Lewandowski, A. Świderska-Mocek, Ionic liquids as electrolytes for Li-

ion batteries-An overview of electrochemical studies, J. Power Sources. 194 (2009) 601–609. doi:10.1016/j.jpowsour.2009.06.089.

[122] A. Balducci, S.S. Jeong, G.T. Kim, S. Passerini, M. Winter, M. Schmuck, G.B. Appetecchi, R. Marcilla, D. Mecerreyes, V. Barsukov, V. Khomenko, I. Cantero, I. De Meatza, M. Holzapfel, N. Tran, Development of safe, green and high performance ionic liquids-based batteries (ILLIBATT project), J. Power Sources. 196 (2011) 9719–9730. doi:10.1016/j.jpowsour.2011.07.058.

[123] C. Kocabas, S. Suzer, Probing voltage drop variations in graphene with photoelectron spectroscopy, Anal. Chem. 85 (2013) 4172–4177. doi:10.1021/ac400489e.

[124] M.T. Camci, B. Ulgut, C. Kocabas, S. Suzer, In-Situ XPS Monitoring and Characterization of Electrochemically Prepared Au Nanoparticles in an Ionic Liquid, ACS Omega. 2 (2017) 478–486. doi:10.1021/acsomega.6b00456.

[125] E.F. Smith, I.J. Villar Garcia, D. Briggs, P. Licence, Ionic liquids in vacuo; solution-phase X-ray photoelectron spectroscopy, Chem. Commun. (2005) 5633–5635. doi:10.1039/b512311a.

[126] T.O. Tasci, E. Atalar, U.K. Demirok, S. Suzer, Electrical circuit modeling of surface structures for X-ray photoelectron spectroscopic measurements, Surf. Sci. 602 (2008) 365–368. doi:10.1016/j.susc.2007.10.041.

[127] S. Suzer, H. Sezen, G. Ertas, A. Dâna, XPS measurements for probing dynamics of charging, J. Electron Spectros. Relat. Phenomena. 176 (2010) 52–57. doi:10.1016/j.elspec.2009.02.003.

[128] M.J. Danielson, Use of the Devanathan-Stachurski cell to measure hydrogen permeation in aluminum alloys, Corros. Sci. 44 (2002) 829–840. doi:10.1016/S0010-938X(01)00103-2.